SOLID-STATE NUCLEAR MAGNETIC RESONANCE SPECTROSCOPY OF PHOSPHAZENE POLYMERS

ALEXEY S. BORISOV
B. Sc., St. Petersburg State Institute of Technology, 2001

A Thesis
Submitted to the School of Graduate Studies
of the University of Lethbridge
in Partial Fulfilment of the
Requirements for the Degree

MASTER OF SCIENCE

Department of Chemistry and Biochemistry
University of Lethbridge
LETHBRIDGE, ALBERTA, CANADA

To my family

ABSTRACT

High-resolution one-dimensional ^{1}H, ^{19}F, ^{31}P and ^{13}C MAS NMR experiments were used in a morphological study of solvent-cast and heat-treated poly[*bis*(trifluoroethoxy)phosphazene] (PBFP). Deconvolution analyses performed on all Nuclear Magnetic Resonance (NMR) spectra are presented. These results suggest the presence of broad and narrow overlapping components at ambient temperature, which were assigned to the crystalline, amorphous and the mesophase regions within the polymer, respectively. The number of signals in the spectra was independently verified using ^{1}H, ^{19}F and ^{13}C Discrimination Induced by Variable Amplitude Minipulses (DIVAM) nutation experiments. Deconvolution analyses showed that heat-treatment increases the overall crystallinity of the solvent-cast PBFP. Further studies conducted on two preparations of the polymer showed significant differences in crystallinity due to variations in the reaction conditions. Magic-Angle Spinning (MAS) NMR spectra of PBFP obtained via living cationic polymerization at ambient temperature indicated that the polymer contains mostly amorphous and mesophase regions with only a small contribution from the crystalline domain.

Variable-temperature ^{31}P NMR experiments suggested that the thermotropic transition occurs in a temperature range of 80ºC to 90ºC, where the crystalline signal disappears and a new signal due to a liquid crystalline phase emerges. Spin-lock ^{31}P experiments provided rates of the transverse relaxation in the rotating frame for each signal, showing that the crystalline and the amorphous regions within the polymer are characterized by significantly different mobilities at ambient temperatures, while the

comparable degree of motion occurs between the amorphous and mesophase environments at temperatures above 90ºC.

The process of thermal ring-opening polymerization of hexachlorocyclotriphosphazene was monitored using one-dimensional ^{31}P MAS NMR at different stages of the reaction. The ratio between cyclic species and the high molecular weight poly(dichlorophosphazene) was seen to change over time. ^{31}P NMR was seen to be a potentially valuable tool in monitoring rates of chain propagation, branching and cross-linking. Two-dimensional ^{31}P homonuclear Radio-Frequency Driven Recoupling (RFDR) and Incredible Natural Abundance Double Quantum Transfer (INADEQUATE) MAS NMR experiments were first tested on the partially phenoxy-substituted hexachlorocyclotriphosphazene, and subsequently applied in the study of a preparation of the partially trifluoroethoxy-substituted poly(dichlorophosphazene). Very high resolution was obtained in the direct dimension due to the presence of low molecular weight species. Preliminary spectral assignments of all of the observed signals were made on the basis of both known chemical shifts of the related species, and the through-space and through-bond phosphorous-phosphorous connectivities.

ACKNOWLEDGEMENTS

I would like to express my deepest gratitude to my supervisor Dr. P. Hazendonk, for his guidance and support over the duration of my studies. I also want to recognize Dr. P. G. Hayes for his continued encouragement and help. For helpful instruction and guidance in the solid-state NMR laboratory I am thankful to Dr. D. Iuga, Dr. P. Wormald and T. Montina. I also would like to acknowledge Dr. C. deDenus (Hobart and William Smith Colleges) and Dr. A. R. McWilliams (Ryerson). I want to express my appreciation to the University of Lethbridge for the given opportunity and financial support.

Last but not least, I would like to thank my family and all my friends for their support and patience.

TABLE OF CONTENTS

LIST OF TABLES

LIST OF FIGURES

1 INTRODUCTION

1.1 Nuclear Magnetic Resonance

1.1.1 Overview

Nuclear Magnetic Resonance (NMR) is a spectroscopic technique that observes intrinsic magnetic moment of the atomic nucleus in the presence of an external magnetic field. Since its discovery and characterization for use on liquids and solids independently by Felix Bloch and Edward Mills Purcell in 1946, NMR techniques have been rapidly developing in both instrumental and experimental aspects.[1] Today, this spectroscopic method is used routinely to provide unique information about structural chemical and physical properties, and dynamics of materials in both liquid and solid states.[1] Recent experimental advances make NMR an extremely powerful and versatile spectroscopic technique.

NMR manipulates the interactions between magnetic nuclei and magnetic fields. These interactions are strongly influenced by the local electronic environment of the observed nucleus in the material, and thus provide unique insight into chemical structure and dynamics.[2] To begin, it is best to describe the basic interactions between a nucleus and the externally applied magnetic field. From there, a description of the basic NMR experiment will follow, which leads into a brief introduction of interactions between nuclei and their surroundings. Within the context provided, advanced NMR experiments will be explained.

1.1.2 Spin and magnetism

Nucleons that compose the atomic nucleus possess the intrinsic quantum mechanical property of *spin*. The overall spin quantum number *S* of the magnetic particle is determined by the number of neutrons and protons in the nucleus and is given by either a whole number (0, 1, 2...) or a half-integer number (1/2, 3/2, 5/2…). Nuclear spin is an intrinsic quantum mechanical *spin angular momentum*, which is quantized, where the number of sub-levels is determined by *2S + 1*. In the absence of external fields, these states are degenerate and the directions of axis of the angular momentum are defined by isotropic distribution, as seen in figure 1.

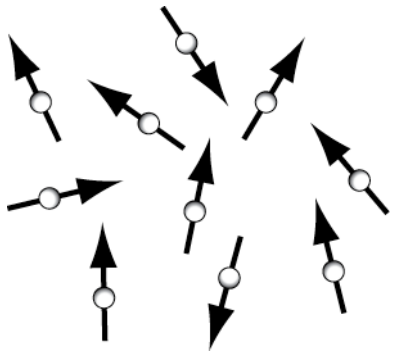

Figure 1 Isotropic distribution of spin magnetic moments in the absence of external magnetic field.[2]

In the presence of magnetic field these states are no longer degenerate. When placed in an external magnetic field, the axis of angular momentum is aligned with the magnetic field, which is arbitrarily chosen to be along the z-axis. In the case of spin-1/2, according to *2I + 1*, two states are possible, +1/2 and -1/2, pointing ‘up’ or ‘down’ with

respect to an external field, where orientations parallel to the field have reduced magnetic energy, and therefore are slightly more probable.

The magnetic moment μ experiences a torque perpendicular to its direction causing it to precess along the magnetic field direction. The frequency of this motion is specific to each type of nucleus and is referred to as a nuclear Larmor frequency ω_0. It is determined by the nuclear gyromagnetic ratio, γ, and the magnetic field strength, B_0, as follows:

$$\omega_0 = \gamma \times B_0 \tag{1}$$

The angle between spin polarization and an external magnetic field is defined by the initial orientation of a spin and is constant with respect to time, which is shown in figure 2 below.

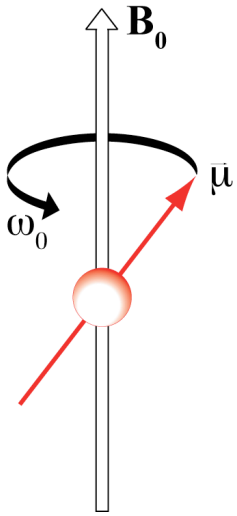

Figure 2 Precession of the spin magnetic moment in the presence of the external magnetic field B_0.[2]

On the macroscopic level, the sample in the presence of a magnetic field consists of an ensemble of randomly oriented spin magnetic moments, each precessing around the direction of the magnetic field at its Larmor frequency, out of phase with respect to each other. According to the Boltzmann distribution, the slight difference between energy level populations results in the higher probability of magnetic moments aligned parallel to the field. This gives rise to a longitudinal *net* magnetization, which is cylindrically symmetrical along the magnetic field and therefore has no transverse component (shown in figure 3).

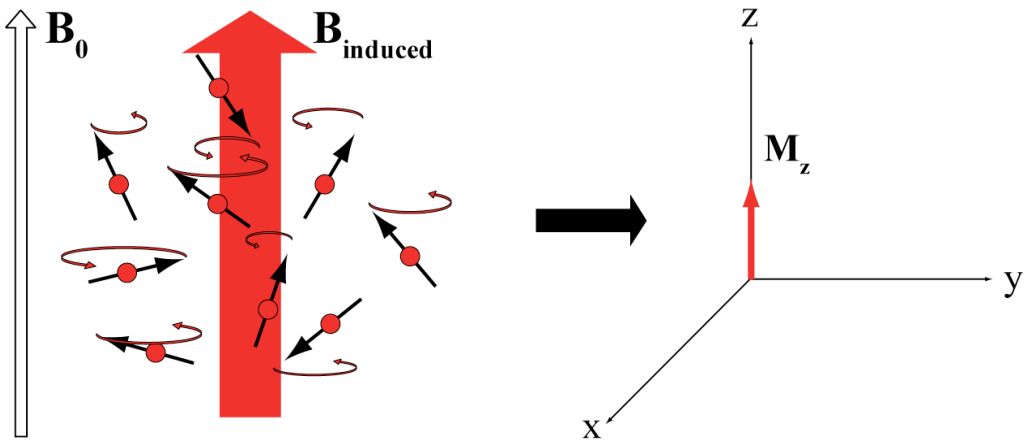

Figure 3 Ensemble of spins precessing at ω_0 in the presence of the external magnetic field B_0 along *z*-axis (left), and the corresponding longitudinal magnetization vector (right).[2]

1.1.3 NMR magnet

A static magnetic field used in NMR has to be as large and as homogeneous as possible. The homogeneity of at least one part per 10^9 has to be maintained throughout the entire volume of a sample. The field also has to be stable over time, with drifts not exceeding several hertz per hour. Most NMR spectrometers today achieve this using solenoid magnets made from a superconducting Sn/Nb alloy. This material is superconductive at 4K, and therefore needs to be submersed in a liquid He bath, which is in turn surrounded by a reservoir filled with liquid N_2. Control over the field homogeneity is achieved with additional sets of coils located inside the liquid He bath and around the bore of the magnet, which are referred to as superconducting shims and room-temperature shims, respectively.

The strength of the magnetic field at which NMR magnets operate is conventionally referred to as the corresponding Larmor frequency of proton, i.e. an instrument producing a 11.4 Tesla magnetic field would be referred to as a 500 MHz magnet. The most commonly used NMR spectrometers today operate at frequencies from 300 to 950 MHz.

1.1.4 Longitudinal and transverse relaxation

The induced longitudinal polarization is too weak to be readily detected; instead, it is best to detect it when perpendicular to the external field. If it were possible for the spins to precess in phase with each other, it would give rise to a bulk transverse magnetization rotating at a Larmor frequency. This phase coherence can be achieved by applying a strong radiofrequency pulse on resonance with the Larmor frequency. The net effect of this pulse is to rotate the bulk longitudinal polarization into the transverse plane. This is shown schematically in figure 4.

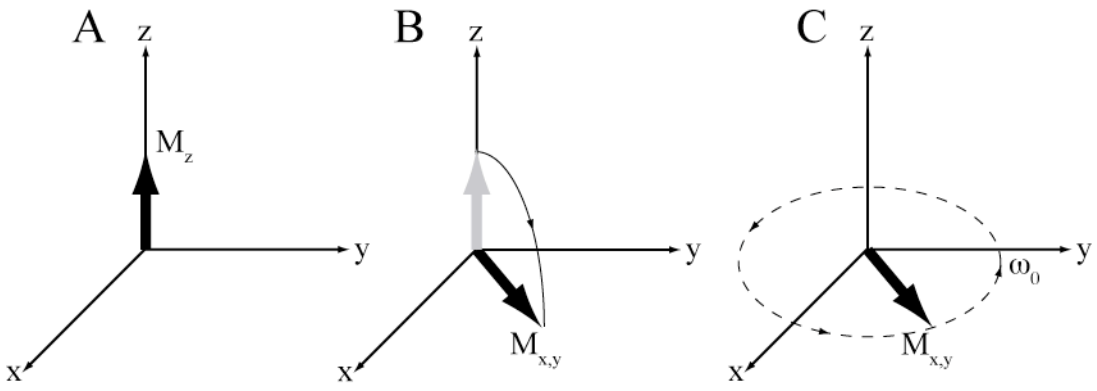

Figure 4 (A) The z-component of the net magnetization; (B) The magnetization rotated to the transverse plane by application of the $\pi/2$ RF pulse; (C) Larmor precession of the transverse polarization.

Spins experience constant perturbations from small locally random time-dependent magnetic fields due to neighboring spins and other electronic interactions. Through this diffusion-like process the spins always randomly re-orient and hence have an isotropic distribution of orientations in the absence of an external magnetic field. When a strong external magnetic field is applied along the *z*-axis, it causes spins to

randomly ‘walk’ towards this direction, giving rise to a net bias in the orientations over time. The rate of reorientation of the spins, and the corresponding build-up of macroscopic longitudinal magnetization is characterized by a longitudinal relaxation time constant, T_1. T_1 largely depends on the time scale of the local fluctuating fields and hence is dependent on the temperature and viscosity of the material. It can be in the range from ms to days or weeks. When an external field is turned off, the net polarization is lost over time due to the same perturbations. Time-dependence of the longitudinal magnetization can be characterized by the curve shown in figure 5.

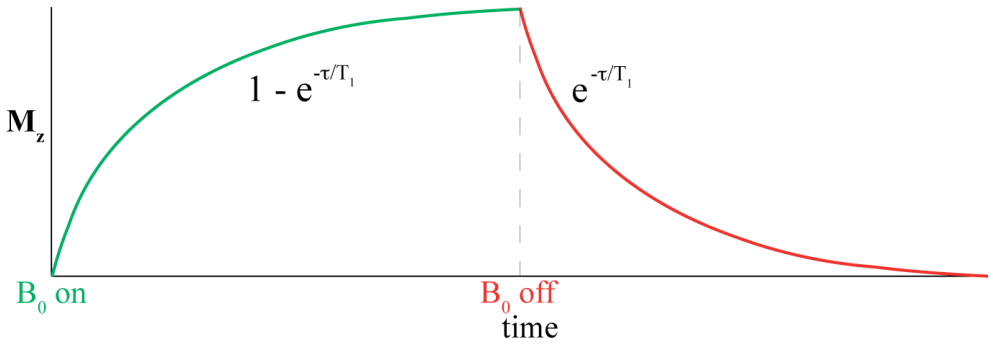

Figure 5 Build-up and decay of the longitudinal magnetization at a rate defined by T_1.

Recall that a radiofrequency pulse creates phase coherence between spins. Fluctuations caused by the local time-dependent magnetic fields cause the loss of this synchronization over time. This loss of coherence can be observed as a decaying transverse magnetization; hence it can be thought of as moving on a spiral-like trajectory in the transverse plane, as illustrated in figure 6.

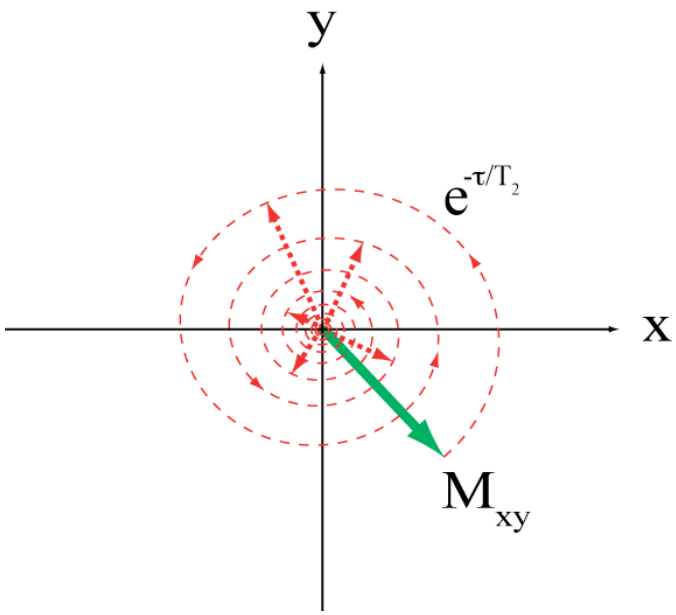

Figure 6 Vertical projection of the decaying transverse magnetization.

The rate of this decay is characterized by the transverse relaxation time constant, T_2, which is different from T_1. The exponential relaxation curve is shown in figure 7.

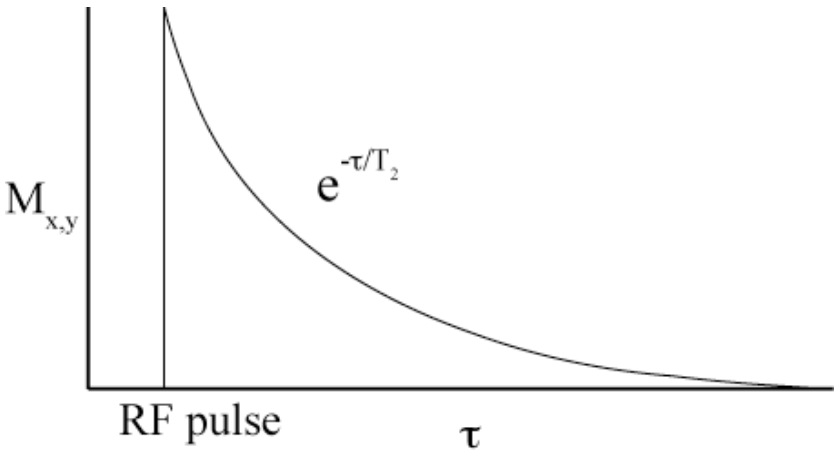

Figure 7 Decay of the transverse relaxation at a rate defined by T_2.

Ultimately, the relaxation processes cause the rotating magnetization vector to walk from the transverse plane to the direction of the applied magnetic field on the conical trajectory, as seen in figure 8.

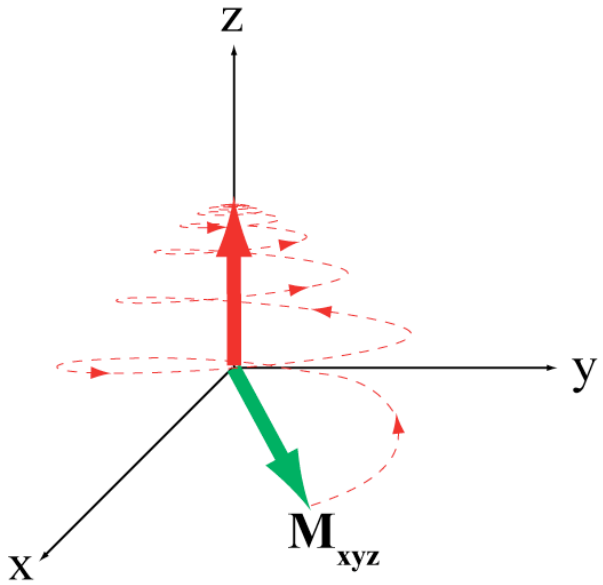

Figure 8 Relaxation of the transverse magnetization.

1.1.5 Free Induction Decay and NMR signal detection

The magnitude of the transverse magnetization is small; however, it is detectable. The rotating magnetic moment in the transverse plane gives rise to an oscillating magnetic field, which in turn induces an electric current in a coil with a winding axis along the *xy*-plane. This weak electric signal decays over time due to the transverse magnetization and is called a Free Induction Decay (FID). This time-dependent FID is amplified, digitized and subsequently transformed to the frequency domain via the Fourier transformation (FT). The resulting NMR spectrum, which is a plot of a signal intensity as a function of frequency, has a peak positioned at the Larmor frequency of the nucleus of interest. The process of signal detection for obtaining the spectrum is depicted in figure 9 below.

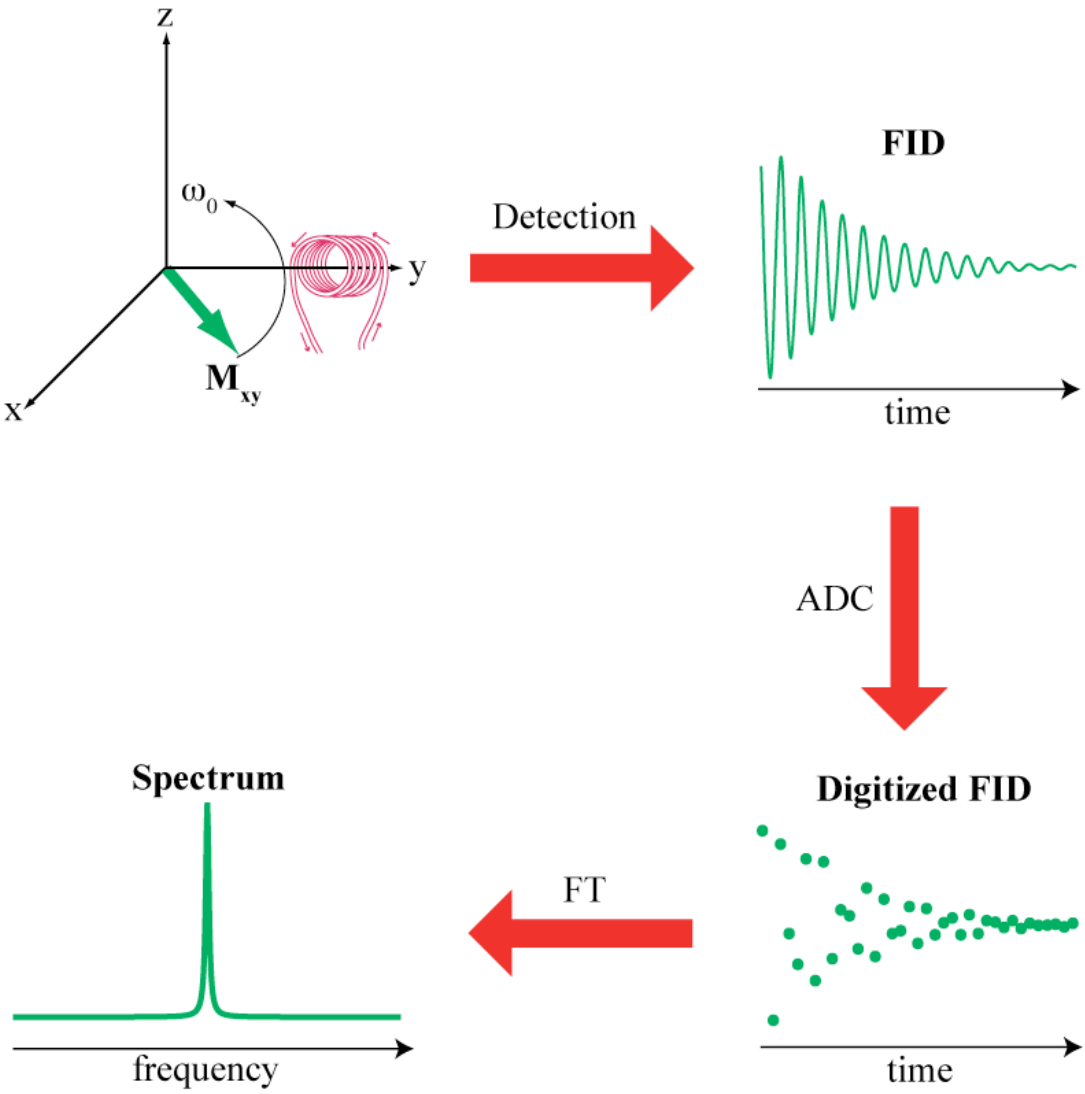

Figure 9 Design of NMR experiment.

NMR experiments are conventionally described with a pulse sequence timing diagram, which shows all experimental events in the order of their appearance in time. The very basic pulse sequence contains an excitation radiofrequency pulse, where its length is given by the angle by which it rotates longitudinal magnetization, followed by detection of the FID, as seen in figure 10. More advanced experiments include

decoupling and polarization transfer, and may involve multiple nuclei simultaneously, as well as several time dimensions, some of which will be explored further.

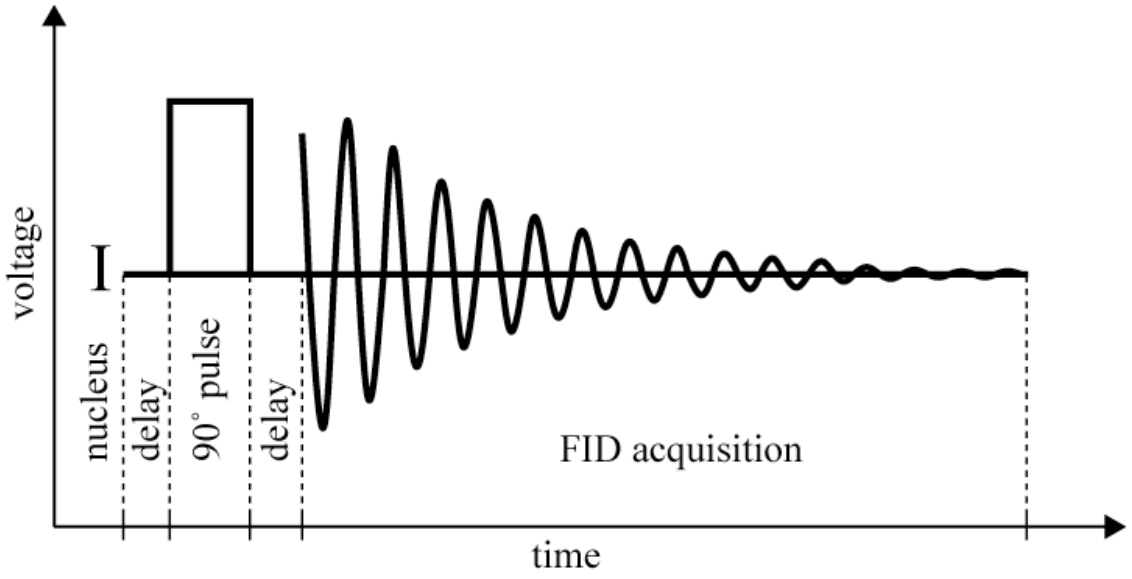

Figure 10 Pulse sequence diagram of a basic NMR experiment on nucleus **I**.

1.1.6 Chemical shift

In theory, an isolated spin-1/2 should give rise to a single peak, which is characterized by a Lorentzian distribution and appears at its Larmor frequency. In actual NMR experiments; however, this is not entirely the case. A phenomenon known as shielding causes a slight shift of the resonance frequency with respect to the Larmor frequency. The position of the signals is characterized by this offset frequency with respect to the Larmor frequency, which in turn is approximated by the frequency of a reference compound particular to each nucleus of interest. This is called the chemical shift and is expressed in parts per million (ppm) of the reference frequency, so that it is independent of the field strength used.

Shielding arises due to local magnetic fields $B_{induced}$ caused by currents in the electron density surrounding the nucleus that are induced by the applied magnetic field. As a result the net magnetic field experienced by the nucleus is altered, as shown in figure 11.

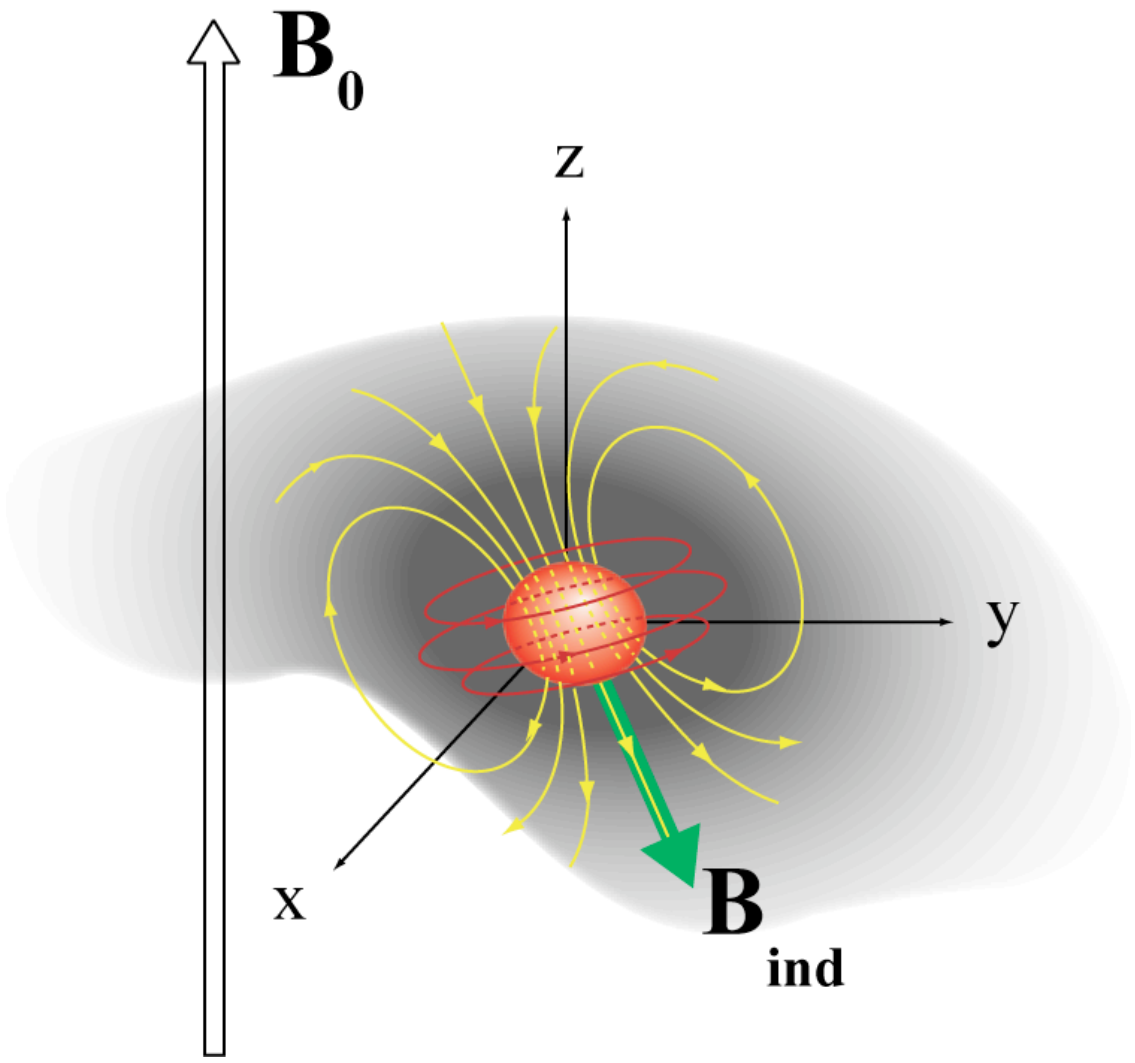

Figure 11 Magnetic field, $B_{induced}$, generated by currents in the electron cloud surrounding nucleus in the presence of the external magnetic field, B_0.

This shielding interaction depends on the orientation of the molecular frame in which the currents are generated, with respect to the external field, where the vector of the induced magnetization is related to the vector of the applied magnetic field through the chemical shift tensor, $\hat{\hat{\delta}}$, as follows:

$$\vec{B}_{induced} = \hat{\hat{\delta}} \cdot \vec{B}_0 \qquad (2)$$

Chemical shift tensor is described by a 3×3 matrix of the following form:

$$\hat{\hat{\delta}} = \begin{vmatrix} \delta_{xx} & \delta_{xy} & \delta_{xz} \\ \delta_{yx} & \delta_{yy} & \delta_{yz} \\ \delta_{zx} & \delta_{zy} & \delta_{zz} \end{vmatrix} \tag{3}$$

The tensor is represented in the laboratory frame and is often transformed to its own reference frame referred to as its Principal Axis System (PAS), shown in figure 12.

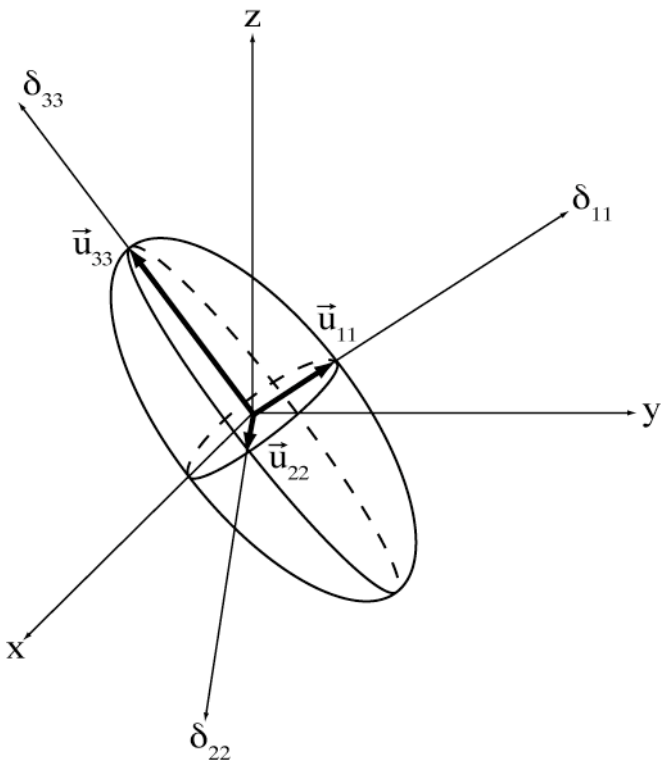

Figure 12 Principle Axis System of the chemical shift tensor.

The principal components of CS tensor, δ_{jj}, are its eigenvalues, and its eigenvectors, $\vec{u}_{jj}$, are the unit vectors defining the PAS frame. The corresponding eigen-representation of the tensor matrix is shown below:

$$\delta_{PAS} = \begin{vmatrix} \delta_{11} & 0 & 0 \\ 0 & \delta_{22} & 0 \\ 0 & 0 & \delta_{33} \end{vmatrix} \tag{4}$$

$$u = \left|\vec{u}_1\middle|\vec{u}_2\middle|\vec{u}_3\right| \tag{5}$$

$$\hat{\hat{\delta}} = u^{-1} \cdot \delta_{PAS} \cdot u \tag{6}$$

The average of the tensor is known as a relative isotropic chemical shift, δ_{iso}, and is defined as follows:

$$\delta_{iso} = \frac{1}{3}(\delta_{11} + \delta_{22} + \delta_{33}) \tag{7}$$

Correspondingly, the absolute isotropic chemical shift, σ_{iso}, has the similar form:

$$\sigma_{iso} = \frac{1}{3}(\sigma_{11} + \sigma_{22} + \sigma_{33}) \tag{8}$$

By convention, these shifts increase in opposite directions: $\delta_{11} \geq \delta_{22} \geq \delta_{33}$ and $\sigma_{11} \leq \sigma_{22} \leq \sigma_{33}$.[2, 3]

Recall that anisotropic nature of the shielding interaction causes a distribution in Larmor frequencies of nuclei when there is corresponding distribution in orientations, as in a powder sample. The range over which the distribution of frequencies occurs is defined by the chemical shift anisotropy (CSA), $\Delta\sigma$, which has the following form:

For $\delta_{33} - \delta_{iso} > \delta_{11} - \delta_{iso}$ and $\sigma_{33} - \sigma_{iso} > \sigma_{11} - \sigma_{iso}$,

$$\Delta\sigma = \delta_{33} - \frac{\delta_{22} + \delta_{11}}{2} \tag{9}$$

for $\delta_{33} - \delta_{iso} < \delta_{11} - \delta_{iso}$ and $\sigma_{33} - \sigma_{iso} < \sigma_{11} - \sigma_{iso}$,

$$\Delta\sigma = \delta_{11} - \frac{\delta_{22} + \delta_{33}}{2} \tag{10}$$

The shape of the distribution is characterized by the chemical shift asymmetry parameter, η_{CS}:

For $\delta_{33} - \delta_{iso} > \delta_{11} - \delta_{iso}$ and $\sigma_{33} - \sigma_{iso} > \sigma_{11} - \sigma_{iso}$,

$$\eta_{CS} = \frac{\delta_{22} - \delta_{11}}{\delta_{33} - \delta_{iso}} \tag{11}$$

for $\delta_{33} - \delta_{iso} < \delta_{11} - \delta_{iso}$ and $\sigma_{33} - \sigma_{iso} < \sigma_{11} - \sigma_{iso}$,

$$\eta_{CS} = \frac{\delta_{22} - \delta_{33}}{\delta_{11} - \delta_{iso}} \tag{12}$$

The CSA interaction affects the spectra in liquids and solids very differently. In liquids, rapid molecular motion averages out the anisotropy of spin orientations leaving one narrow peak at isotropic chemical shift, δ_{iso}. On the other hand, the rapid motion causes the CSA term to give rise to randomly fluctuating fields and thus provides a very efficient relaxation mechanism. As a result molecules with large CSA's can have very

different relaxation times from those with much smaller CSA's depending on experimental conditions such as temperature and viscosity. Solid-state experiments are normally performed on powders, which consist of a large number of crystals, each having different orientation with respect to the applied magnetic field. Consequently the CSA causes inhomogeneous broadening of the signal. The broad shape of the signal is a result of superimposition of peaks with different chemical shifts due to the various crystal orientations, and is referred to as a powder pattern (shown in the top of figure 13).

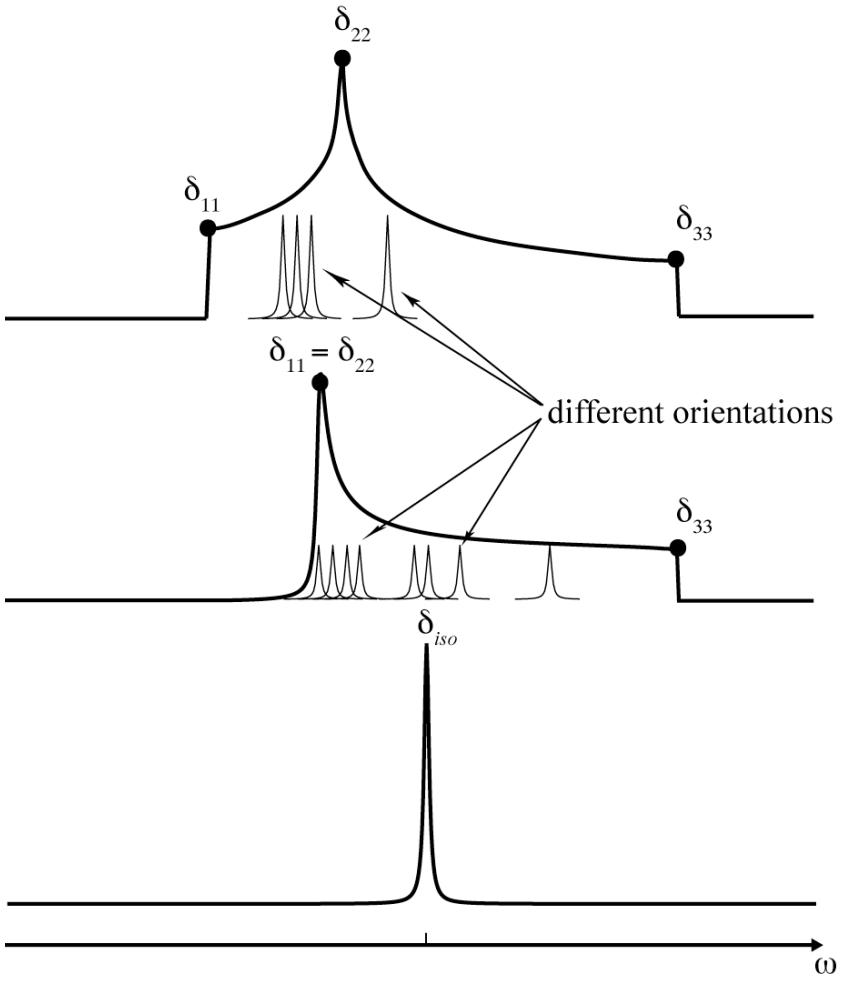

Figure 13 Inhomogeneous line broadening mechanisms in NMR spectra caused by CSA. Powder pattern characterized by three different tensor components (top); powder pattern characterized by reduced chemical shift tensor in the case of axial symmetry along bond axis (middle); single peak at δ_{iso} as a result of fast isotropic motion (bottom).

Tensor components can be scaled down in molecules that exhibit fast dynamics. For example, a methyl group that has rapid rotation about the CH_3–X bond axis which leads to axial symmetry in the tensor along the bond resulting in two of its principal components becoming equal (figure 13, middle). Finally, fast isotropic motion causes all three tensor components to become equalized; hence, all orientations have the same shielding, leaving one narrow peak at δ_{iso}, as seen in the bottom of figure 13. In short, the symmetry reflected by the tensor components is the result of a combination of the symmetry in the electron density surrounding the nucleus and the symmetry of any motion that the system undergoes.

1.1.7 Dipolar and quadrupolar interactions

The magnetic moment of a nuclear spin may interact with a magnetic field due to the magnetic moment of another spin. This interaction is called spin-spin coupling and can occur between spins of the same (homonuclear) or different type of nuclei (heteronuclear). There are two types of coupling possible: one is a direct interaction between the spins while the other is mediated through the electrons and is referred to as indirect coupling (J-coupling). In the latter case, the magnetic moment of one spin polarizes surrounding electrons, which in turn induces a magnetic field at the site of the second spin. This indirect dipole-dipole interaction makes spins sensitive to their neighboring spins and gives rise to the multiplet peak structure observed in the spectra of most liquids. This is most routinely employed in determination of molecular structures,

via solution-state NMR. The J-coupling is also observed in the solid state, where it is orientationally dependent. Only its isotropic value is observed in solution.

Couplings can also be experienced directly between the magnetic dipole moments of nuclei through space, which is known as direct dipolar coupling, *D*. This interaction is proportional to the angle between the coupling vector and the direction of the external magnetic field (as seen in figure 14), and is inversely proportional to the cube of the internuclear distance. It is characterized by a traceless tensor, which means that its isotropic value is zero.

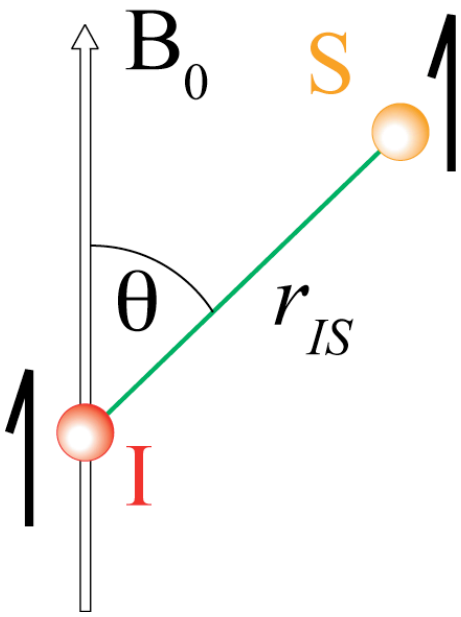

Figure 14 The direct dipolar coupling between two spins, **I** and **S**, in the presence of an external magnetic field, B_0.

On one hand, the latter implies that the direct dipolar coupling is lost in liquids due to the fast molecular motion; however, on the other hand it can be very strong in solids, 100's

Hz to 100's kHz. The coupling constant D_{IS} between spin **I** and spin **S** is proportional to their gyromagnetic ratios, γ_I, γ_S, and the internuclear distance, r_{IS}, as follows:

$$D_{IS} = \frac{\hbar \mu_0 \gamma_I \gamma_S}{4\pi r_{IS}^3} \tag{13}$$

Strong homonuclear couplings give rise to homogenous line broadening, which can severely limit spectral resolution. Such interactions are especially strong and frequent in the case of abundant nuclei with large gyromagnetic ratios, such as ^{1}H, where linewidths of 10's to 100's of kHz are common and spectra lack sufficient resolution to give detailed structural information. Consequently, it is not commonly used. In contrast, ^{13}C is only 1% abundant and has a small gyromagnetic ratio, which results in weak rarely occurring homonuclear interactions. Hence, no homogeneous line broadening occurs and high resolution is possible with modest spinning rates. Thus, ^{13}C MAS spectroscopy is routinely used. Heteronuclear interactions do not give rise to homogeneous line broadening and can be efficiently suppressed using decoupling sequences, which will be explored further. Ultimately, it is crucial to have experimental control over coupling so that it can be suppressed to improve spectral resolution, and reestablished to measure internuclear distances.[4-7]

The nuclear spin interactions become further complicated in the case of quadrupolar nuclei (spin >1/2). In such a situation the electric charge distribution is no longer spherically symmetrical and interacts with surrounding magnetic fields depending on the geometry and orientation of nuclei within the molecule. In solution, this often leads to very rapid relaxation of the quadrupolar nucleus and any other nucleus strongly coupled to it. This causes such nuclei to be very difficult to observe. This interaction is beyond the scope of this work and is the subject of an entire sub-discipline of NMR

where unique techniques have been developed to obtain high resolution from lineshapes that are anywhere from tens of kHz to several MHz wide.

1.1.8 Magic Angle Spinning

Dipolar coupling interactions are dependent on the direction of the coupling vector with respect to the external magnetic field, which is given by the following equation:

$$D(\theta) \propto \frac{1}{2}(3\cos^2\theta - 1) \tag{14}$$

The dipolar coupling can be eliminated if the coupling vector between two spins is inclined with respect to the direction of the applied field by an appropriate angle, referred to as a magic angle and given by:

$$\theta = \arccos\frac{1}{\sqrt{3}} \approx 54.74° \tag{15}$$

The magic angle can be represented as an angle between the *z*-axis and the body diagonal in a unit cube. Rotating an object about the direction of this diagonal would equally interchange its respective *x,y,z* coordinates and give rise to an equivalent to isotropic motion, as seen in the left hand side of figure 15. Magic Angle Spinning (MAS) NMR experiments on a solid attempts to average out the orientational dependence of the nuclear spin interactions and reduces the inhomogeneous and homogeneous broadening, significantly improving the spectral resolution[8-11] (shown in figure 15, right).

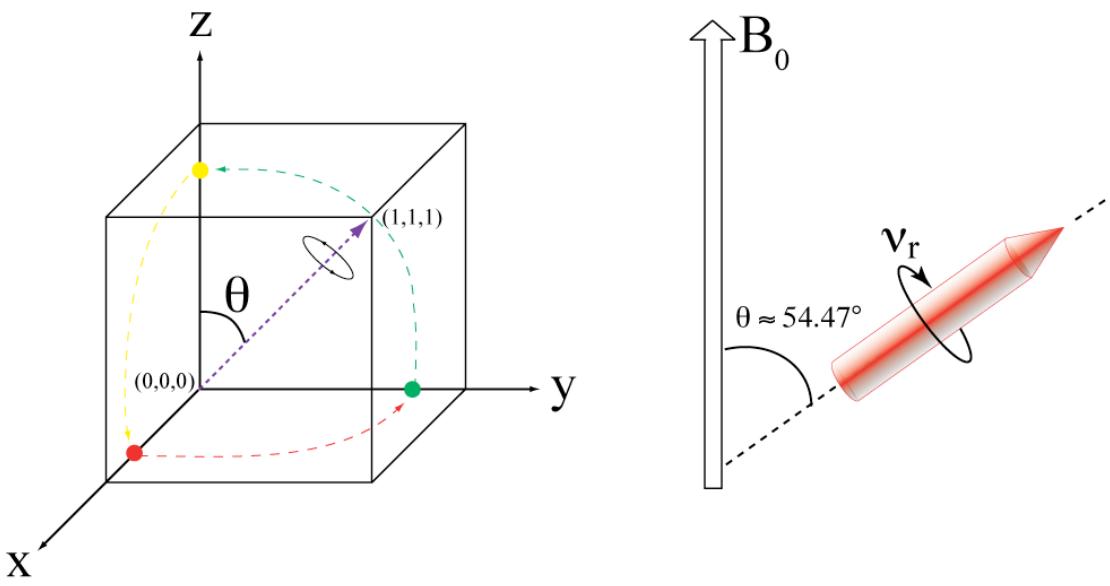

Figure 15 Geometrical interpretation of the magic angle (left); sample rotation at the magic angle in solid-state NMR (right).

Strong homonuclear couplings that give rise to extreme homogeneous line broadening can only be effectively suppressed at spinning speeds exceeding several times the strength of the coupling interactions. This is not often achievable at even modern limits of spinning speed for ^{1}H and in some materials for ^{19}F and ^{31}P as well, where high resolution can remain elusive. On the other hand, heteronuclear coupling leads to inhomogeneous line broadening which is effectively removed under MAS conditions. If the interactions are too strong to be removed by MAS, the spectrum will exhibit a pattern of side-bands, where the isotropic line is surrounded by line on both sides separated in frequency by the spinning speed, as seen in figure 16.

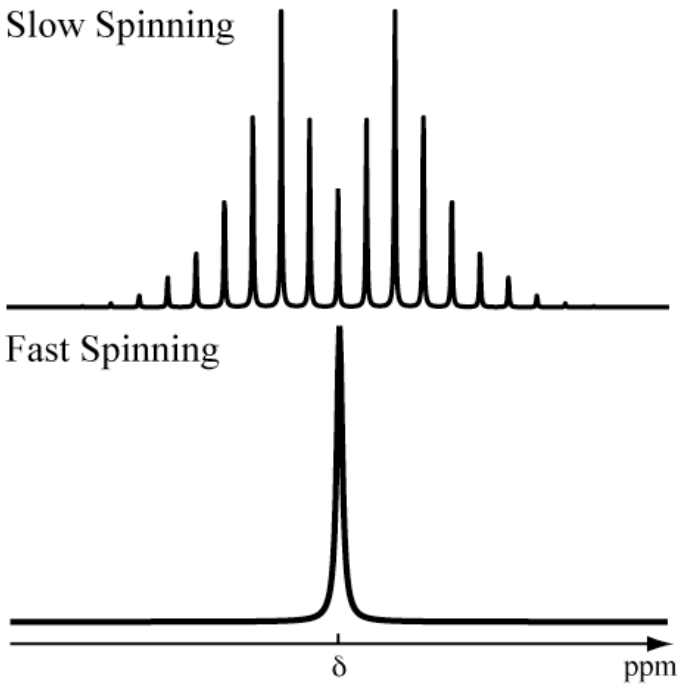

Figure 16 MAS NMR spectrum with a sideband pattern due to insufficient spinning speed (top); the same spectrum but obtained at higher spinning speed (bottom).

1.1.9 Decoupling

As mentioned earlier, strong dipolar spin interactions may result in splitting patterns and inhomogeneous line broadening in NMR spectra. Even though coupling constants may provide useful information about spin surroundings and atomic distances, these interactions often limit the spectral resolution and hence need to be removed using RF pulse sequences. Decoupling sequences form a class of NMR techniques employed in both liquids and solids to remove heteronuclear spin coupling interactions. They are implemented to match the particular needs of an NMR experiment and limitations of the instrument. Two such sequences to be used in all solid-state NMR work to be presented

are Two Pulse Phase Modulation (TPPM)[12] and XY-16[13, 14] decoupling sequences and will be explained further.

TPPM heteronuclear decoupling consists of a train of RF pulses with a length of one rotation period, τ_r, and alternating phases ($-\phi/2$, $+\phi/2$, $-\phi/2$…), as illustrated in figure 17.

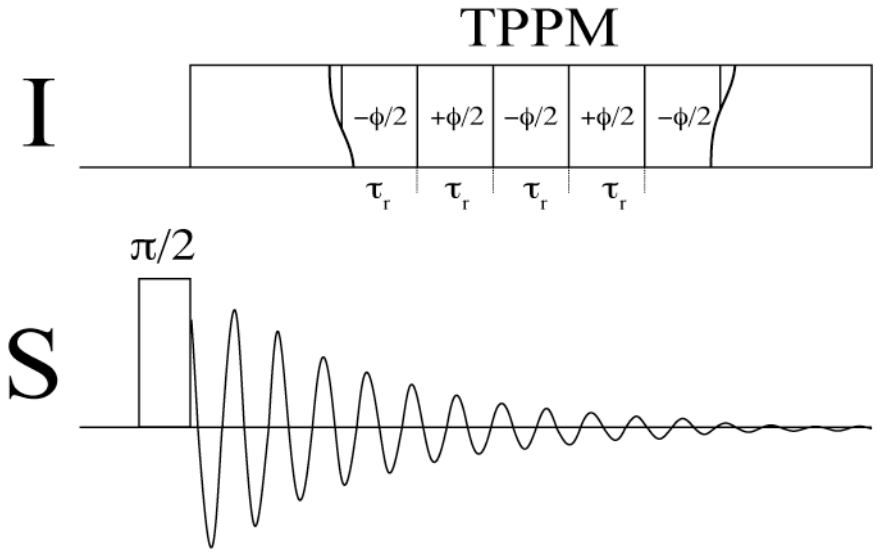

Figure 17 Pulse sequence diagram of an MAS NMR experiment with TPPM heteronuclear decoupling of spin **I**.

It has been shown that TPPM decoupling is significantly more efficient in removing the heteronuclear couplings under MAS conditions compared to conventional continuous-wave (CW) irradiation, which is often degraded in strongly coupled systems due to perturbations caused by CSA and magnetic susceptibility fields. In addition, rotor-synchronized $\pm\phi/2$ phase modulation reduces offset-dependence of the heteronuclear

decoupling, increasing its performance, in particular for nuclei with a broad frequency ranges such as ^{19}F.[12]

In some cases even further improvements of the heteronuclear decoupling efficiency can be achieved using a Carr-Purcell-type sequence with an XY-16 phase cycle. This consists of 16 repetitive rotor-synchronized high-power π *(xyxy yxyx -x-y-x-y -y-x-y-x)*$_n$ pulses applied on nucleus **I** simultaneously with windowed acquisition of nucleus **S** at the end of each rotation period, as shown in figure 18.

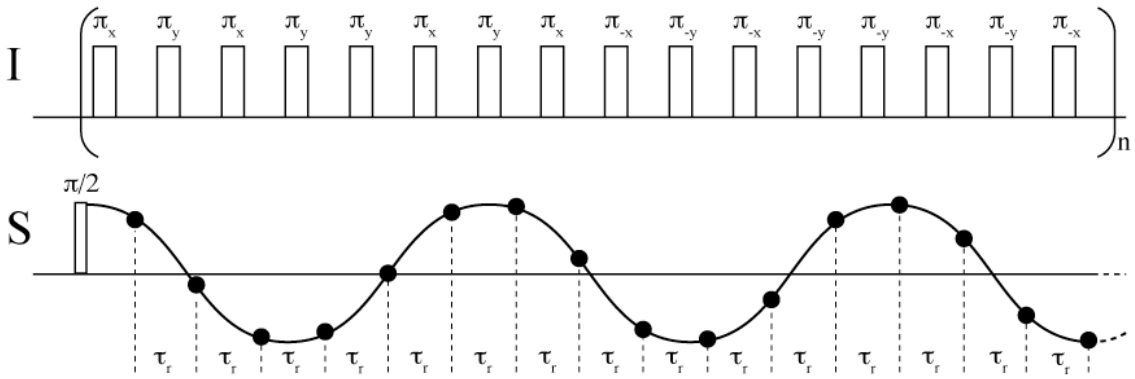

Figure 18 A Carr-Purcell-type rotor-synchronized decoupling sequence with an XY-16 phase cycle on spin **I** and simultaneous detection of spin **S** at the end of each rotation period.

This decoupling sequence provides very efficient compensation of pulse imperfections and avoids short duty cycles, τ_π/τ_r. As a result, signal detection can occur on a longer time scale, as the π pulses can be applied at higher power for longer periods, when spaced by delays, avoiding breakthrough to the detection channel. XY-16 decoupling is very effective in removing the residual heteronuclear dipolar and J-couplings under MAS conditions.[14] Application of the rotor-synchronized 180º pulses with such phase cycling results in the refocusing of the J_{IS} interactions at the end of each rotation period, causing

them to be efficiently suppressed during the windowed rotor synchronized detection on **S**. Furthermore, if an experiment in which simultaneous irradiation on multiple channels is required, the application of XY-16 decoupling does not impose power limitations that CW and TPPM do, and hence can be readily applied to several nuclei (*eg.* $^{13}C\{^{1}H,^{19}F\}$), dramatically improving the spectral resolution. Two examples include ^{13}C MAS NMR studies of fluoropolymers[14] and polyphosphazene[15] using XY-16 decoupling, where very high spectral resolution was obtained.

1.1.10 Spin-lattice relaxation in the rotation frame

Another property that is routinely measured in the study of relaxation and dynamics is the spin-lattice relaxation in the rotating frame, $T_{1\rho}$.[1,2,16,17] Experimentally $T_{1\rho}$ is measured by rotating the longitudinal magnetization to the transverse plane by the means of a $\pi/2$ pulse with subsequent application of a lower amplitude pulse with the same phase as the resulting transverse magnetization for the duration of τ. This second long low amplitude pulse is referred to as the spin-locking pulse, or field, and is applied on the order of milliseconds, as opposed to microseconds for ordinary $\pi/2$ pulses.

The most commonly used pulse sequence for measuring $T_{1\rho}$ is depicted in figure 19. If the field strength is large enough, the spin magnetization is then locked and precesses about the *x*-axis. At this time the magnetization is locked into position along the axis corresponding to the phase of the locking pulse during which it decays according to a T_1 like process governed by the time scale of the locking power and not the Larmor frequency. After period τ, B_1 is turned off, releasing the transverse magnetization, which

is then allowed to freely precess and be detected. The behavior of the magnetization vector during the spin-lock experiment is illustrated schematically in figure 20 below.

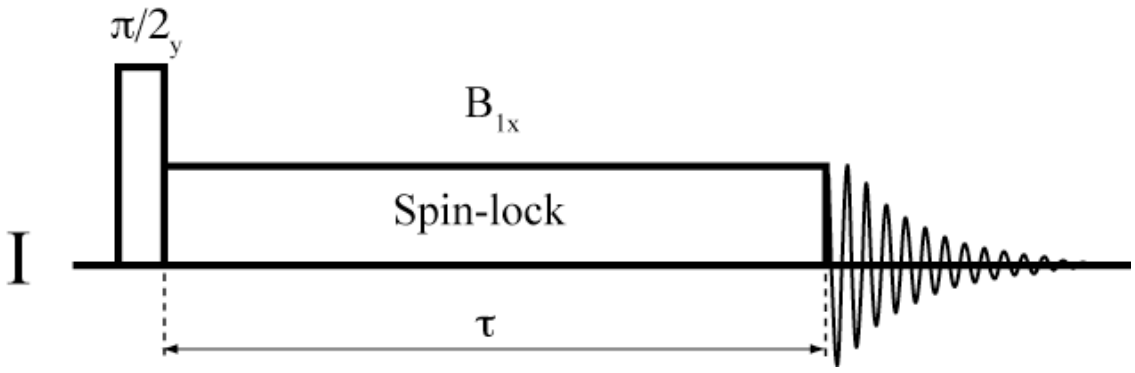

Figure 19 A basic spin-lock pulse sequence for measuring $T_{1\rho}$.

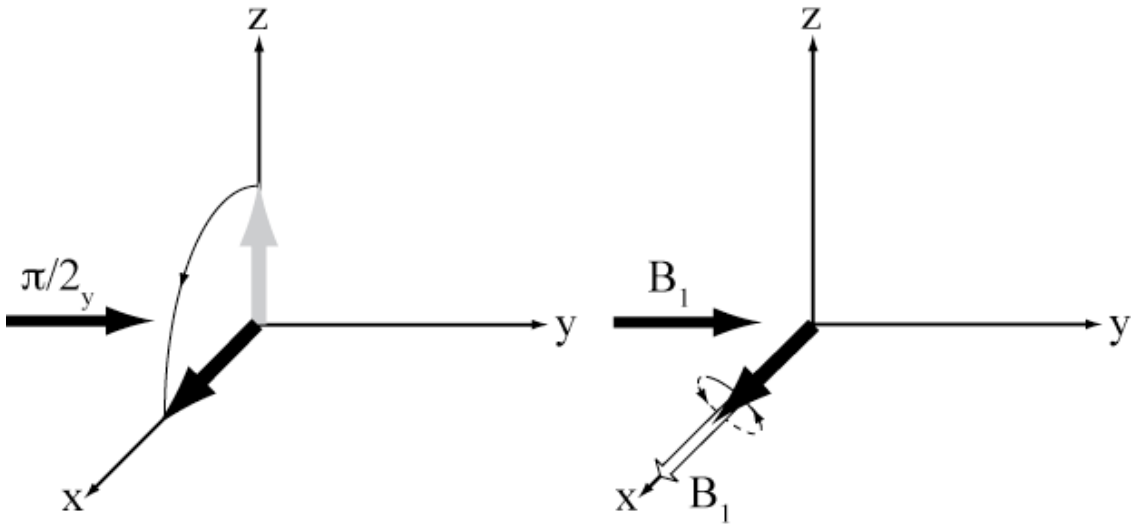

Figure 20 Magnetization vector in the spin-lock experiment.

The magnetization decays as a function of spin-lock time τ as follows:

$$M_x = M_0 e^{-\frac{\tau}{T_{1\rho}}} \tag{16}$$

By measuring intensities of the decaying signal at different spin-lock times, the time constant of the process, $T_{1\rho}$, can be easily obtained. This technique allows for probing the molecular dynamics that occur on a slower scale, which is usually inaccessible by conventional T_1 and T_2 measurements.[18, 19]

1.1.11 Polarization transfer

Low γ and natural abundance nuclei (^{13}C, ^{15}N etc) result in a weak NMR signal, which can be further dispersed by the ever-present heteronuclear couplings to other nuclei. In order to improve the quality of such spectra, either synthetic enrichment of the material with NMR-detectable isotopes or drastically increased experimental times, are required, both of which are extremely expensive and impractical. These problems can be circumvented using cross-polarization (CP), which involves magnetization transfer from an abundant nucleus, to a rare nucleus of interest.[1, 3] CP employs flip-flop transitions, mutual 'up-down/down-up' transitions, that can only be experienced between homonuclear coupled spins, and hence is negligible in rare nuclei. However, a heteronuclear flip-flop transition can be induced via simultaneous spin-locking of an abundant spin **I** and a rare spin **S**, which under appropriate conditions equalizes their frequencies. CP establishes a new equilibrium in the spin polarizations as determined by the ratio of their gyromagnetic ratios:

$$\frac{P_{0I}}{P_{0S}} = \frac{\gamma_I}{\gamma_S} \tag{17}$$

In principle, $^{1}H \rightarrow {}^{13}C$ cross-polarization results in an enhancement factor of:

$$\frac{267.522 \cdot 10^{6} \text{ rad s}^{-1} \text{ T}^{-1}}{67.283 \cdot 10^{6} \text{ rad s}^{-1} \text{ T}^{-1}} \approx 4 \tag{18}$$

In solids, transfer from spin **I** to spin **S** can be established by creating a transverse magnetization from spin **I**, via a $\pi/2$ RF pulse with an appropriate phase, and subsequently applying spin-locking fields B_{1I} and B_{1S} on both spins simultaneously, along the direction of the magnetization of spin **I**. The spin locking powers on both channels must meet the Hartmann-Hahn condition ($\gamma_I B_{1I} = \gamma_S B_{1S}$), thereby equalizing both spin frequencies ($\omega_{1I} = \omega_{1S}$), promoting mutual heteronuclear spin flop transitions, and leading to build-up of the spin **S** magnetization along the B_1 axis during the course of the contact period. When the spin-lock terminates on both channels, it is followed by simultaneous detection of spin **S** and decoupling of spin **I**, as shown in figure 21.

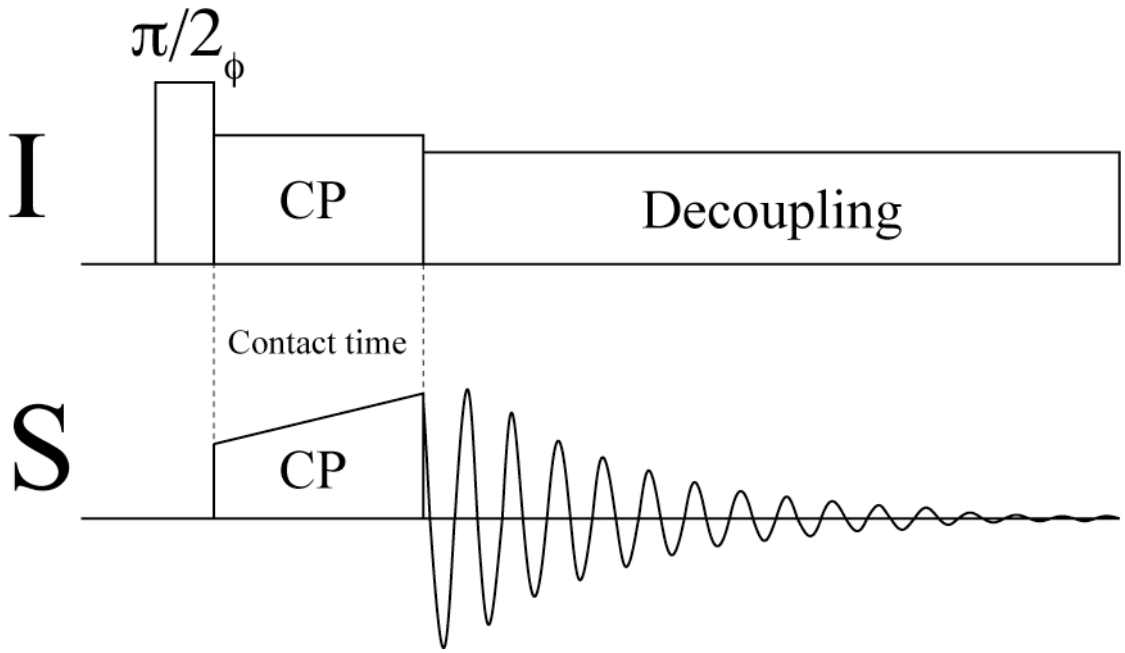

Figure 21 Pulse sequence of an MAS NMR experiment with Hartmann-Hahn polarization transfer from abundant spin **I** to rare spin **S**.

The duration of the spin-lock is limited by the $T_{1\rho}$ of spin **I** and is referred to as contact time. The rate of polarization transfer, k_{IS}, is determined by an average dipolar coupling between the two spins. The dynamics of the **I** → **S** CP can be characterized by $T_{1\rho}$ and k_{IS} as shown in the CP curves in figure 22.

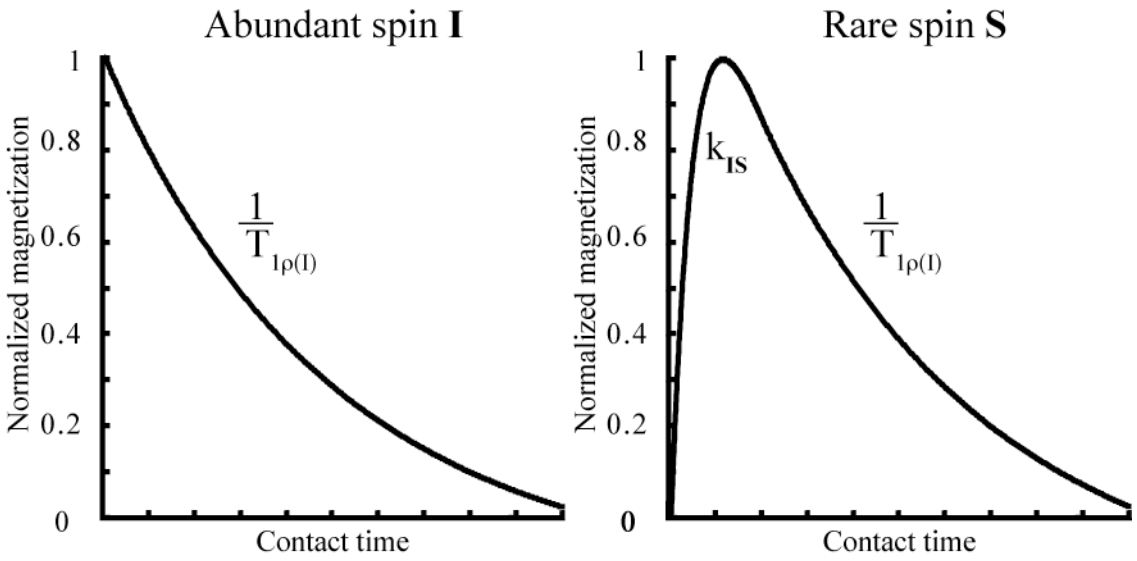

Figure 22 Dynamics of polarization transfer from an abundant spin **I** to rare spin **S**.

The magnetization of an abundant spin exponentially decreases from its maximum as the contact time increases, at a rate 1 / $T_{1\rho(I)}$, while that of a rare spin grows at a rate determined by k_{IS}, reaching a maximum and subsequently decaying at a rate determined by $T_{1\rho(I)}$.

In conclusion, the development of cross-polarization techniques revolutionized modern NMR in solids and made it a routine operation. CP provides a several-fold enhancement of the signal to noise ratio for weak nuclei on a per scan basis. In addition, it allows for a faster scanning rate as it is limited by $T_{1\rho(I)}$ rather than $T_{1(S)}$, which is always longer, often by orders of magnitude. As a result the signal to noise ratio over a fixed experimental duration is improved dramatically. In CPMAS CP is combined with MAS, offering both vastly improved resolution with greatly increased signal to noise, making it possible for SSNMR to become a routine technique in material science.

1.1.12 Multidimensional NMR

In conventional one-dimensional NMR experiments, spin coherence created during the experiment is observed as a function of one time variable, and the corresponding spectrum is constructed by plotting signal intensity as a function of one frequency variable. However, this approach is very limiting as much information can be obtained by observing the spin system changing (evolving) over time. Furthermore, analyses of NMR spectra may become an impossible task as with large and complex molecular structures, one-dimensional spectra can become hopelessly crowded and impossible to interpret. Such spectra can be significantly simplified with multidimensional NMR spectroscopy, where the signal is detected as a function of several time variables. 2D NMR experiments allow the observation of correlations between peaks in the spectrum, due to spin-spin interactions that can be controlled using RF pulses, which provide detailed insight about connectivities between spins, inter- and intra-molecular distances and molecular structures in both liquids and solids. Two-dimensional methods are composed of a series of specific experimental operations performed during each of four time periods: preparation, evolution, mixing and detection, as shown in figure 23.

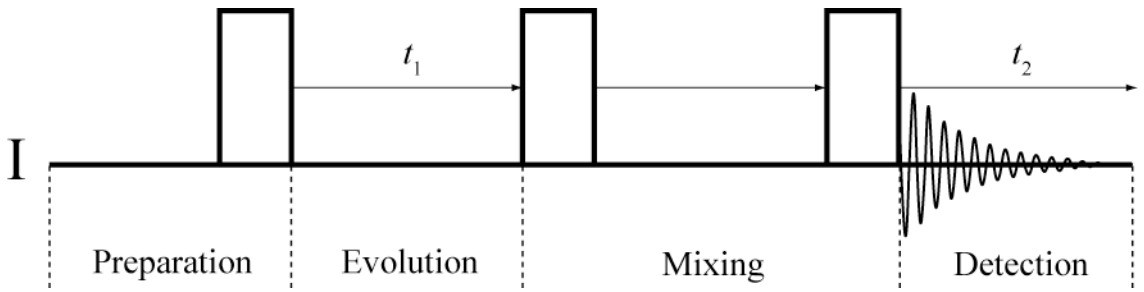

Figure 23 A general pulse sequence diagram of 2D NMR experiment.

During the preparation phase, spin coherence and the transverse magnetization are created, normally with a 90º RF pulse or polarization transfer from another nucleus, from a system that was allowed to return to equilibrium beforehand. Spins are subsequently allowed to freely precess at their Larmor frequency during the evolution period, t_1. Sometimes the system is subject to decoupling using decoupling sequences during this time. Additional operations performed on a spin system during the mixing period cause the magnetization transfer between spins according to a chosen mechanism determined by the pulse sequence, and normally allow for the establishment of coherences via through-space or through-bond spin-spin interactions. Ultimately, by the end of the mixing period a detectable coherence is created on the nucleus of interest. The pulse sequence ends with the detection period, during which the signal is observed as a function of a second time variable, t_2, often under decoupling conditions.

The value of t_1 is incremented, and the sequence is repeated for each point in the indirect time dimension, thereby creating an array of FID's that constitute a data set that is two-dimensional in time S (t_1, t_2). This signal is then converted from time domains to the corresponding frequency domains, F_1 and F_2, via double Fourier transformation, as illustrated in figure 24. Finally, the 2D spectrum is displayed as a contour map plot with frequency axes labeled F_1 and F_2, correlations between the spins shown as a vertical projection of signal intensities, and the peak coordinates reflecting respective frequencies. A basic two-dimensional chemical shift correlation spectroscopy (COSY)[2] spectrum of an AX spin system is seen in figure 25.

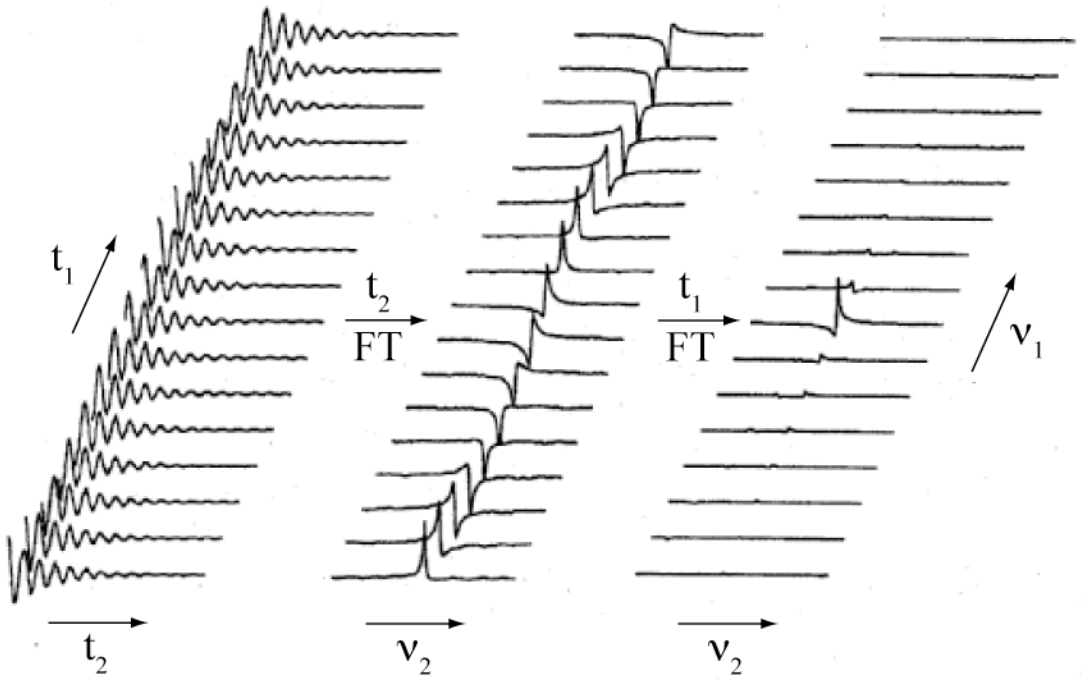

Figure 24 Structure of a two-dimensional NMR experiment.

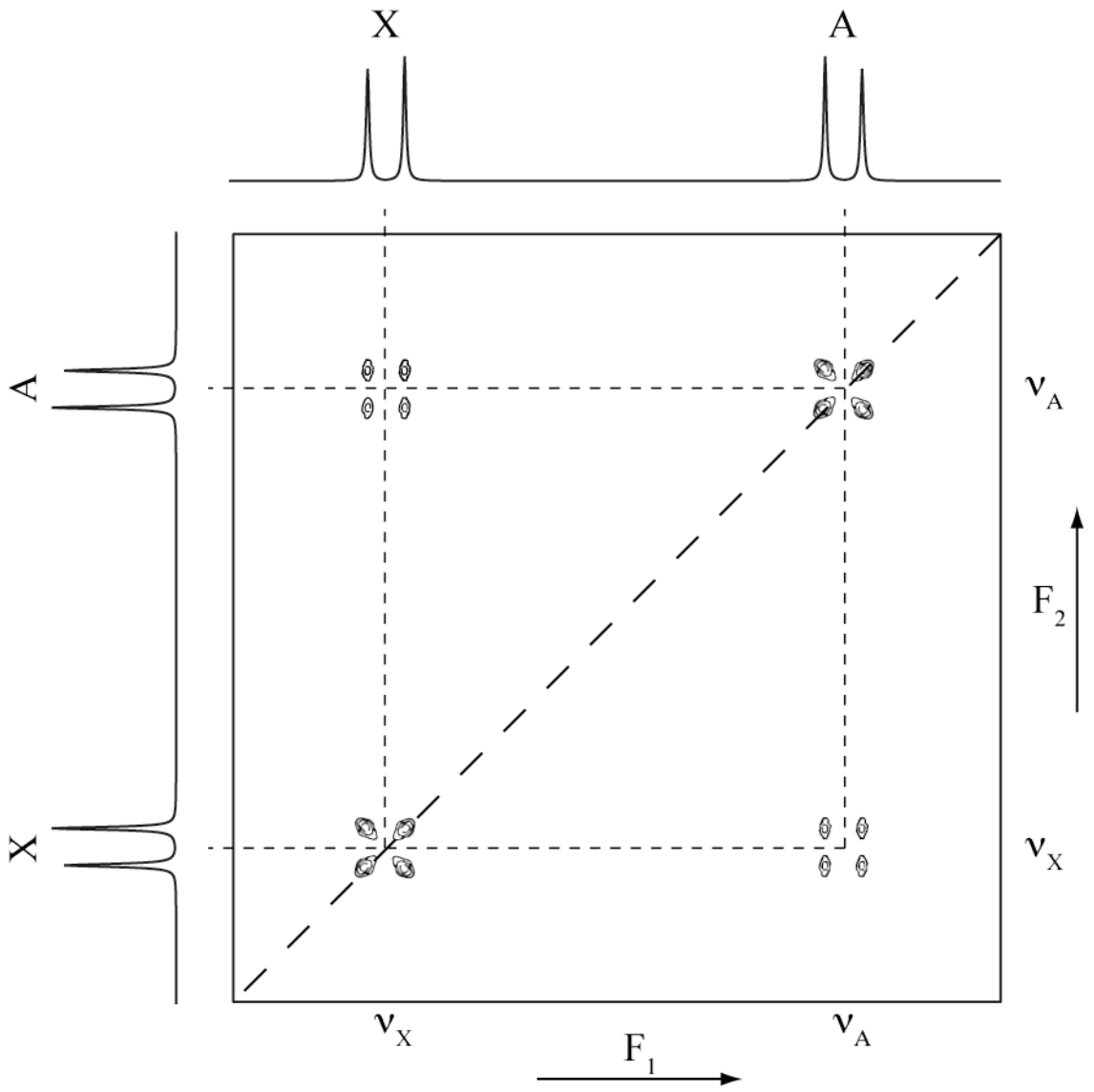

Figure 25 2D COSY spectrum of an AX spin system.

In one-dimensional NMR experiments, the corresponding FID of the AX spin system would contain two signals, upon which Fourier transformation would give rise to two peaks appearing at ν_A and ν_X and split in doublets due to J-coupling. The 2D COSY spectrum of this spin system shows two groups of peaks along the diagonal at (ν_X, ν_X) and (ν_A, ν_A) which show homonuclear correlations for spin X and A, respectively. Two

off-diagonal sets of peaks referred to as cross-peaks characterize the homonuclear magnetization transfer that occurred between the coupled spins and therefore provide information about their connectivity, and often their relative geometry.

A basic two-dimensional NMR experiment can be designed to suit the requirements for specific applications. This can be achieved by making modifications to the pulse sequence that enable specific coherence transfer mechanisms through desired coherence pathways,[20-31] two of which will be discussed in the following treatment.

1.1.13 Two-dimensional INADEQUATE experiment

2D INADEQUATE (Incredible Natural Abundance DoublE QUAntum Transfer) leads to discrimination between signals from J-coupled spin pairs and isolated spins, where the latter can be eliminated through a series of pulses executed in a two-step phase cycle. Originally developed as a solution NMR technique[32] , it was later adapted for experiments in solids under MAS conditions. During the preparation period, a spin echo sequence is applied, $\pi/2_x - \tau - \pi_y$, resulting in the anti-phase magnetization on both spins in the spin pair, which are converted to a double quantum coherence by the subsequent $\pi/2_x$ pulse. At this point the magnetization from isolated spins end up along the *–z* axis. The double quantum coherences evolve during t_1 according to the sum of chemical shifts only, as they do not evolve under J-coupling. The next $\pi/2_{x/y}$ pulse causes these double quantum coherences to be converted into single quantum anti-phase magnetization, although this time on the other spin in the spin pair, thus completing the coherence

transfer process. The phase of this π/2 pulse is cycled between two successive acquisitions so that only the anti-phase magnetization can be detected; however, in order to allow for decoupling, it needs to be converted to the in-phase magnetization, via application of τ–π–τ refocusing pulse. Correspondingly, this experiment is referred to as the Refocused INADEQUATE; the pulse sequence is shown in figure 26.

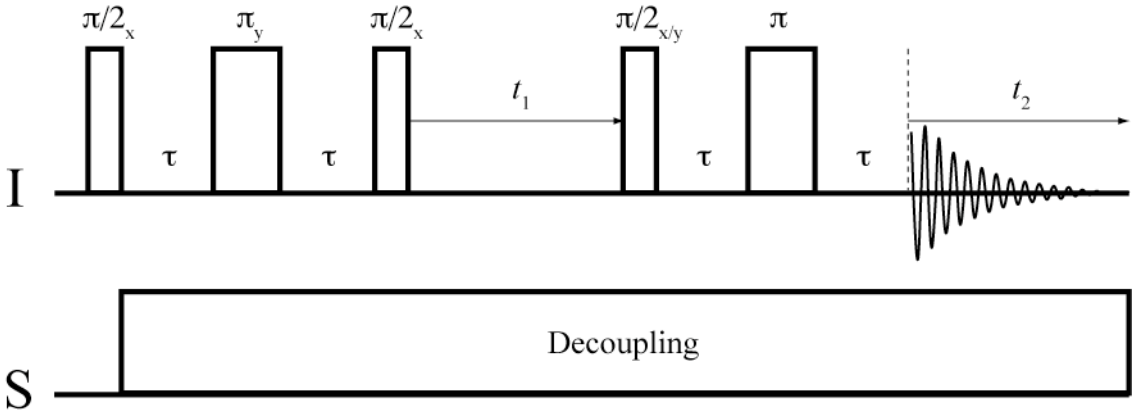

Figure 26 Pulse sequence of the two-dimensional refocused INADEQUATE MAS NMR experiment.

1.1.14 Two-dimensional RFDR experiment

As mentioned earlier, dipolar coupling is effectively averaged out under MAS conditions in solid-state NMR; however, in some cases this coupling information is desired to measure internuclear distances or to simply establish connectivities for molecular structure elucidation. A number of experiments allow dipolar interactions to be reintroduced by the application of a series of RF pulses. One such technique is a two-dimensional experiment referred to as Radio Frequency Driven Recoupling (RFDR). [33] In this method mixing of the longitudinal magnetizations is achieved using a series of rotor-synchronized π pulses that interfere with the averaging of the dipolar coupling during MAS. This reintroduced dipolar coupling causes longitudinal spin polarization to exchange leading to correlation between spins with different chemical shifts. The sequence then terminates with a $\pi/2$ pulse converting the longitudinal magnetization back to the transverse coherence that can be detected. A pulse sequence diagram for the RFDR experiment is shown in figure 27. The corresponding 2D spectrum then contains cross-peaks between dipolar-coupled spins, from which intra-molecular connectivities can be determined.

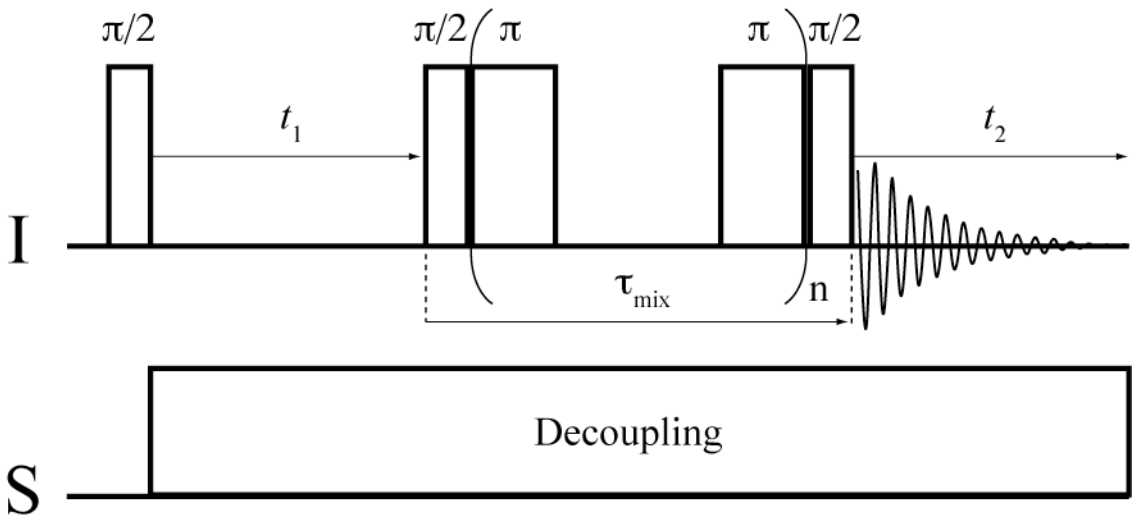

Figure 27 Pulse sequence of the two-dimensional RFDR MAS NMR experiment.

1.2 Polymers

1.2.1 Introduction to polymers

A polymer is a large macromolecule composed of smaller repeating structural units. Polymers that consist of the same type of repeating units are referred to as homo-polymers, whilst those that contain several non-identical repeating units are called co-polymers, or block co-polymers.[34]

Depending on the nature of the elements composing the repeating units, polymers are arbitrarily classified as organic, inorganic or biological. This contribution will be primarily focused on inorganic polymers.

Inorganic polymers can be further classified as fully inorganic, i.e. entirely comprised of inorganic elements, as organic-inorganic hybrid or organometallic polymers, containing inorganic elements in the backbone or side-chains. They offer a number of significant advantages over their organic counterparts, such as increased chemical resistance, thermal stability and mechanical durability. The unique composition of inorganic polymers efficiently reduces problems arising from aging, degradation, toxic fumes emission upon ignition, etc., usually associated with organic polymers. A variety of elements found in the backbone and side-chains allows tailoring of chemical and physical properties of the polymer to suit specific applications, which can range from very basic to high-performance, such as electronics components and biomedical materials.[35, 36] In addition, the relatively low cost of mass-production of polymer materials and the mild conditions under which they can be processed into usable objects,

make them commercially more preferred over other conventional materials with similar properties, such as metals.

Ultimately, inorganic polymers comprise a rapidly growing field of material science, where new materials with unique properties are constantly being developed and reported.[35, 36] The following sections will give a brief introduction to the most commonly studied and utilized classes of inorganic and organometallic polymers, covering their structures, syntheses, basic properties and most interesting examples of their application.

1.2.2 Silicon-based polymers

Polysilanes

Polysilanes are a very promising class of inorganic polymers and are composed of a linear backbone of continuous silicon atoms. They were first synthesized by Kipping in 1921,[37] and are most commonly obtained today via either polycondensation reactions or ring-opening polymerization.[34,37] A general structure of the polysilane repeating unit is shown in figure 28 below.

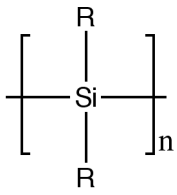

Figure 28 A general structure of the polysilane repeating unit.

Typically, polysilanes have relatively low glass transition temperatures, and their physical properties depend on the size and character of units in the side-chains. Polymers

with small and identical side-chain groups such as CH_3, are highly crystalline and insoluble solids; however, the crystallinity decreases when units of larger size or with dissimilar structures are attached to Si in the backbone. Polysilanes exhibit unique behavior due to σ-delocalization in the Si–Si bond,[38, 39] which gives rise to very useful properties such as electro- and photoconductivity, photosensitivity and long wavelength UV absorption. Most interesting applications of materials produced from polysilanes with such important properties include semiconductors, non-linear optical materials, photoconductors and photoresistors.[38,40] Polysilanes with pendent metal complex segments were found useful in the area of new organic electroconductive materials.[41] Modification of the backbone of soluble polysilanes by interrupting the Si–Si sequence with a carbon atom yields pre-ceramic polymers that can be turned into usable silicon-carbide (SiC) ceramic materials through pyrolysis, chemical vapor deposition or chemical liquid deposition.[41,42]

Polysiloxanes

Polysiloxanes, commonly known as silicones, consist of a backbone of repeating siloxane (Si–O–Si) units (shown in figure 29), and are found in a broad range of commercial products.[34] Depending on the functionality of side-chains, polysiloxanes can be composed of either linear chains or cross-linked networks and can range from fluids to gels, to elastomers, to resins.[43]

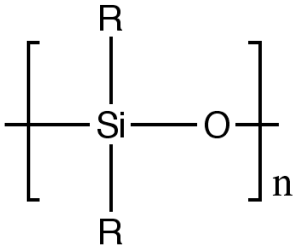

Figure 29 A general structure of the polysiloxane repeating unit.

Relatively high Si–O bond strengths and increased Si–O–Si bond angles result in thermal stability, extreme flexibility and high gas permeability of polysiloxanes. Various structures of the side-chain units of the polymer define its physical properties and potential applications, which include membranes, high-voltage insulators, water repellents, adhesives, lubricants and ceramic composites.[44] Biocompatibility, inertness and stability make silicones suitable for various medical applications, such as artificial organs and tissues, prostheses, contact lenses, cardiovascular devices, breast implants and devices preventing sexually transmitted infections.[38, 45]

One of the most interesting polysiloxane-based materials, which has a number of unique applications, is poly(dimethylsiloxane) (PDMS). It is extensively used in soft lithography to generate patterns with dimensions as small as nanometers.[46] In 2004, a revolutionary miniature hydrogen air proton exchange membrane from PDMS was designed and tested.[47]

Polysilazanes

Another important class of silicon-based polymers is polysilazanes, which contain a backbone of alternating Si and N, as seen in figure 30.

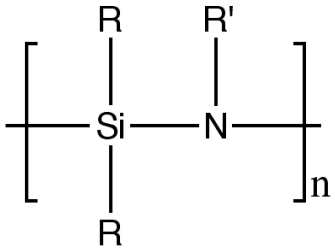

Figure 30 A general structure of the polysilazane repeating unit.

Polymers with linear chain structures possess relatively low molecular weights; however, species with high MW are obtainable by dehydrocoupling of oligomers. Polysilazanes are commonly used as precursors for silicon nitride ceramics, which are formed at high temperatures and provide heat- and impact resistant materials.[34]

1.2.3 Metal-containing polymers

Polymers of this type contain a variety of main group metals, transition metals or rare earth metals in the repeating unit and comprise a very unique part of material science. Numerous variations of the polymer structures with metals incorporated in the backbone directly or covalently bonded to the backbone result in novel and versatile materials, which advantageously combine common properties of polymers with electrical conductivity and the redox properties of metals. Two examples of such polymers are shown in figure 31.[34]

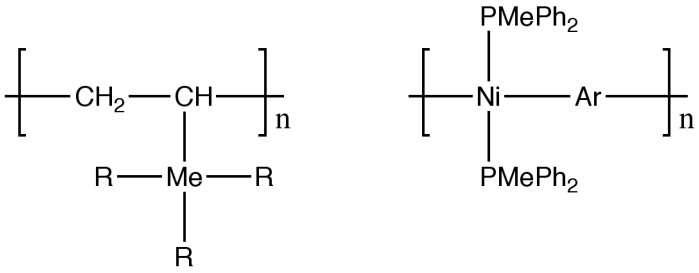

Figure 31 Two examples of organometallic polymers.

The most widely utilized polymers of this class are metallocenes, which are composed of repeating units of two η^5-bonded cyclopentadienyl ligands to a metal atom, as seen in figure 32.

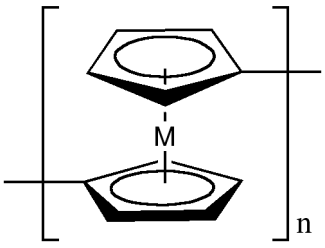

Figure 32 A general structure of a metallocene repeating unit.

In particular, polyferrocenes, which contain an iron atom in the repeating unit, exhibit very useful and unique properties, and hence are widely developed and characterized, with most work conducted by Alaa S. Abd-El-Aziz[48-59] and Ian Manners.[60-67] A general structure of a heteroannular polyferrocene is shown in figure 33.

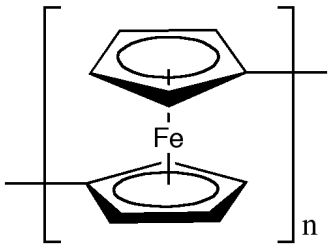

Figure 33 General structure of a heteroannular polyferrocene.

Several interesting examples include phosphazene polymers with ferrocene units in the side-chains shown in figure 33 A, and poly(ferrocenylsilane-*b*-polyphosphazene) block-copolymer[68] shown in figure 33 B.

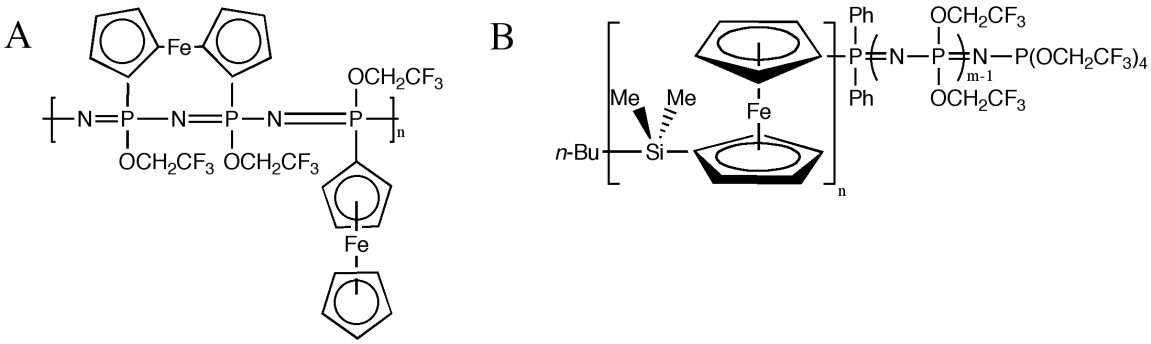

Figure 34 (A) Phosphazene polymer with ferrocene units in the side-chains; (B) poly(ferrocenylsilane-b-polyphosphazene) block-copolymer.

Various applications of polyferrocenes include semiconductors, adhesives, antioxidants and lubricants.[69]

1.2.4 Phosphorous-based polymers

Polyphosphazenes

Polyphosphazenes are a class of inorganic polymers that has drawn much research attention due to its extremely useful properties and wide range of applications. The pioneer of the polyphosphazene synthesis and research is Harry R. Allcock, who primarily developed and characterized this class of polymers during the 1960s.[70-84] Polyphosphazenes are composed of a backbone of alternating phosphorous and nitrogen atoms, with two side groups attached to each phosphorous atom, as depicted in figure 35.

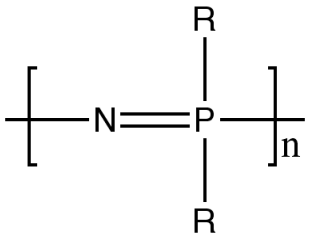

Figure 35 A general structure of a polyphosphazene repeating unit (R = NHR, NHAr, OR, OAr, Ar).

A polymer is commonly obtained via either thermal ring-opening polymerization (ROP) of hexachlorocyclotriphosphazene $(NPCl_3)_2$[34, 85-87] or by ambient living cationic polymerization of phosphoroanimine $Cl_3P{=}NSiMe_3$ in the presence of PCl_5[77-79] to produce a high molecular weight poly(dichlorophosphazene).

A ring-opening polymerization proceeds at 250°C – 300°C, as depicted schematically in figure 36.

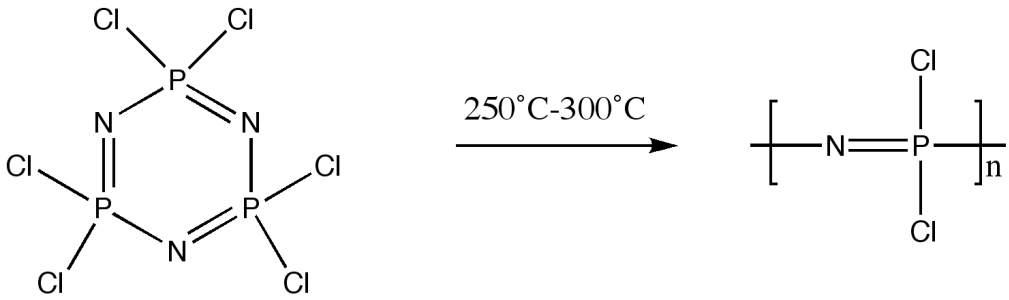

Figure 36 Synthesis of poly(dichlorophosphazene) via thermal ring-opening polymerization of hexachlorocyclotriphosphazene.

The ring-opening approach is a rather complicated and somewhat unpredictable process due to the lack of full understanding or control over polymerization.[88] The polymers are high molecular weight ($M_w > 2 \times 10^5$), but may differ largely in M_w, distribution and macromolecular arrangements even when prepared at similar conditions. This results in very high polydispersity indices ($M_w/M_n > 10$). Another difficulty associated with thermal ring-opening polymerization, which is believed to proceed by cationic chain mechanism, is a formation of 'inorganic rubbers' due to cross-linking. This mechanism is still uncertain; however, it has been suggested that the chain propagation may occur via electrophilic attack on the nitrogen of a cyclic molecule and reaction of a propagating terminal unit with another chain would then result in formation of branches, as seen in figure 37. Given these processes are competitive, the cross-linking would only become considerable at later stages of polymerization when most of the cyclic trimer species are depleted and propagation is retarded.[89]

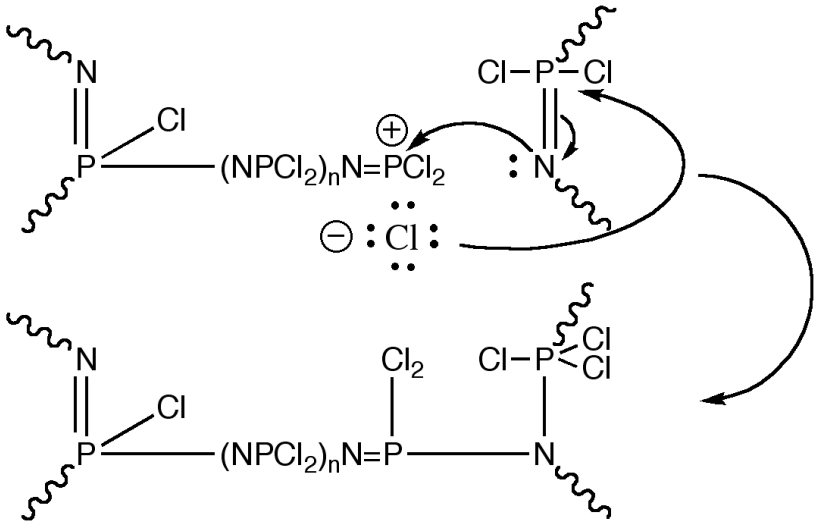

Figure 37 Proposed mechanism of chain propagation and cross-linking during thermal ring-opening polymerization of hexachlorocyclotriphosphazene.

Formation of the cross-linked polymer matrix can also occur if the hydrolytically unstable poly(dichlorophosphazene) is exposed to trace moisture, in which it undergoes rapid hydrolysis of P–Cl segments, and branching between polymer chains then occurs via formation of P–O–P bonds (shown in figure 38).[89]

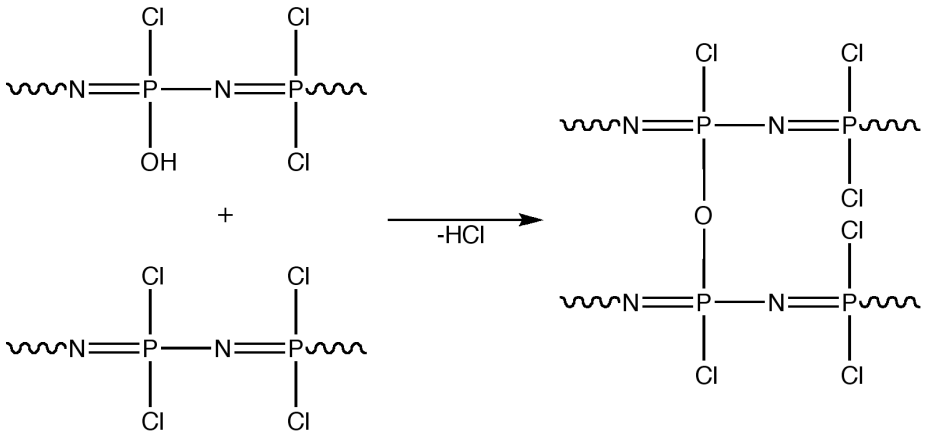

Figure 38 Cross-linking of poly(dichlorophosphazene) via P–O–P bonds forming upon hydrolysis.

Cross-linked species are highly insoluble in common organic media and therefore are unsuitable for any further side chain substitutions in solution.

Another approach to the synthesis of poly(dichlorophosphazene) is via the polymerization of phosphoroanimine in the presence of trace initiator. The monomer is prepared by a two-step one-pot synthesis at ambient conditions (depicted in figure 39), which helps minimize energy consumption that is usually associated with the thermal polymerization, and hence is more economically efficient.[90] Ultimately, this method can be optimized to suit syntheses on the industrial scales.

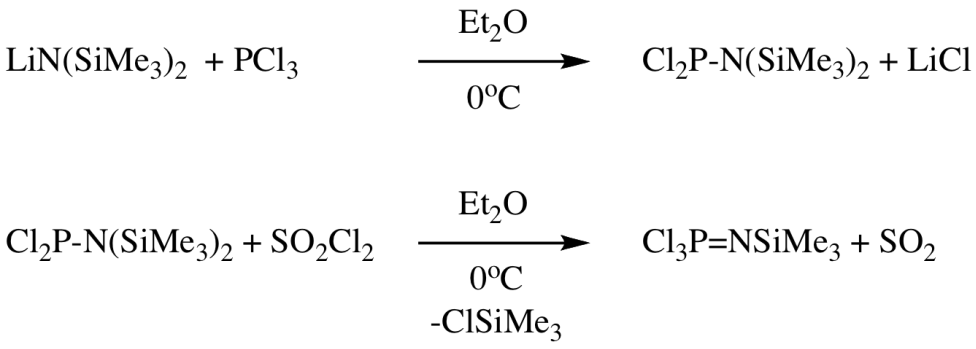

Figure 39 A synthesis of phosphoroanimine at mild conditions.

Trace quantities of Lewis acid, PCl_5, then trigger living cationic polymerization to produce poly(dichlorophosphazene).[91] Properties and molecular weight of the polymer are influenced by reaction parameters, i.e. solvent, concentration, temperature and monomer to initiator ratio, yielding species with M_w about 10^5 and narrow polydispersity ($M_w/M_n < 2$).

The polymeric precursor poly(dichlorophosphazene) can be reacted with bi- or multifunctional substituents[86, 92] through the direct nucleophilic substitution of chlorine

atoms in side chains, yielding over 700 derivatives known to date.[86, 93] This extremely large variety of side chains provides materials for applications such as electric insulators and conductors, non-linear optics, lubricants, membranes, flame-resistant and flame-retardant films and coatings, solid polymer electrolytes, photosensitive materials, artificial bone grafts, soft tissue prostheses, chemotherapeutic models, drug delivery systems, etc.[84, 92, 94-121] A general schematic of nucleophilic substitution are shown in figure 40.

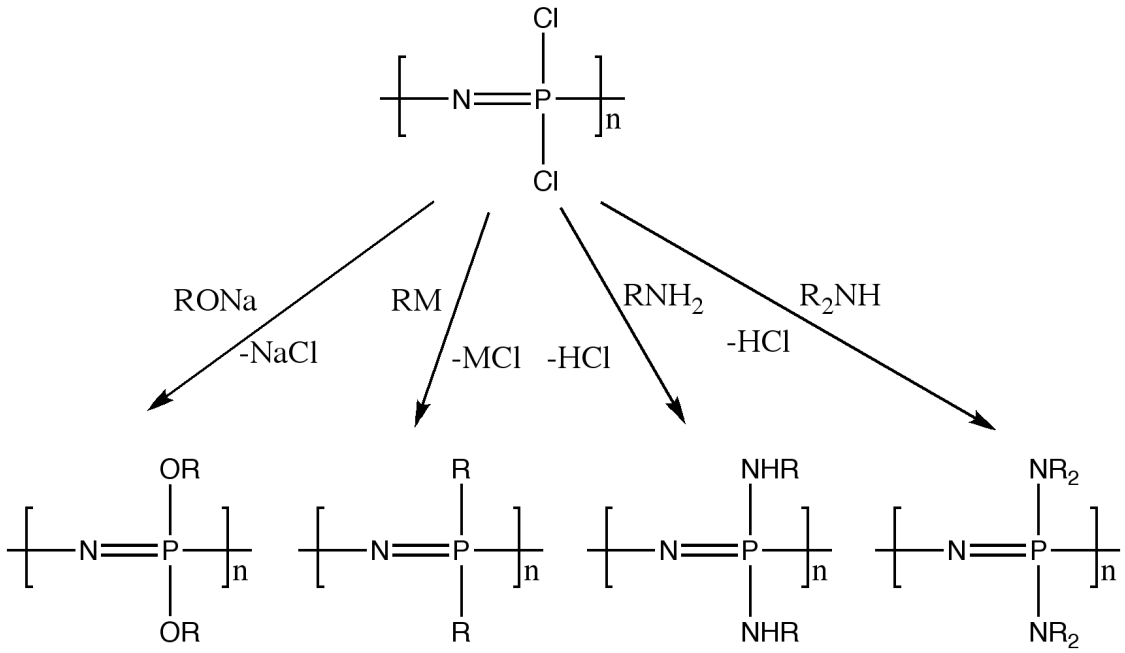

Figure 40 Polyphosphazene derivatives obtained via nucleophilic substitution of side-chains in poly(dichlorophosphazene).

Polyphosphazenes have been extensively characterized in the last 30 years using X-ray diffraction, dilatometry, differential scanning calorimetry (DSC), thermal gravimetric analysis (TGA), optical microscopy, calorimetric analysis, dynamic mechanical, Raman and NMR spectroscopy,[122-124] to provide detailed insight on the

electronic structure, bond lengths, chain orientation, mechanical properties and thermal transitions.

Theoretical calculations suggest the 'island model' of the electronic structure of polyphosphazenes,[124] where suitable *3d* phosphorous orbitals are hybridized with *p* orbitals of the nitrogen to form three-centered π-bond islands interrupted at phosphorous. Bonding parameters reported for poly(dichlorophosphazene) indicate bond lengths of approximately 1.6 Å (P–N) and 2.0 Å (P–Cl).[124] Bond angles are approximately 132° (P–N–P), 114° (N–P–N) and 105° (Cl–P–Cl). Studies confirm *cis,trans*-planar conformation as a model for polyphosphazene backbone,[125] with the chain repeating distance about 4.8-4.9 Å. The arbitrary direction of the polymer chain is determined by the ligand bonds from phosphorous, which are inclined with respect to the backbone, as seen in figure 41.

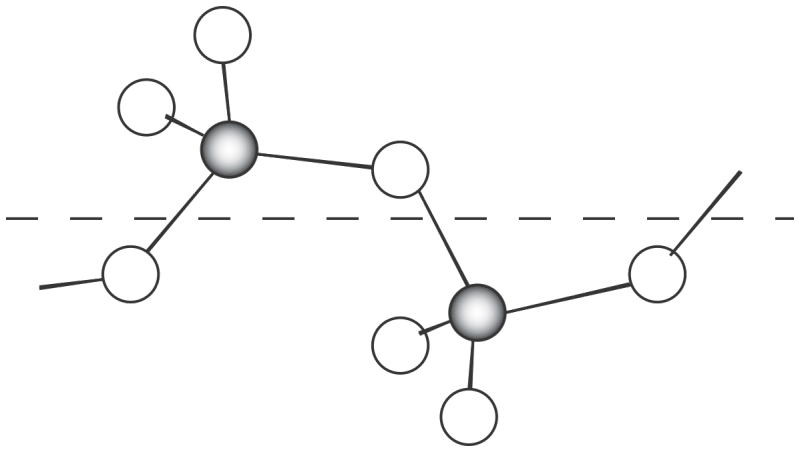

Figure 41 A fragment of polyphosphazene backbone in cis,trans-planar conformation with respect to the chain axis.

The most commonly utilized and studied polyphosphazene derivative is poly[*bis*(trifluoroethoxy)phosphazene] (PBFP).[126] It is easily obtained through

nucleophilic substitution of chlorines in poly(dichlorophosphazene) side-chains upon reaction with sodium trifluoroethoxide.

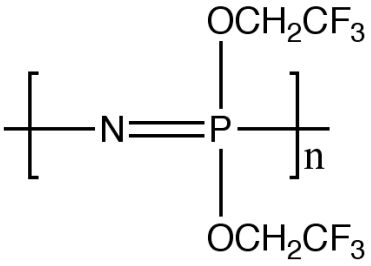

Figure 42 Structure of the poly[*bis*(trifluoroethoxy)phosphazene] repeating unit.

PBFP is a high molecular weight polymer ($M_w > 10^4$), where its physical properties are largely dependent on the preparation and normally can range from white fibrous to opaque flexible material that can form films and fibers.[127] Solution parameters of PBFP suggest a high degree of flexibility and coiling of the polymer backbone with a *cis,trans*-planar conformation. The polymer is extremely hydrophobic and chemically stable, and has been shown to be inert to alcohols, pyridine and concentrated NaOH solutions[126]. Studies using TGA suggest high thermal stability of PBFP, which volatilizes at approximately 500°C. Tests on the flame resistance of the polymer show a Limiting Oxygen Index of 48.0, resulting in high resistance to combustion and 'clean' burning leaving no heavy residue. The afore-mentioned unique properties make PBFP a highly versatile material that can be used for such important high-performance applications as membranes for fuel cell technologies[128] and biomedical materials.[129]

PBFP belongs to the semi-crystalline class of polymers and hence contains both regions with rigid and ordered chains (crystalline), and randomly coiled and entangled chains (amorphous). Materials of this type can be characterized by the percent

crystallinity and the crystallites size and structure, and combine both strength and flexibility. The boundaries between two types of chain arrangement are insignificant, and hence these interfacial regions are often neglected; this is illustrated schematically in figure 43.

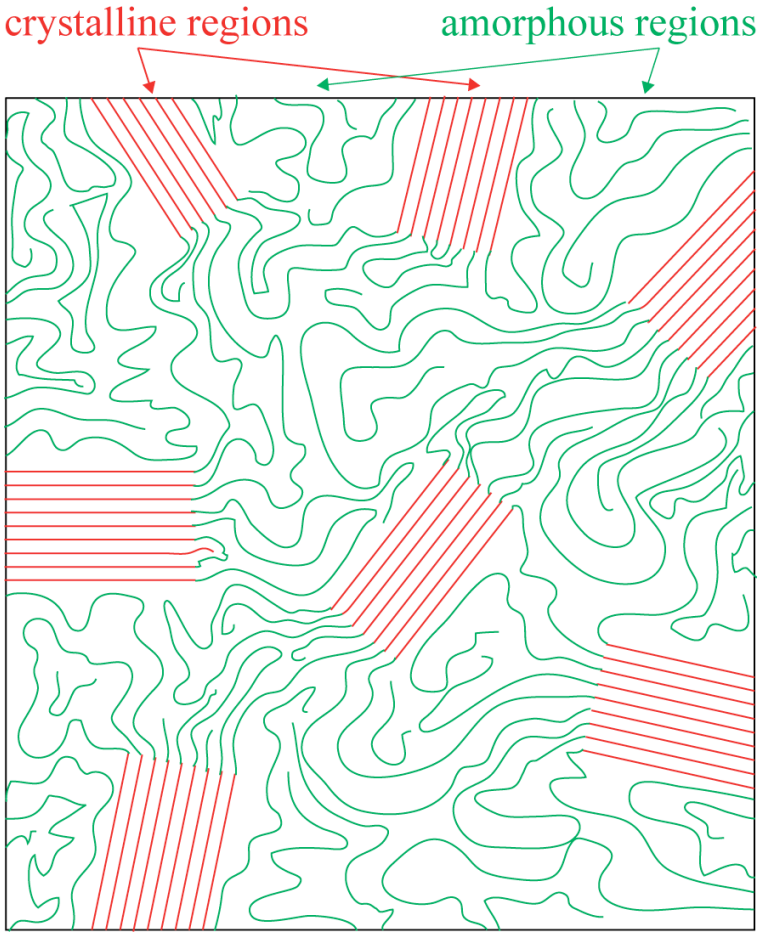

Figure 43 Domain structure of semi-crystalline materials

Previous investigations[130-153] indicate that PBFP exhibits complex thermal and morphological behavior, identifying three transition temperatures that vary largely depending on the thermal history, molecular weight and crystallinity of the polymer. The

temperatures reported in the literature for the glass transition, thermotropic transition and melting point, are $T_g \approx$ -66°C, $T(1)$ = 66°C – 90°C and $T_m \approx$ 240°C, respectively.

When cast from solvent, PBFP tends to form large spherulites, which are readily observed in optical micrographs, and are composed of lamellae with either mostly 3D chain-folded β-monoclinic, 3D chain-folded α-orthorhombic crystal forms, or a mixture of the two, depending on the initial crystallinity and polymorphism. Upon heating through $T(1)$, the spherulites are unaffected; however, PBFP transforms to a 2D chain-extended pseudohexagonal mesophase. At temperatures above T_m the spherulitic structures are destroyed, and the polymer melt exhibits the isotropic phase with zero birefringence. Recrystallization from the melt reverts PBFP to the 2D pseudohexagonal mesophase, where needle-like batonnet morphology is formed instead of the spherulitic structure. Cooling below $T(1)$ leads to formation of a chain-extended 3D γ–orthorhombic structure of a higher crystallinity, rather than the chain-folded form. This transition upon initial passage through $T(1)$ is irreversible, and the degree of phase transformation is characterized by the molecular weight of the polymer species as well as the rate of heating and cooling. Upon additional thermal treatment with temperatures cycled from ambient to above T_m, PBFP undergoes transition from the chain-extended crystallite form, through the 2D pseudohexagonal mesophase, to the isotropic melt, and back to the rod-like 3D γ–orthorhombic structure below $T(1)$. Such repeated heat treatment increases the overall crystallinity of the polymer, as indicated by higher $T(1)$ values at each cycle. Effects of thermal treatment on PBFP are shown in the phase transition diagram in figure 44.

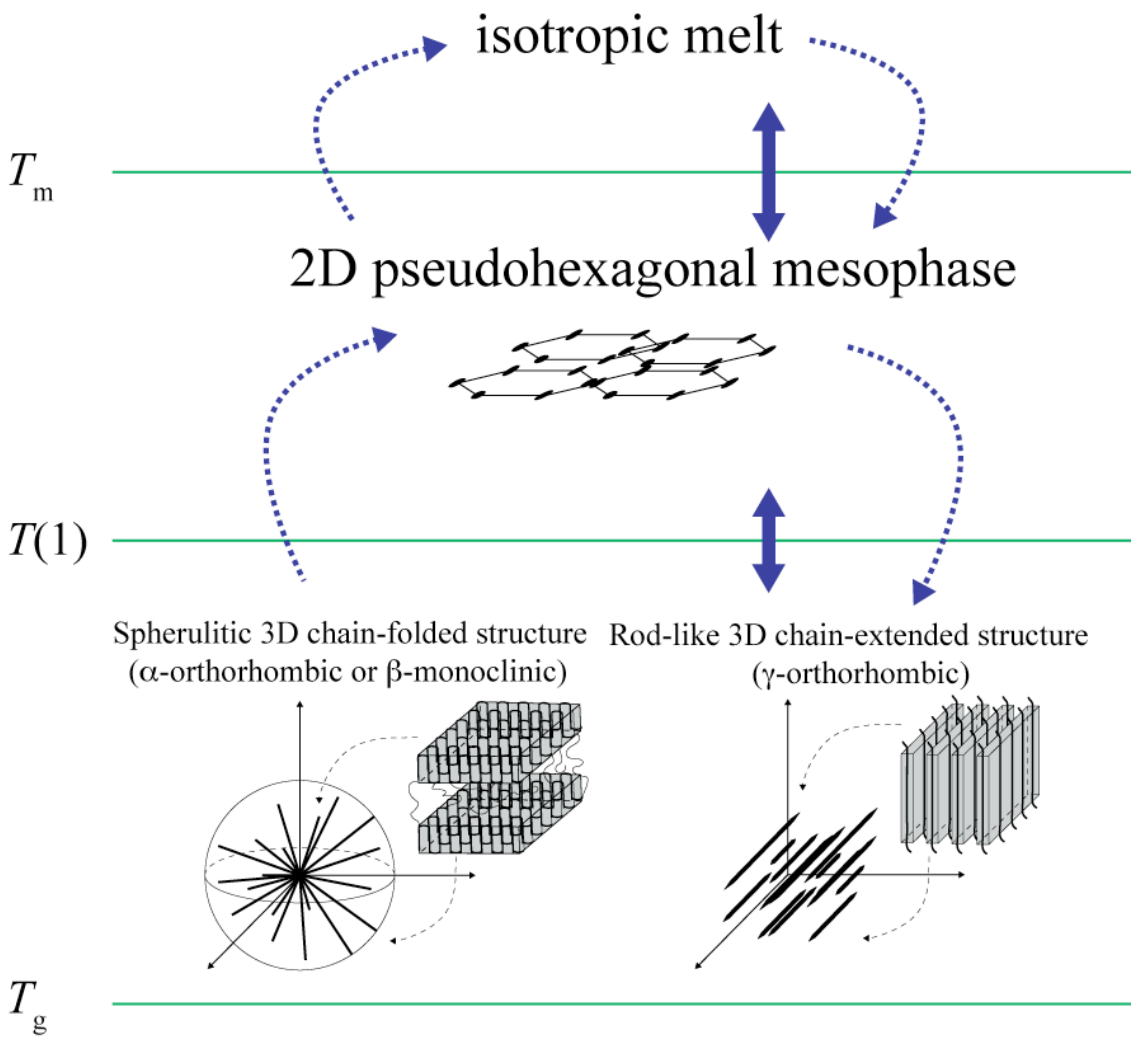

Figure 44 Phase transition diagram for solvent-cast PBFP. Dashed lines indicate transition pathway upon initial thermal treatment; bold arrows indicate reversible transitions upon cycled heating.

In conclusion, it has been shown how various preparation methods and thermal history affect the crystallinity and morphology of PBFP, which in turn define final properties of the product. One can appreciate the importance of accurate and extensive characterization methods that would allow for fine 'tuning' of properties of PBFP to suit specific applications.

Phosphorous-oxygen based polymers

A variety of oligomers and polymers containing oxygen and phosphorous atoms is found in living cells and play an important part in biochemical processes. One example is a high-molecular weight polyphosphate shown in figure 45.

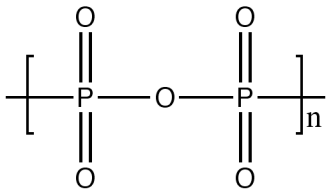

Figure 45 Structure of the polyphosphate repeating unit.

Polyphosphates occur naturally in living organisms, where they regulate metabolic processes, cellular development and proliferation, and participate in transport mechanisms.

1.3 Solid-state NMR of polymers

1.3.1 Overview

One of the primary focuses of material science today is the development of novel polymers and modification of existing ones, to ensure they meet the ever-increasing requirements for today's high-performance applications. Correspondingly, in order to understand how to finely tailor the macroscopic properties of a polymer one must first fully understand how they relate to its structural features on the atomic scale. A variety of techniques for characterizing solid materials exist today, each employing different principles of operation and hence the type of properties they can probe. X-ray diffraction, DSC, TGA, and GPC, are most commonly applied to studying polymers. In the case of semicrystalline polymers X-ray is limited to providing unit cell dimensions of only the crystalline phases and cannot give insight into the disordered phases. DSC gives only thermodynamic transition temperatures. In a similar manner, most techniques do not provide the most important and desired structural, and dynamic information at the atomic level. On the other hand, MAS NMR is not subject to these limitations and has proven to be an extremely robust and versatile tool for probing a broad range of parameters that are common to polymers, as will be discussed in this chapter. Interesting and notable applications of solid-state NMR on various organic, inorganic and biological polymer systems will be illustrated with chosen examples.

Polymers are large and complex systems that are comprised of linear, branched and cross-linked macromolecular chains of variable length, which differ in backbone, and

side-chain composition. They can also have variations in the end-chain and defect-unit structures. These chains also have a degree of variation in conformations along their main chain and in the way these chains pack together. These polymer environments are further characterized by different dynamics. End-chain units may undergo a rapid rotation about the bond axis, while motions of units in the backbone and side-chains at the cross-linking sites are restricted. In addition, polymers with complex morphologies are composed of local macromolecular regions containing chains that are tightly packed forming crystalline lamellae with various crystal types and dimensions, and chains that are randomly coiled and entangled to give rise to amorphous domains of different mobilities.

The high degree of variation in structure, morphology and dynamics between various regions of the polymer are reflected in complexity of the signals observed in the corresponding NMR spectrum. Chemical shifts, linewidths, intensities, and line shape of each signal are all influenced by these factors, which are a direct result of how they affect relaxation mechanisms, CSA and dipolar interactions experienced by spins. For example, in the crystalline phase of a polymer the CSA and the dipolar coupling interactions are prominent due to the restricted mobility and reduced internuclear distances arising from the tight packing. This gives rise to homogenous and inhomogeneous broadening of the lines and gives them a Gaussian shape. In contrast, these line-broadening mechanisms are reduced in the more mobile amorphous domains, which correspondingly give narrower and mostly Lorentzian lines. The rigidity of the crystalline domain also causes more rapid T_1, T_2 and $T_{1\rho}$ relaxation processes compared to the amorphous regions. These differences between amorphous and crystalline signals are widely exploited by

various selective 1D and 2D MAS NMR techniques used to measure spin diffusion, relaxation, dipolar interactions *etc*, that give valuable insights into polymer morphology.

1.3.2 Molecular structures and connectivities in polymers

Signals in the NMR spectra of polymers consist of the superimposition of peaks from numerous diverse macromolecular units. In principle, provided that sufficient resolution can be achieved, allowing accurate determination of their chemical shifts, widths, intensities, composition (via deconvolution analysis), and connectivity leads to the elucidation of their 'average' local atomic structures of the recurring units. Furthermore, the signal from end-chain groups can be compared to that corresponding to the main chain to determine its length in terms of the number of repeating units and subsequently estimate the average molecular weight. Similar comparison can be made to determine the degree of cross-linking in the polymer if the characteristic signal for a cross-link can be identified. Variable temperature experiments exhibit changes in the corresponding spectra as the result of phase transitions in the polymer. This approach not only indicates that a phase transition is occurring but also identifies the process; therefore, MAS NMR is invaluable in the study of polymer morphology and thermochemistry.

Detailed information about the molecular structure, cross-linking and backbone and side-chain geometry of polymers can be determined from the through-space and through-bond connectivities and internuclear distances obtained via two-dimensional MAS NMR experiments. A variety of such 2D solid-state NMR techniques exist today

and are routinely applied in the studies of materials[154-156] from which two, INADEQUATE and RFDR, were explored in detail in sections 1.1.13 and 1.1.14, respectively. The most recent examples of applications of 2D INADEQUATE MAS NMR experiments include studies of conformations in poly(ethylene oxide)[157] and the determination of the P–O–P connectivities in crystalline and amorphous phosphates [158, 159]. The RFDR experiment was used to determine the proximities between crystalline and amorphous domains in an alpha-poly(vinylidenefluoride).[160] Another widely used sequence that is also worth mentioning is Heteronuclear Correlation (HETCOR) spectroscopy. HETCOR correlates the signals from two different types of directly coupled nuclei and has been employed to determine through-space heteronuclear connectivities in polymers.[161-173] Several other two-dimensional solid-state NMR experiments have recently been developed that can provide information about connectivities and structures of materials, such as: Heteronuclear Multiple-Bond Connectivity (HMBC),[174] Through-bond Heteronuclear Single-quantum Correlation (MAS-J-HSQC)[175] and Through-bond Heteronuclear Multiple-quantum Correlation (MAS-J-HMQC); however at this time they have not yet seen extensive application to the study of polymer systems.

Finally, MAS NMR spectroscopy of crystalline polymers allows for the study of the electronic structure and conformations of polymer, via the observation of the chemical shielding anisotropy of its various constituent nuclei. In principle, tensor components can be extracted from the spectra and compared with predictions from MO calculation methods along with X-ray diffraction information, to determine a structural model of the system.[176]

1.3.3 Molecular dynamics of polymers

Solid-state NMR is a very powerful tool for probing the chain dynamics within polymers, in both amorphous and crystalline regions.[177] Dynamics can have a profound impact on important properties of the material, such as flexibility, elasticity, permeability, etc. Unlike solutions where rapid molecular motions have mostly averaged out the orientationally dependent spectral parameters, in solids relaxation, linewidths and dipolar interactions, which depend very strongly on the molecular motion, can provide detailed insight into chain dynamics. Most common techniques used to elucidate segmental motions in polymers include measurements of T_1, T_2 and $T_{1\rho}$ relaxation, cross-polarization dynamics and advanced two-dimensional experiments, all of which were successfully applied to studies of polymers as will be illustrated with recent examples.

Recall that the spin magnetization experiences relaxation processes due to the constant perturbations from local time-dependent magnetic fields, which are caused by CSA, spin-spin couplings and other orientationally-dependent interactions which are modulated by nearby molecular motion. The motion of these fields, characterized by the correlation time, τ_c, must be near the Larmor frequency of the nucleus in order for relaxation to occur: $\tau_c \approx 1 / \omega_0 \approx 10^6 - 10^9$ Hz. Since dynamics in solids is several orders of magnitude slower than in liquids, it is desirable to enable detection of motions at slower frequencies, and hence a common approach in MAS NMR is to measure the $T_{1\rho}$, which is determined by the strength of the spin-lock field, which is several kHz ($T_{1\rho} \approx 1 / \omega_1 \approx 1$ ms to 10 μs), rather than the magnetic field strength, which is 100's of MHz. The closer the $1/\tau_c$ is to the spin locking frequency of the nucleus, the faster the relaxation rate

will be. In fact, the rate is maximum when the two are equal. Correlation times are temperature dependent, hence obeying the Arrhenius form. Therefore, one can measure relaxation as a function of temperature and extract the rate of motion from the maximum in the plot of $1 / T_x$ vs T where T_x is T_1, T_2 or $T_{1\rho}$. This approach is very widely utilized for elucidating quantitative information about dynamics at the specific sites of the bulk organic, inorganic and biological polymers.[178-193]

Another approach to investigating the dynamics in solids under MAS conditions is employed in two-dimensional Exchange Spectroscopy (EXSY)[177] and Centerband-Only Detection of Exchange (CODEX)[1], in which the mechanism of the longitudinal magnetization exchange between nuclei is established through chemical exchange rather than polarization exchange. This allows for observing molecular motions occurring at much lower frequencies (10^{-1} – 10^4 Hz), which is particularly useful for investigating very slow dynamics of polymers near glass-transition temperatures. The most recent examples include 2D EXSY NMR studies of the conformational exchange dynamics in poly(ethylene glycol)-substituted cyclodextrins[194] and application of CODEX experiments to elucidate slow chain motions in [Ring-fluoro]polycarbonate,[195] isotactic-poly(4-methyl-1-pentene) crystallites[196] and poly(alkyl methacrylate).[197]

1.3.4 Domains and phases of polymers

In order to fully understand the macroscopic properties of polymers, it is necessary to obtain detailed insight about their various crystalline, amorphous and interfacial environments such as their sizes, morphologies and phase structure. These aspects of the domains would be more easily studied if it were possible to investigate them separately. Domain selective methods have been developed for MAS NMR for just that purpose, and have proven to be very effective in probing those properties.[176] Efficient domain selection is made possible through filtering the signals on the basis of differences in relaxation rates, dipolar interactions and CSA's. This makes it possible to perform spin diffusion measurements, which are used to determine the domain sizes.

Relaxation-based sequences, widely used to study solid polymers, exploit differences in T_1, T_2 and $T_{1\rho}$, which are normally significantly shorter in ordered crystalline environments; therefore the pulse sequence can be setup so that only the signal from amorphous domains remain behind.[198] Differences in strengths of dipolar interactions can be used to selectively remove domains with strong dipolar interactions[199] this again would give rise to sequences that are selective for mobile amorphous domains. Sequences that utilized this approach are pulse saturation transfer,[200] dipolar filter,[201] dipolar dephasing,[202-206] cross-polarization-depolarization[207] and Discrimination Induced by Variable Amplitude Minipulses (DIVAM)[208-212] MAS NMR experiments. Furthermore, chemical shift anisotropy has also proven useful for discriminating between different domains in polymers.[213, 214] Amongst these techniques DIVAM is of particular interest due to its effectiveness and versatility, and hence it will be discussed in detail.

The CP DIVAM filter sequence can be tuned to select desired signals on the basis of spin-spin relaxation rates. This technique is very versatile in that it allows for observing the signals from either domain of interest (i.e. crystalline or amorphous), while suppressing signals from other domains, within one experiment. A filter is applied to an abundant nucleus, **I**, followed by the subsequent detection of nucleus **S**, which leads to the magnetization transfer from the chosen regions only. A pulse sequence of the MAS NMR DIVAM experiment is shown in figure 46.

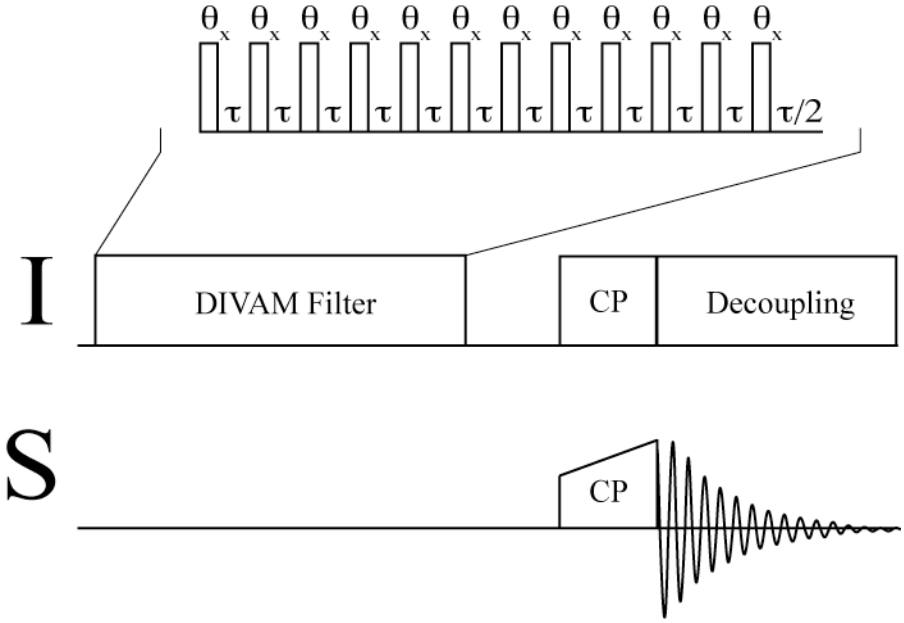

Figure 46 Pulse sequence of the MAS NMR DIVAM experiment.

The pulse sequence is composed of a train of 12 θ_x pulses spaced by the inter-pulse delay τ, where an excitation angle θ is varied from 0º to 90º, in small increments, by changing the strength of the RF field, whilst retaining the constant pulse duration. Each mini-pulse

rotates the longitudinal magnetization from both crystalline and amorphous domains, to the transverse plane by an angle θ. During an appropriate delay τ differences in T_2 cause the separation of the two components of magnetization, where the faster-relaxing component from the crystalline region will have a smaller angle with respect to the *z* axis, than the amorphous one. Repetitive θ – τ – θ cycles result in the accumulation of a phase difference in the *xy*-plane, caused when the transverse magnetization from one domain is fully relaxed back to the *z* axis while the other component moves very little, as seen in figure 47. As the corresponding intensity of the signals in the spectrum nutate as a function of the excitation angle, differences in the spin-spin relaxation rate between rigid and mobile components will therefore alter the rate of nutation of each component causing them to invert, or zero-cross, at slightly different excitation angles. As a result, by setting the appropriate excitation angle and interpulse delay one can set the sequence to select for either domain of interest, while the other is suppressed.

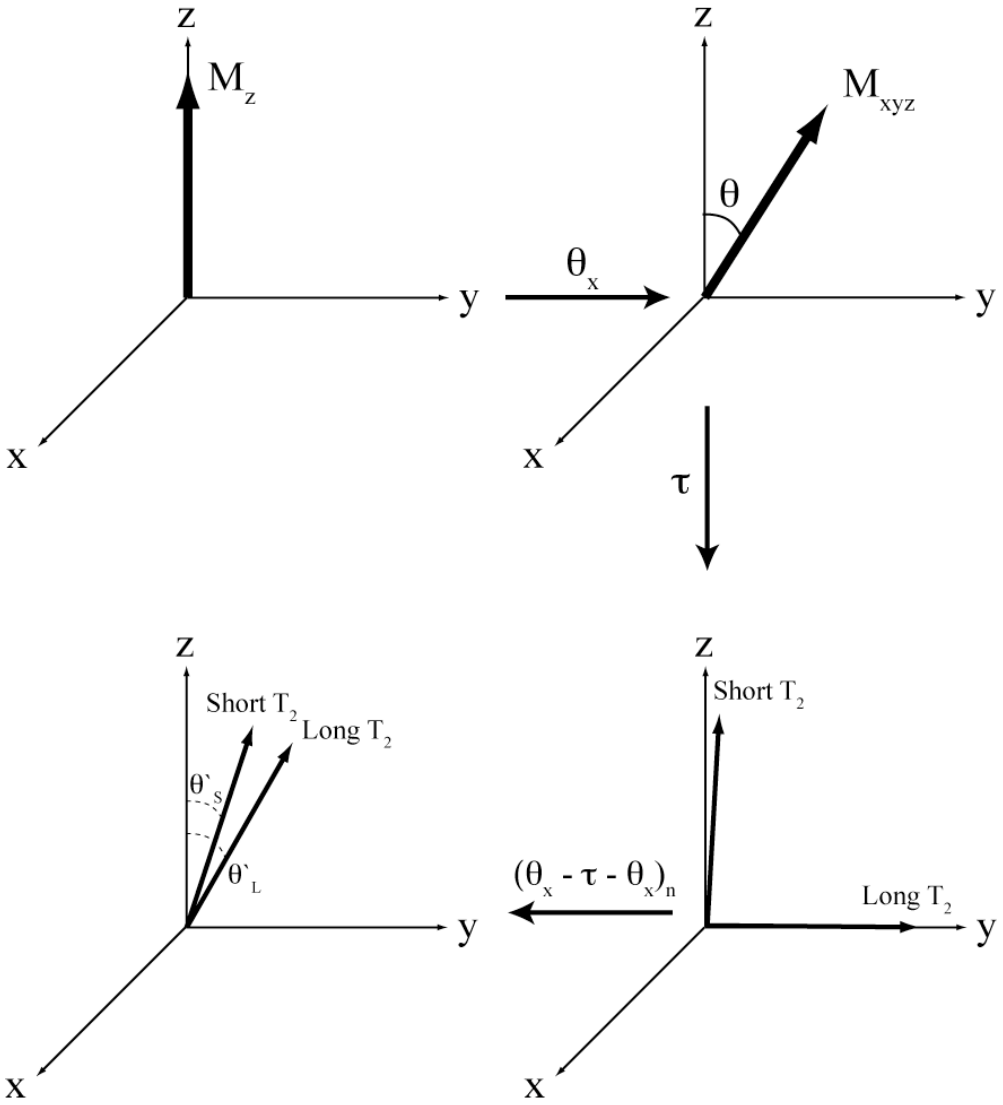

Figure 47 Structure of the MAS NMR DIVAM domain selection filter.

Spin magnetization experiences diffusion-like processes throughout a volume of material, which are translated via the dipolar interactions. This phenomenon known as spin diffusion, is a function of the molecular geometry and the magnitude of the dipolar coupling, and hence reflects structural and dynamic features of the different domains of the bulk material. By selectively exciting a particular domain of polymer and subsequently monitoring the change over time in the signal for each domain one can

determine the rate of spin-diffusion and from this estimate the average distance over which the diffusion process takes place, indicating the size of the domains. Since this process is influences by the heterogeneity of polymer environments, spin diffusion measurements make it possible to obtain unique insights into: polymer morphology, surface and interfacial properties, domain structures and sizes, and miscibility of polymer and polymer blends.[215-225] Two of the most commonly used techniques based on the observation of spin diffusion include the Goldman-Shen-based experiments[226] and 2D Wide-line separation (WISE) spectroscopy.[144, 227-229]

In conclusion, the aforementioned techniques make MAS NMR give rise to information that is not readily available via other methods and hence it is an invaluable and routine tool for investigating the domains and morphologies of inorganic, organic and biological polymer materials.[165, 168, 179, 182, 189, 230-253, 144-146, 254-286, 134, 142, 146, 181, 182, 198, 233, 251, 259, 267, 287-301]

1.3.5 Solid-state NMR of phosphazene polymers

As previously discussed, polyphosphazenes are an extremely important class of polymers, which see a very broad range of commercial applications due to their unique properties. However, conventional methods used for characterization of the polymers are not always able to provide comprehensive and accurate information about atomic structures, phases, morphologies and spatial parameters on the microscopic level, which can be correlated to the corresponding macroscopic properties of phosphazene polymers and allow for their fine tailoring to meet particular needs. On the other hand, MAS NMR

has been proven an extremely powerful tool for elucidating various information of polymers. Despite apparent advantages offered by this spectroscopic technique, polyphosphazenes so far have seen somewhat limited attention from MAS NMR, even though very interesting information can be obtained using various NMR techniques, as will be demonstrated with examples that follow.

The first notable application of MAS NMR was reported in 1983 by Pratt Ackerman where ^{31}P solid-state NMR was used to observe chemical shift anisotropies and molecular motions in several phosphazene elastomers.[302] Five years later, in 1988, Tanaka *et al* proposed multinuclear MAS NMR for investigating phase transitions in a representative poly[*bis*(4-ethylphenoxy)phosphazene],[303] which was followed by ^{31}P experiments at variable temperatures, where two signals observed in the spectra from crystalline and amorphous domains exhibited temperature dependence, from which the thermotropic transition temperature $T(1)$ of poly[*bis*(trifluoroethoxy)phosphazene] was estimated.[304] A few years later several independent MAS NMR studies were conducted on a variety of phosphazene polymers using the combination of variable temperature, relaxation and spin diffusion methods. The activation parameters for the phenoxy group motion about the P–O bond, as well as the existence of the interfacial regions, were determined for semicrystalline poly[*bis*(phenoxy)phosphazene].[145] The morphology, molecular dynamics and lamellar thickness were probed for poly[*bis*(3-methylphenoxy)phosphazene].[146] Solid-state NMR was combined with other methods to provide interesting insight about properties of the mesophase as well as the phase transitions in halogenated phenoxyphosphazenes, which were correlated to the nature of side-chain units.[305] Variable-temperature ^{31}P and ^{13}C MAS NMR experiments were

applied to a series of polyphosphazenes with non-linear optical (NLO) groups, which suggested that increasing the spacer group between the backbone and the NLO units lowers the temperature regime of the chromophore motional quenching.[306] Simonutti *et al.* investigated morphology and side-chain mobilities in poly(ethylphosphazene) using variable-temperature ^{1}H – ^{13}C – ^{14}N triple-resonance MAS NMR experiments.[152, 153] Relaxation rate measurements and variable temperature NMR were used to probe dynamics of the swelling and solvent permeation processes.[307] DIVAM domain selection filter and high-resolution ^{1}H, ^{19}F, ^{31}P and ^{13}C fast-MAS NMR experiments were performed on poly[*bis*(trifluoroethoxy)phosphazene],[15, 308] where significant improvements in spectral resolution allowed for the preliminary assignment of signals from various crystalline, mesophase and amorphous regions of the polymer. Finally, the most recent account features solid-state NMR studies of the backbone dynamics in the deuterated poly[*bis*(methoxy)phosphazene] near the glass transition temperature T_g using ^{2}H NMR.[309]

In conclusion, it was shown that various MAS NMR techniques can provide a broad array of interesting information about the properties of polyphosphazenes; however, these methods are still frequently neglected. Results of the systematic approach to investigating the representative polyphosphazene systems using MAS NMR will be discussed in chapter 3.

2 MATERIALS AND METHODS

2.1 NMR experimental parameters

2.1.1 General parameters

NMR spectra were obtained using a Varian INOVA 500 spectrometer operating at 499.84 MHz for ^{1}H, 125.68 MHz for ^{13}C, 470.332 MHz for ^{19}F and 202.34 MHz for ^{31}P. ^{19}F NMR spectra were referenced to external $CFCl_3$ (δ 0.0), ^{1}H NMR spectra were referenced to external TMS (δ 0.0), ^{31}P NMR spectra were referenced to 85% H_3PO_4 (δ 0.0) and ^{13}C NMR spectra were referenced to adamantane by setting the CH_2 peak to δ 38.6. For all experiments either 2.5 or 4 mm Vespel rotors were used, which were equipped with Kel-F turbine caps, inserts and seal screws.

2.1.2 ^{1}H, ^{19}F, ^{31}P and ^{13}C one-dimensional MAS NMR at ambient temperature

Direct polarization and cross-polarization experiments at ambient temperature were performed using a VARIAN T3 4-channel HFXY probe with a 2.5 mm outer rotor diameter and a MAS rate of 25 kHz. All NMR spectra were obtained using a 100 kHz sweep width with 8192 points in the FID, and were zero-filled to 64,000 points, unless stated otherwise. For all direct polarization experiments, a one-pulse sequence was used, where 90º excitation pulse lengths for ^{1}H, ^{19}F, ^{31}P and ^{13}C channels were set to 3.5, 3.25, 4.25 and 4 μs, and relaxation delays to 4, 4, 4, and 8 s, respectively. $^{31}P\{^{1}H,^{19}F\}$, $^{1}H\{^{19}F\}$ and $^{19}F\{^{1}H\}$ NMR spectra of all samples were acquired using TPPM decoupling,[12] where the powers for the ^{1}H and ^{19}F decoupled channels were set to 35.7

and 38.5 kHz, as determined by peak-to-peak voltage. High-resolution $^{13}C\{^{1}H,^{19}F\}$ NMR spectra were obtained using high-power XY-16 rotor-synchronized simultaneous double-decoupling[14] with windowed acquisition. Curve and width for the $^{1}H \rightarrow {}^{13}C$ and $^{19}F \rightarrow {}^{13}C$ ramped cross-polarization experiments were set to 50 and 10000, respectively. Optimal Hartmann-Hahn matching conditions were achieved by setting contact times to 2 ms and cross-polarization powers to 48.2 kHz for the proton channel and 50.9 kHz for the fluorine channel. ^{1}H and ^{19}F direct DIVAM nutation experiments were performed using 50 excitation pulses with increments of 1.83 degrees.

2.1.3 Variable-temperature ^{31}P MAS NMR

Variable-temperature studies were conducted using a VARIAN T3 4-channel HFXY probe with 4 mm outer rotor diameter, and a MAS rate of 10 kHz. $^{31}P\{^{1}H,^{19}F\}$ NMR VT studies of SC were performed at a MAS rate of 10 kHz with temperatures ranging from RT to 150°C, in 10 degree increments. Spin-lock times in the $^{31}P\{^{1}H,^{19}F\}$ $T_{1\rho}$ experiment were set to 1, 5, 10, 15, 25, 35, 50, 65 and 90 ms. The excitation pulse length for ^{31}P was set to 4.75 ms, with a 6 s recycle delay. ^{1}H and ^{19}F were decoupled using a TPPM sequence, with respective powers set to 31.3 and 33.3 kHz.

2.1.4 Two-dimensional ^{31}P MAS NMR

The homonuclear ^{31}P – ^{31}P refocused INADEQUATE experiment was set up according to the pulse sequence diagram discussed in chapter 1.1.13, where $\pi/2$ and π pulse lengths were set to 4.75 and 9.5 ms, respectively. The inter-pulse delay τ was determined as $1/(4 \times J_{PP}) = 1/(4 \times 60\ \text{Hz}) = 4.16$ ms, where J_{PP} was obtained from the splitting pattern in the ^{31}P{^{1}H} NMR ($CDCl_3$) of the phenoxy-substituted chlorinated phosphonitrillic trimer. The number of points in the FID were set to 8192 in t_2 and 180 in t_1. The relaxation delay was set to 1 s. All NMR spectra were obtained under ambient conditions using 4 mm Vespel rotors and at a MAS rate of 8 kHz.

The phosphorous homonuclear RFDR experiments for all samples under ambient conditions were performed at a MAS rate of 8 kHz. Lengths of $\pi/2$ and π pulse were set to 4.75 and 9.50 ms, respectively. The number of points in the FID were set to 8192 in t_2 and to 256 in t_1. Durations of the longitudinal mixing, τ_{mix}, were set to 2, 4, 6 and 8 ms, from which $\tau_{mix} = 2$ ms gave the best result and hence was used in all 2D RFDR ^{31}P – ^{31}P NMR spectra.

2.1.5 Temperature calibration

Actual temperatures of the samples during acquisition in all NMR experiments were higher than those reported for the corresponding spectra due to the rotor heating caused by friction at high spinning speeds. The necessary corrections were made using the temperature calibration curve for MAS rates from 5 to 25 kHz, which is shown in figure 48.

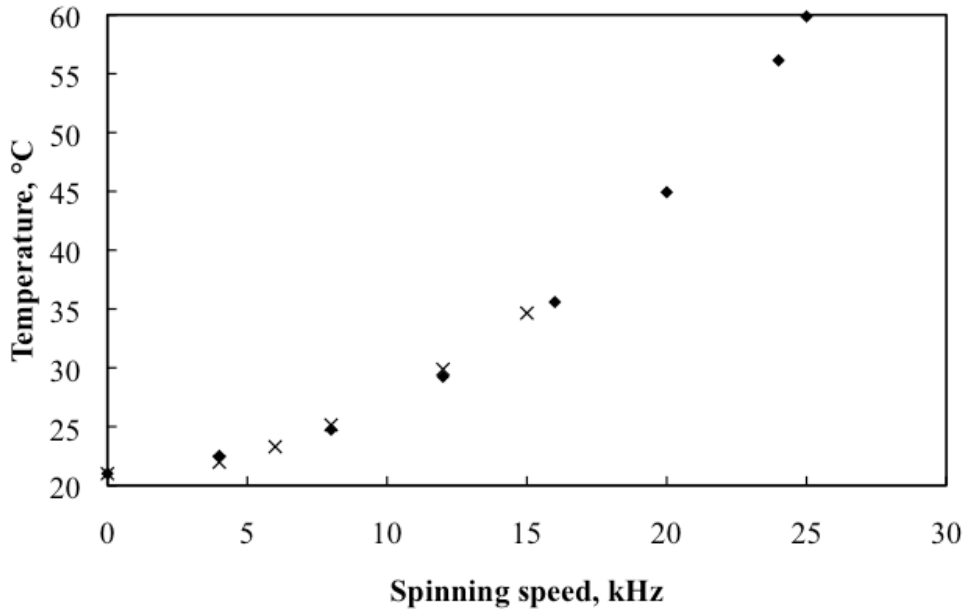

Figure 48 Temperature calibration curves for 4 mm (shown with crosses) and 2.5 mm (shown with squares) rotors in MAS NMR experiments at various spinning speeds.

The calibration curve was constructed by measuring temperature-dependent chemical shifts in the spectra of lead (II) nitrate and correlating them with the shifts in the room temperature spectra at various spinning speeds.[310] One can readily appreciate that the

actual temperatures of the samples in the experiments conducted under ambient conditions at a MAS rate of 25 kHz, were in the vicinity of 60°C.

2.1.6 Linear prediction

An insufficient number of points in the $^{31}P\{^{1}H, ^{19}F\}$ VT NMR experiments on solvent-cast PBFP resulted in a clipped FID, and hence no reliable information could be extracted from the signals, as seen in figure 49 A. Zero-filling an FID to 64,000 gave rise to baseline distortions, shown in figure 49 B, that obscured the signal appearance, which could lead to errors in peak analysis. In order to circumvent such problems, a combined detection-estimation Information Theory and the Matrix Pencil Method (ITMPM)[311] was implemented for an exponential FID modeling (forward linear prediction or LP). Forward linear prediction to 64,000 points was performed on the basis of the last 2048 points in an FID, and the number of signals in an FID were determined automatically using the Minimum Description Length (MDL) algorithm.[312] Correspondingly, the spectrum in figure 49 C shows that information lost due to FID clipping can be efficiently recovered using the ITMPM linear prediction method.

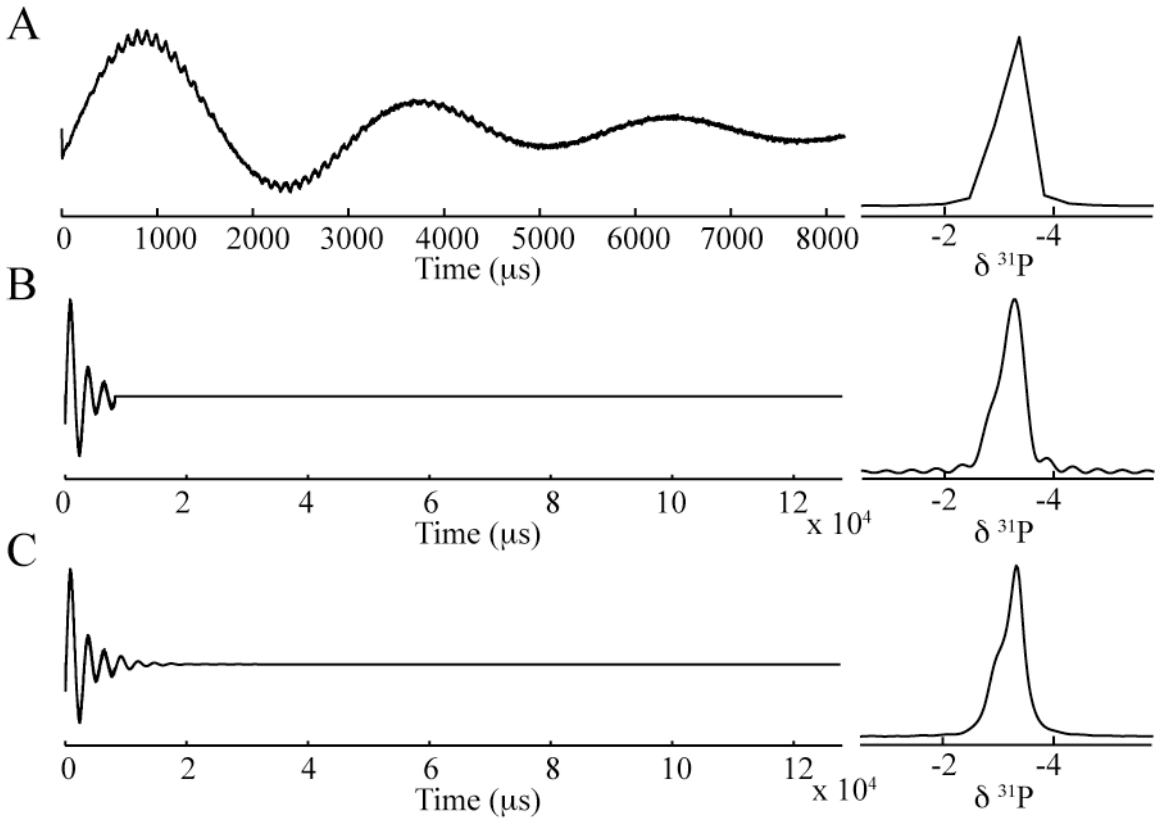

Figure 49 $^{31}P\{^{1}H, ^{19}F\}$ NMR of solvent-cast PBFP at 150°C and a MAS rate of 10 kHz. Unprocessed clipped FID and the corresponding spectrum (A); FID zero-filled to 64,000 and the corresponding spectrum (B); FID linear-predicted to 64,000 points using ITMPM-MDL algorithm and the corresponding spectrum (C).

2.2 Synthetic procedures

2.2.1 General procedures

Hexachlorocyclotriphosphazene, phenol, trifluoroethanol, $LiN(SiMe_3)_2$, SO_2Cl_2 and PCl_3 were purchased from Sigma-Aldrich and used as received, unless stated otherwise. Sodium metal was obtained from Sigma-Aldrich and was stored under an atmosphere of argon to avoid surface oxidation. All solvents were dried and purified via an MBraun MB SPS solvent purification system. Air and moisture sensitive reactions were carried out using common Schlenk, high vacuum and glove box techniques. A custom-made vacuum line equipped with an Edwards RV12 pump and a customized MBraun Unilab glove box were operated under an atmosphere of dry argon. Unless stated otherwise, all PBFP samples were prepared from the material obtained as a courtesy of Dr. Christine deDenus of Hobart and William Smith Colleges, New York.

2.2.2 Synthesis of batch 1 PBFP via thermal ring-opening polymerization of hexachlorocyclotriphosphazene

Hexachlorocyclotriphosphazene (2.00 g, 5.75 mmol) was loaded into a 15 × 2.5 cm Pyrex polymerization tube in a glove box. The tube was evacuated for 35 min, flame sealed and placed in an oven at 250°C. The oven was designed specifically to accommodate this type of polymerization, as depicted in figure 50. The tube was clamped onto the platform and was constantly agitated throughout the entire polymerization process to ensure homogeneity of the propagation of polymeric chains

and to minimize cross-linking. The speed of the electric motor was regulated with a rheostat.

Figure 50 Design of an oven used for the thermal ring-opening polymerization. Expansions show a platform with a Pyrex polymerization tube containing poly[dichlorophosphazene] (A) and an electric motor (B).

As mentioned previously, chain propagation during thermal ROP is an unpredictable process which is further complicated due to thermal cross-linking that occurs at later stages of polymerization. As a result, the reaction must be terminated before depletion of the cyclic trimer results in a significant retardation of chain growth and when cross-linking is minimal. Correspondingly, ROP is controlled via observation of the viscosity of phosphazene melt. Optimum conversion to high molecular weight polymer is reached when the polymer remains at the top of the polymerization tube upon inversion. Changes in viscosity were monitored every hour for the first five hours, followed by intervals of 30, 15 and 5 min at later stages of the polymerization. The reaction was complete in 7 h, 15 min forming a mixture of the unreacted cyclic trimer, oligomers, high molecular weight polymer and some cross-linked species.

The polymerization tube was opened under an atmosphere of dry argon, and the chlorinated polymer was subsequently extracted with dry dichloromethane (3 × 10 mL) and transferred to a 250 mL round bottomed flask containing 75 mL of dichloromethane and a stir bar and equipped with a condenser. The mixture was then allowed to completely dissolve (2 h). Poly[dichlorophosphazene] is a translucent, rubbery, air-sensitive material which undergoes a rapid hydrolysis of P–Cl bonds upon contact with trace moisture, resulting in a cross-linked polymer matrix which is highly insoluble in organic media and therefore unsuitable for further substitutions. Subsequently, chlorinated polymer side-chains were substituted with trifluoroethoxy units, via reacting with solution of sodium trifluoroethoxide (4.21 g, 34.5 mmol) in 1,4-dioxane at 0°C.

Sodium trifluoroethoxide was prepared by loading Na metal (0.800 g, 34.8 mmol) into a 150 mL two-neck round bottomed flask containing 25 mL of 1,4-dioxane. To this

stirred solution, a solution of 2,2,2-trifluoroethanol (2.48 mL, 34.5 mmol) in 25 mL of 1,4-dioxane was slowly added via syringe. This solution was heated to reflux for 2 h, followed by an additional 10 h of stirring at ambient temperature. The reaction mixture was filtered through a medium porosity sintered glass funnel and slowly added to a stirring solution of poly[dichlorophosphazene] at 0°C.

The mixture was heated to reflux for 4 h and allowed to cool to room temperature whereupon stirring was continued for an additional 4 h. The solvents were removed under reduced pressure and the resulting solids were washed with water (4 × 30 mL) to remove occluded sodium chloride. The polymer was then dissolved in 5 mL of THF and precipitated via a continuous stream addition into rapidly stirring hexanes (150 mL). Further removal of excess sodium trifluoroethoxide and low molecular weight oligomers was achieved by repeating the precipitation twice more using acetone as the solvent. The solvents were further removed under vacuum (30 h), resulting in a yellow-white flexible polymer which could be easily drawn into strings.

2.2.3 Synthesis of batch 2 PBFP via thermal ring-opening polymerization of hexachlorocyclotriphosphazene

Batch 2 PBFP was prepared on the same scale, and using the same procedures as batch 1 (*vide supra)*. The thermal polymerization was complete in 8 h, 5 min, and the chlorinated polyphosphazene was subjected to further work-up according to the aforementioned procedures. Upon substitution, the mixture of polymer and sodium trifluoroethoxide was stirred for 4 h at reflux, followed by an additional 20 h at ambient temperature. PBFP was then purified by three sequential precipitations from hexane and dried under vacuum for 24 h. The resulting material exhibits slightly a different physical appearance than batch 1, being less flexible.

2.2.4 Synthesis of PBFP via living cationic polymerization of $Cl_3P{=}NSiMe_3$ at ambient temperature

$LiN(SiMe_3)_2$ (14.9 g, 89.4 mmol) was loaded into a 500 mL two-neck round bottomed flask, equipped with a stir bar and a swivel frit apparatus. The reaction flask was evacuated for 30 min, and to it, dry Et_2O (200 mL) was vacuum transferred, resulting in a pale-yellow suspension. The suspension was cooled to $0^{\circ}C$ in an ice bath, and PCl_3 (7.80 mL, 89.4 mmol) was added in a dropwise manner. The mixture was slowly warmed to room temperature and allowed to stir for 1 h. The flask was again cooled to $0^{\circ}C$, and SO_2Cl_2 (7.25 mL, 89.4 mmol) was slowly added via syringe. The reaction was allowed to stir at $0^{\circ}C$ for 1 h, followed by an additional 45 min at ambient temperature. Subsequent filtration yielded a clear pale yellow filtrate. The volatiles (Et_2O, $ClSiMe_3$)

were removed *in vacuo* and a clear colorless liquid $Cl_3P{=}NSiMe_3$ was isolated (13.1 g, 65.3%) by distillation of the remaining residue under static vacuum at 57°C. ^1H NMR ($CDCl_3$): δ 0.18. $^{31}P\{^1H\}$ NMR ($CDCl_3$): δ −54.3 ppm.

For the bulk phase polymerization, a Pyrex polymerization tube was loaded with $Cl_3P{=}NSiMe_3$ (1.00 g, 4.46 mmol) and a trace amount of PCl_5 (0.0100 g, 0.0480 mmol). The tube was evacuated and the mixture was allowed to stand for 24 h, leading to the formation of two phases. The contents were then dissolved in dry dichloromethane (25 mL) and subsequently added to a dry 1,4-dioxane (25 mL) solution of sodium trifluoroethoxide (1.09 g, 8.92 mmol). The sodium trifluoroethoxide was prepared as previously described *(vide supra)*. The polymer was substituted and purified as described in chapter 2.2.1. The isolated PBFP (0.321 g, 62.0%) was dried under vacuum for 36 h before future use.

2.2.5 Preparation of solvent-cast samples

A viscous solution of PBFP (0.5 g) in acetone (3 mL) was poured onto a 10 × 10 cm glass plate. The solvent was then allowed to evaporate under ambient conditions (14 h) and the thin polymer film was removed from the glass using a razor blade. The polymer was rolled into strips, which were cut to fit in a 2.5 mm Vespel rotor. The same procedure was performed for all PBFP samples studied.

2.2.6 Preparation of heat-treated samples

Heat-treated PBFP, heat-treated batch 1 PBFP and heat-treated batch 2 PBFP were prepared via 11 cycles of heating of the respective polymers. For each sample, cycles consisted of annealing materials for 1 h at 150°C, followed by slow cooling to ambient temperature.

2.2.7 Preparation of phenoxy-substituted hexachlorocyclotriphosphazene

The preparation of sodium phenoxide was similar to that of sodium trifluoroethoxide, where fresh Na metal (0.079 g, 3.43 mmol) was allowed to react with a 1,4-dioxane (25 mL) solution of phenol (0.290 mL, 3.43 mmol) for 12 h at 60°C. Hexachlorocyclotriphosphazene (1.00 g, 2.86 mmol), purified via recrystallization,[89] was loaded into a 150 mL round bottomed flask containing 50 mL of dry THF. To this stirring solution, sodium phenoxide (0.400 g, 3.43 mmol, 1.2 equiv) in 20 mL of THF was slowly added via syringe. The mixture was allowed to stir for 24 h at ambient temperature, followed by subsequent removal of the solvents under reduced pressure. The resulting yellow opaque solid was a mixture of unsubstituted, mono- and di-substituted cyclic trimer.

2.2.8 Preparation of partially trifluoroethoxy-substituted poly[dichlorophosphazene]

The experimental procedure was identical to the preparation of batch 1 PBFP, where poly[dichlorophosphazene] (2.00 g, 5.75 mmol) was allowed to react with 3 equiv of sodium trifluoroethoxide (2.11 g, 2.86 mmol) to ensure approximately 50% substitution of the chlorine atoms. Due to the moisture sensitivity of the partially substituted PBFP, the removal of occluded salt with water was omitted. Purification via precipitations into hexane were performed in a glove box. The polymer was dried under vacuum for 30 h and then packed into a 2.5 mm rotor under a dry argon atmosphere.

2.2.9 Preparation of the hexachlorocyclotriphosphazene at different stages of polymerization

Equal amounts of hexachlorocyclotriphosphazene (1.00 g, 2.86 mmol) were loaded into three Pyrex polymerization tubes which were then flame sealed and placed into the oven at 250°C. The tubes were removed and allowed to cool to ambient temperature after 3, 8.5 and 17.5 h. The materials were subsequently extracted from the tubes and packed into 4 mm Vespel rotors under an atmosphere of dry argon.

2.3 Software

All NMR spectra were processed and deconvolved using Mestrelab Research S.L.® MestReNova© 5.2.5 and the MatNMR[313] 3.9 NMR processing toolbox (© Jakko van Beek) for The MathWorks™ MATLAB® 6.5. Chemical structures and reaction schemes were created in CambridgeSoft® ChemDraw© Ultra 11.0.1. Illustrations and figures were created in Adobe® Illustrator© CS4. Microsoft® Excel© 2008 for Mac was used for numerical data processing and plotting.

3 RESULTS AND DISCUSSION

3.1 Overview

A variety of ^{1}H, ^{19}F, ^{31}P and ^{13}C solid-state NMR methods was applied to a series of poly[*bis*(trifluoroethoxy)phosphazene] (PBFP) preparations, and demonstrates the potential of NMR as a tool for probing microscopic properties of different environments of these semicrystalline polymer systems.

Often the resolution of ^{1}H, ^{19}F, ^{31}P MAS NMR is insufficient to allow for in-depth characterization of the amorphous and crystalline domains within a polymer, which can be attributed to number of reasons. Moreover, the polymer side-chains experience high rotational and torsional mobility, and as a result, proton and fluorine nuclei are insensitive to their local environment and hence occur in a narrow frequency range making the need for higher resolution even more acute. Poor spectral resolution is caused by homonuclear dipolar interactions that are too strong to be efficiently removed by spinning at the magic angle and with modern decoupling methods at currently available power levels. Spinning speeds in excess of 25 kHz are required in many situations to effectively average out the interactions that lead to line-broadening in order to achieve resolution that is suitable for elucidating the domain structures. Poor resolution in ^{31}P spectroscopy can also result from inhomogeneous broadening due to a distribution of environments of the backbone, where the corresponding signals are close in frequencies and thus merge into one featureless peak. In addition, its resolution can be further compromised by the residual dipolar couplings with nitrogen, which is spin-1 and 99% abundant. Nitrogen's quadrupolar interactions tend to be very strong, often as much as 4 MHz. Dipolar couplings to a quadrupolar nucleus cannot be completely averaged out under MAS conditions, therefore spinning speeds in excess of 25 kHz alone will not

suffice and ^{14}N decoupling will be necessary, which can only be achieved using decoupling sequences designed to be effective over very large offsets such as adiabatic pulses. These decoupling methods are not currenlty available in this facility.

At this stage, no further improvements in ^{1}H, ^{19}F, ^{31}P MAS NMR resolution can be achieved, nor are proposed. These experiments are useful upon comparing spectra of solvent-cast and heat-treated PBFP samples, where lineshapes suggest that only signals from crystalline and amorphous domains of the polymer can be distinguished; however, no detailed information about crystalline phases is provided.

On the other hand, carbon-13, which is 1% abundant and has a gyromagnetic ratio ¼ that of proton, has direct dipole couplings that are relatively weak, and can in principle offer excellent spectral resolution. In addition, mobility of carbon in the polymer side chain is somewhat limited, making this nucleus sensitive to its immediate environments. To achieve good spectral resolution a combination of fast magic-angle spinning and simultaneous $\{^{1}H, ^{19}F\}$ XY-16 double decoupling is required. $^{13}C\{^{1}H, ^{19}F\}$ MAS NMR spectra of PBFP *vide infra* reveal complex structures, with signals composed of multiple overlapping components. Observations and comparisons of chemical shifts, intensities, widths and Gaussian/Lorentzian fractions obtained via deconvolution analyses, for different PBFP samples, were used to make preliminary assignments of the amorphous and crystalline phases.

^{31}P MAS NMR studies were performed on the hexachlorophosphonitrillic trimer at various stages of thermal polymerization. Spectra reveal the presense of primarily cyclic low molecular weight species at earlier stages of the ring-opening process. These are seen to decrease with time, whilst a new peak corresponding to chlorinated

polyphosphazene arises. This method has potential to provide quantitave information about rates of depletion of the initial cyclic trimer species, rates of formation of the high polymer and the rate of propagation of cross-linking processes.

3.2 $^{1}H\{^{19}F\}$ MAS NMR of solvent-cast and heat-treated PBFP obtained via thermal ring-opening polymerization of hexachlorocyclotriphosphazene

^{1}H MAS NMR spectra of solvent-cast (SC) and heat-treated (HT) PBFP samples were obtained. Their respective signals were deconvolved into several components, which were preliminarly assigned to the crystalline and amorphous environments of the polymer. A comparison of the results of the HT and the SC samples revealed substantial differences in crystallinity upon heat-treatment.

3.2.1 One-dimensional $^{1}H\{^{19}F\}$ MAS NMR

Proton MAS NMR spectra of solvent-cast and heat-treated PBFP acquired at a MAS rate of 25 kHz are shown in figure 51. In both spectra, the signal near 4.7 ppm exhibits complex structure with several overlapping components. Differences between signals of the two samples are noticeable at a glance; however, in order to make difinitive observations upon differences in crystallinity between SC and HT PBFP, quantitative information about parameters for each peak needs to be extracted, via peak deconvolution analysis. This decomposes complex signals that contain separate contributions, giving their individual chemical shifts, widths, intensities, areas and Gaussian/Lorentzian

fractions. This extremely useful and versatile method; however, can give rise to non-unique solutions when applied to poorly resolved signals. In order to obtain the most reliable and accurate information, it is therefore necessary to retain consistency between analyses of two different preparations of the same material. Accordingly, the peak parameters used in the deconvolution analyses of the proton spectra of solvent-cast and heat-treated PBFP are locked in, such that only changes in the intensities are allowed. This entailed the search for a model, changing the number of lines, their chemical shifts, widths and Gaussian/Lorentzian fractions, until one is found that fits both spectra, where only the intensities are changed.

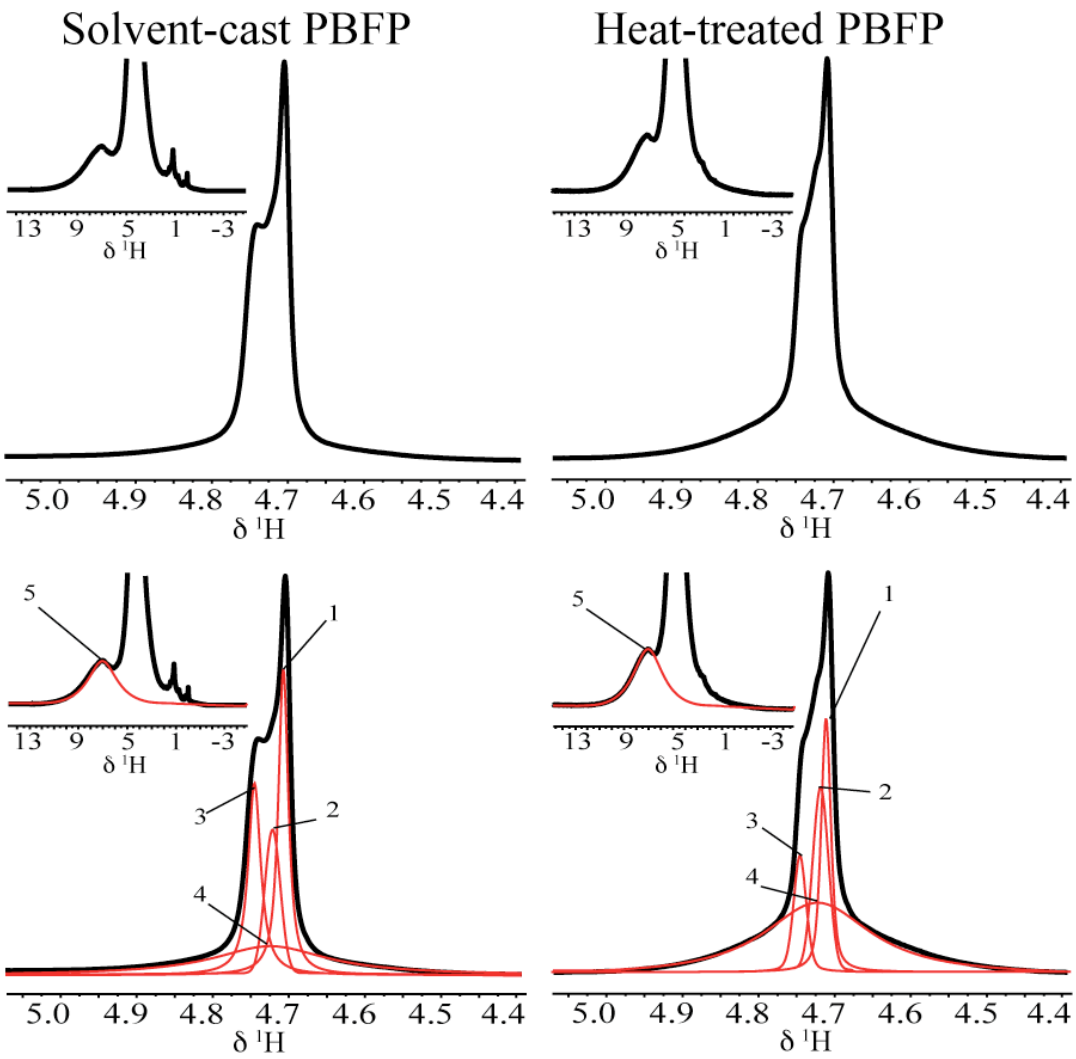

Figure 51 500 MHz $^{1}H\{^{19}F\}$ MAS NMR spectra of solvent-cast and heat-treated PBFP. MAS rate 25 kHz.

Multiple trials reapeatedly confirm the presence of a total of five peaks in the proton spectra, which are labelled and will be referred to as peaks 1 through 5 as shown in the bottom of figure 51. Their respective parameters are tabulated in Table 1. Peaks 1 through 3 are Lorentzian in character and relatively narrow, between 11 and 24 Hz wide. In contrast, peaks 4 and 5 are Gaussian and much broader, being 215 and 501 Hz wide,

respectively. Upon side-by-side comparison of the results obtained via deconvolution analyses of SC and HT PBFP, one can readily appreciate significant changes in distribution between peak intensities. In the SC spectrum, all lines contribute to the total signal area approximately equally, with the exception of peak 5, which has rather low intensity. In contrast, the contributions of lines 1 through 3 in the HT spectrum are reduced significantly. Also worth mentioning is the group of narrow peaks with low intensity seen in the spectrum of solvent-cast PBFP at about 1.5 ppm. These were assigned to the trace water or solvent trapped inside the polymer matrix. Correspondingly, these peaks are not observed in the spectrum upon heat-treatment, which indicates that the high temperature regime of the thermal treatment resulted in the evaporation of impurities.

Table 1 Peak parameters in the $^{1}H\{^{19}F\}$ MAS NMR spectra of solvent-cast and heat-treated PBFP.

Sample	SC					HT				
Peak #	**1**	**2**	**3**	**4**	**5**	**1**	**2**	**3**	**4**	**5**
Chemical shift (ppm)	4.69	4.70	4.72	4.73	7.20	4.69	4.70	4.72	4.73	7.20
Normalized intensity†	0.77	0.36	0.48	0.08	0.02	0.63	0.46	0.29	0.17	0.04
Width (Hz)	11.1	23.8	21.9	215	501	12.4	21.8	17.8	216	429
Area (%)	25.8	18.9	24.7	17.5	13.1	16.6	15.9	9.50	44.0	14.0

† Intensities normalized on the basis of the maximum intensity of the respective signal

Recall that under ambient conditions, PBFP contains amorphous and crystalline regions that are characterized by different molecular dynamics, and therefore will give rise to signals with different chemical shifts, intensities and widths. Correspondingly, signals from mobile and disordered regions appear as narrow Lorenztian lines, whilst

rigid regions where motion is restricted, result in broad Gaussian peaks. As the heat-treatment of PBFP causes phase transitions and increases its overall crystallinity, these changes must be reflected in the corresponding solid-state NMR spectra. As a result, it can be inferred that peaks 1 and 3 correspond to amorphous environments of PBFP, as they are narrow, Lorentzian, and decrease upon heat-treatment. At this stage, no definite conclusions can be drawn on component 2, other than that it becomes more intense upon heat-treatment, which implies that it is an ordered phase. Its lineshape and width, however, suggest that this signal cannot originate from the rigid crystalline domain, but rather an environment that is both ordered and mobile, such as mesophase. These are known to exist in this type of polymer, however at much higher temperatures. Further work with relaxation measurements at variable temperature will verify this assignment. In contrast, peaks 4 and 5 are broad Gaussian lines, which increase significantly upon heat-treatment and must therefore correspond to various crystalline formations of the polymer.

In conclusion, data shown in Table 1 suggests that the overall crystallinity of PBFP upon heat-treatment is increased by 27.4%. In order to confirm the reliability and accuracy of these analyses, different techniques must be used to independently verify the number of components in the spectra, such as the DIVAM experiment.

3.2.2 ^{1}H DIVAM experiment

The DIVAM experiment was set up, such that it could select for signals in the ^{1}H spectrum of PBFP on the basis of differences in their respective relaxation rates, and hence in principle should separate amorphous components from crystalline components. As discussed previously, differences in mobilities of the environments in the polymer determine their nutation profile, where crystalline signals 'lag' behind the amorphous ones, as the excitation angle is increased. Figure 52 A shows the full nutation array for SC.

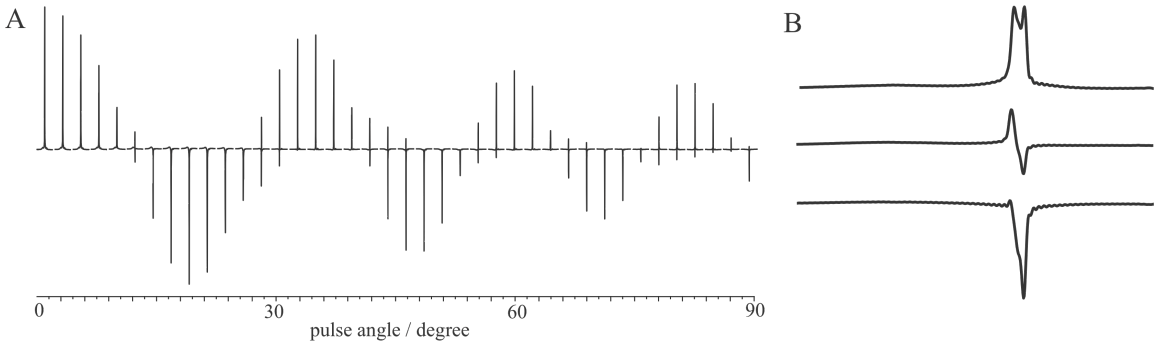

Figure 52 (A) 500 MHz ^{1}H MAS NMR direct DIVAM nutation experiment on solvent-cast PBFP. MAS rate 25 kHz. (B) Expansion of the array at the mini-pulse angles of 9º, 10.8º and 12.6º.

The spectra in the DIVAM array exhibit regular nutation behavior for all of the observed signals. The expansions of selected spectra near the first zero-crossing, shown in figure 52 B, clearly show three narrow lines crossing zero at slightly different excitation angles. Therefore, the DIVAM experiment on SC and HT PBFP confirms the presence of three signals from mobile regions of the polymers.

3.3 $^{19}F\{^{1}H\}$ MAS NMR of solvent-cast and heat-treated PBFP obtained via thermal ring-opening polymerization of hexachlorocyclotriphosphazene

3.3.1 One-dimensional $^{19}F\{^{1}H\}$ MAS NMR

As mentioned previously, $^{19}F\{^{1}H\}$ MAS NMR of PBFP is expected to provide limited spectral information, which indeed is seen to be the case (shown in figure 53). Despite the relatively narrow linewidth of the signal at –77.6 ppm, both spectra lack the structural details to guide the deconvolution analyses, which in turn suggest that three signals are present. Results of the most consistent and accurate deconvolutions are tabulated in table 2 and shown in the bottom of figure 53.

Table 2 Peak parameters in the $^{19}F\{^{1}H\}$ MAS NMR spectra of solvent-cast and heat-treated PBFP.

Sample	SC			HT		
Peak #	**1**	**2**	**3**	**1**	**2**	**3**
Chemical shift (ppm)	–77.6	–77.2	–76.8	–77.6	–77.2	–76.8
Normalized intensity[†]	0.64	0.48	0.09	0.59	0.57	0.25
Width (Hz)	31	42	176	32	39	176
Area (%)	34.6	36.0	29.4	21.9	29.7	48.4

[†] Intensities normalized on the basis of the maximum intensity of the respective signal

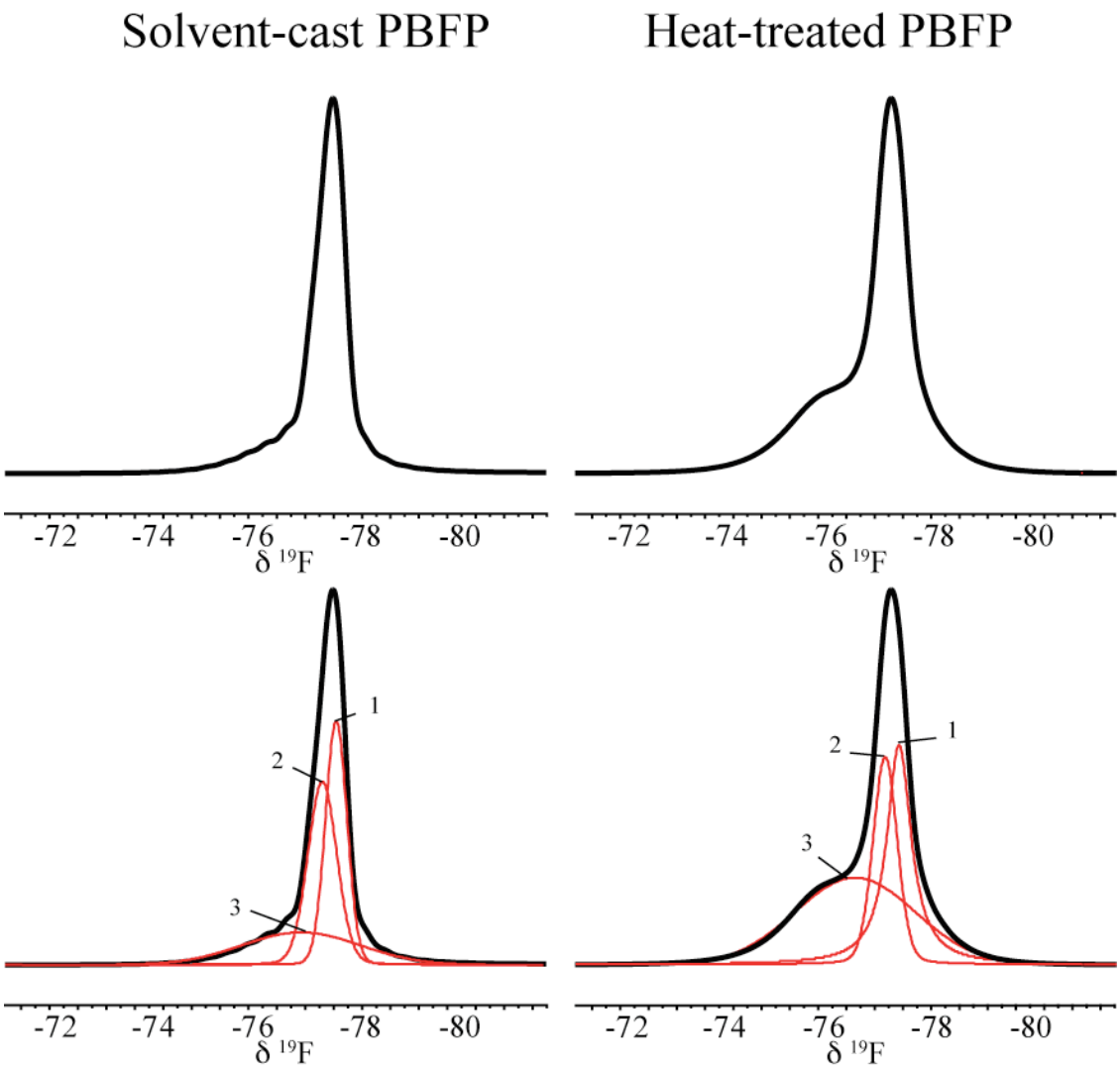

Figure 53 469 MHz $^{19}F\{^{1}H\}$ MAS NMR spectra of solvent-cast and heat-treated PBFP. MAS rate 25 kHz.

Peaks 1 and 2 in the $^{19}F\{^{1}H\}$ NMR spectrum of solvent-cast PBFP exhibit somewhat similar Lorentzian appearance, where their widths are 31 Hz and 42 Hz, respectively. The mostly Gaussian shaped component (3) occurs at –76.8 ppm and is 176 Hz wide. Peaks 1, 2 and 3 in the spectrum of the solvent-cast PBFP contribute 34.6%, 36.0% and 29.4% to the overall area under the signal, respectively. Changes upon heat-treatment are consistent with $^{1}H\{^{19}F\}$ MAS NMR, such that line 1 decreased in the

spectrum of HT PBFP and hence can be assigned to the amorphous domain of the polymer. Similar behavior of line 2 is observed, where it increases upon heat-treatment, which leads to a conclusion that it corresponds to the mesophase region of PBFP. In contrast, Gaussian component 3, 176 Hz wide, is approximately five times broader than the remaining two lines, increases upon heat-treatment, and is therefore assigned to the crystalline domain. The overall crystallinity of PBFP, as determined from peak areas, increases by 19% upon heat-treatment, which is in slight disagreement with the results reported for the ^{1}H NMR spectra of the polymer due to inevitable errors encountered during deconvolution analyses.

At this stage, it was helpful to use the DIVAM experiment to verify the number of mobile components in the signal.

3.3.2 ^{19}F DIVAM experiment

The ^{19}F DIVAM nutation experiment, tuned to select on the basis of spin-spin relaxation, was applied to SC and HT PBFP. The ^{19}F DIVAM nutation array of solvent-cast PBFP is shown in Figure 54 A, and the expansions of the spectra near the first zero-crossing are also shown in figure 54 B.

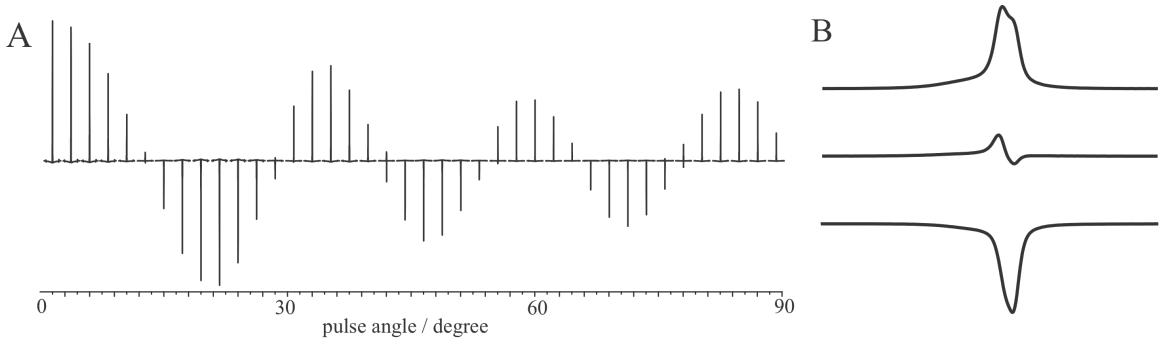

Figure 54 (A) 469 MHz ^{19}F MAS NMR direct DIVAM nutation experiment on solvent-cast PBFP. MAS rate 25 kHz. (B) Expansion of the array showing signals at the mini-pulse angles of 9º, 10.8º and 12.6º.

Upon closer examination of the spectra of the direct DIVAM nutation array near the first zero-crossing, one can readily appreciate that the main signal contains two narrow components. Consistent with the nutation behavior seen in the ^{1}H DIVAM array of SC, these narrow lines cross zero at slightly different excitation angles; a similar conclusion can be made, as with the proton NMR spectra of PBFP, where in this case, there are two narrow components that correspond to the amorphous and mesophase domains in the polymer.

3.4 $^{31}P\{^{1}H, ^{19}F\}$ MAS NMR of solvent-cast and heat-treated PBFP obtained via thermal ring-opening polymerization of hexachlorocyclotriphosphazene

High degree of heterogeneity in the PBFP backbone environments in combination with the residual quadrupolar coupling to nitrogen conspire to cause poor resolution in the $^{31}P\{^{1}H,^{19}F\}$ NMR spectrum. As seen in figure 55 below, both spectra reveal two broad signals at –7.5 and –3.5 ppm, respectively.

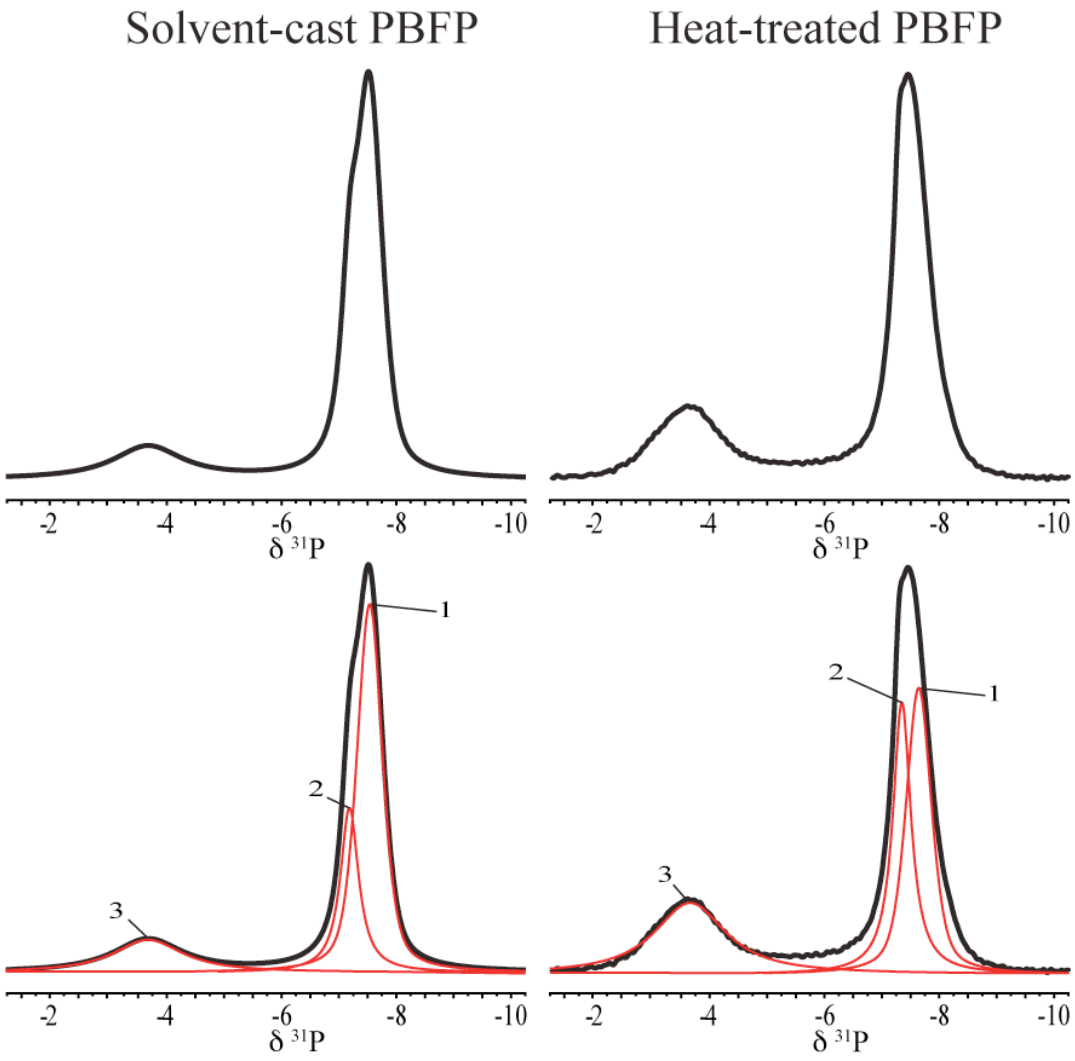

Figure 55 202 MHz $^{31}P\{^{1}H, ^{19}F\}$ MAS NMR spectra of solvent-cast and heat-treated PBFP. MAS rate 25 kHz.

The somewhat symmetrical lineshape and the lack of distinguishing features in the spectrum undermine the accuracy of the deconvolution analyses, and, as a result, the determination of the individual components of the signal is compromised. At this stage, the poor resolution in the room temperature phosphorous spectra of SC and HT PBFP results in only three peaks being indentified with any degree of certainty, as seen in figure 55, bottom, and tabulated in Table 3. This is a departure from the $^{1}H\{^{19}F\}$ and $^{19}F\{^{1}H\}$ deconvolution analyses, where the DIVAM nutation experiment was employed to independently verify the number of lines contributing to the main signals. The acknowledged interpretation; however, is supported by the $^{31}P\{^{1}H,^{19}F\}$ MAS one-dimensional NMR, $T_{1\rho}$ measurements and variable temperature ^{31}P NMR experiments, which confirm the presence of two components in the main peak near –7.5 ppm, as will be discussed in the sections to follow.

Table 3 Peak parameters in the $^{31}P\{^{1}H,^{19}F\}$ MAS NMR spectra of solvent-cast and heat-treated PBFP.

Sample	SC			HT		
Peak #	**1**	**2**	**3**	**1**	**2**	**3**
Chemical shift (ppm)	–7.51	–7.11	–3.45	–7.51	–7.11	–3.45
Normalized intensity[†]	0.90	0.40	0.08	0.69	0.66	0.18
Width (Hz)	149	123	341	149	123	342
Area (%)	62.6	26.2	11.2	40.4	36.7	22.9

[†] Intensities normalized on the basis of the maximum intensity of the respective signal

Lines 1 and 2, 149 and 123 Hz wide, respectively, exhibit similar Lorentzian shapes, whilst the Gaussian line 3 is almost twice as broad. Being consistent with the deconvolution analyses of the $^{1}H\{^{19}F\}$ and $^{19}F\{^{1}H\}$ MAS spectra of PBFP, it can be inferred that line 1 corresponds to the amorphous domain in the polymer, as it becomes less intense upon heat-treatment. Similarly, peaks 2 and 3 are assigned to the mesophase and crystalline regions of the polymer, respectively, as their intensities increase significantly in HT PBFP. The overall crystallinity of the heat-treated polymer increases by 11.7%, as determined from the area under peak 3.

3.5 $^{13}C\{^{1}H, ^{19}F\}$ MAS NMR of solvent-cast and heat-treated PBFP obtained via thermal ring-opening polymerization of hexachlorocyclotriphosphazene

Previous studies[308] of SC and HT using ^{13}C MAS NMR resulted in extremely poor spectral resolution revealing signals from CF_3 and CH_2 carbons with widths on the order of 25-35 ppm (3.1-4.4 kHz), at 71 and 11 ppm, respectively, as seen in figure 56. For this assignment, ^{1}H and ^{19}F decoupling gating was used, where the reintroduced heteronuclear coupling interactions split or broaden corresponding carbon signals in the spectrum. Attempted deconvolution analyses fail to give accurate and consistent information about the number of components in the signals. Some changes in the lineshape occur upon heat-treatment; however, no definite interpretations can be made for spectra with such resolution.

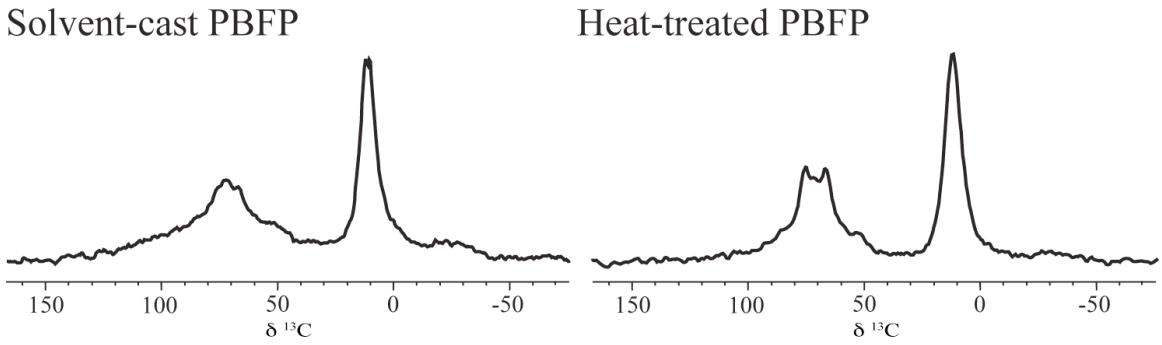

Figure 56 125 MHz $^{13}C\{^{1}H,^{19}F\}$ MAS NMR spectra of solvent-cast and heat-treated PBFP at a MAS rate of 15 kHz and TPPM decoupling.

Currently, very high resolution in carbon-13 spectra of this representative polymer system can be achieved by using direct acquisition, as well as $^{1}H \rightarrow {}^{13}C$ and $^{19}F \rightarrow {}^{13}C$ cross-polarization, under fast-MAS conditions and simultaneous high-power $\{^{1}H,^{19}F\}$ double decoupling with the XY-16 pulse sequence, as will be shown in what follows. Application of the DIVAM filter preceding the CP spin-lock field allows the determination of the number of components comprising the signals, by transferring the magnetization from either the amorphous or crystalline domain of the abundant spin to carbon.

3.5.1 $^{13}C\{^{1}H,^{19}F\}$ one-dimensional MAS NMR

The one-dimensional $^{13}C\{^{1}H,^{19}F\}$ MAS NMR spectra of solvent-cast and heat-treated PBFP are shown in figure 57. Two signals, at 11 and 71 ppm, respectively, were already known to correspond to the CH_2 and CF_3 carbons.[308] Peaks in both spectra exhibit fine structural details containing several well-resolved components from different environments of the polymer. The subsequent deconvolution analyses suggest six separate contributions to the CF_3 signals of SC and HT and five to the CH_2 signals, respectively, as seen in figure 57. Results of the most consistent deconvolutions are summarized in Table 4.

Lines 1 through 5 in the CF_3 signal are in the vicinity of 30 Hz wide leading to a conclusion that they must originate from environments with significant molecular mobility. However, they all reduce in intensity upon heat-treatment, which is a departure from the interpretations of ^{1}H, ^{19}F and ^{31}P spectra where the narrow component, believed

to correspond to the mesophase, is seen to increase in HT PBFP. It can be therefore be inferred that the high spectral resolution and the sensitivity of the carbon nucleus to its immediate environment gives rise to multiple peaks representing the amorphous domains, interfacial regions and mobile regions with some degree of order retained (i.e. mesophase). In contrast, line 6 is broad (~ 125 Hz wide) and increases dramatically upon heat-treatment, and hence is consistent with behavior expected for crystalline domains.

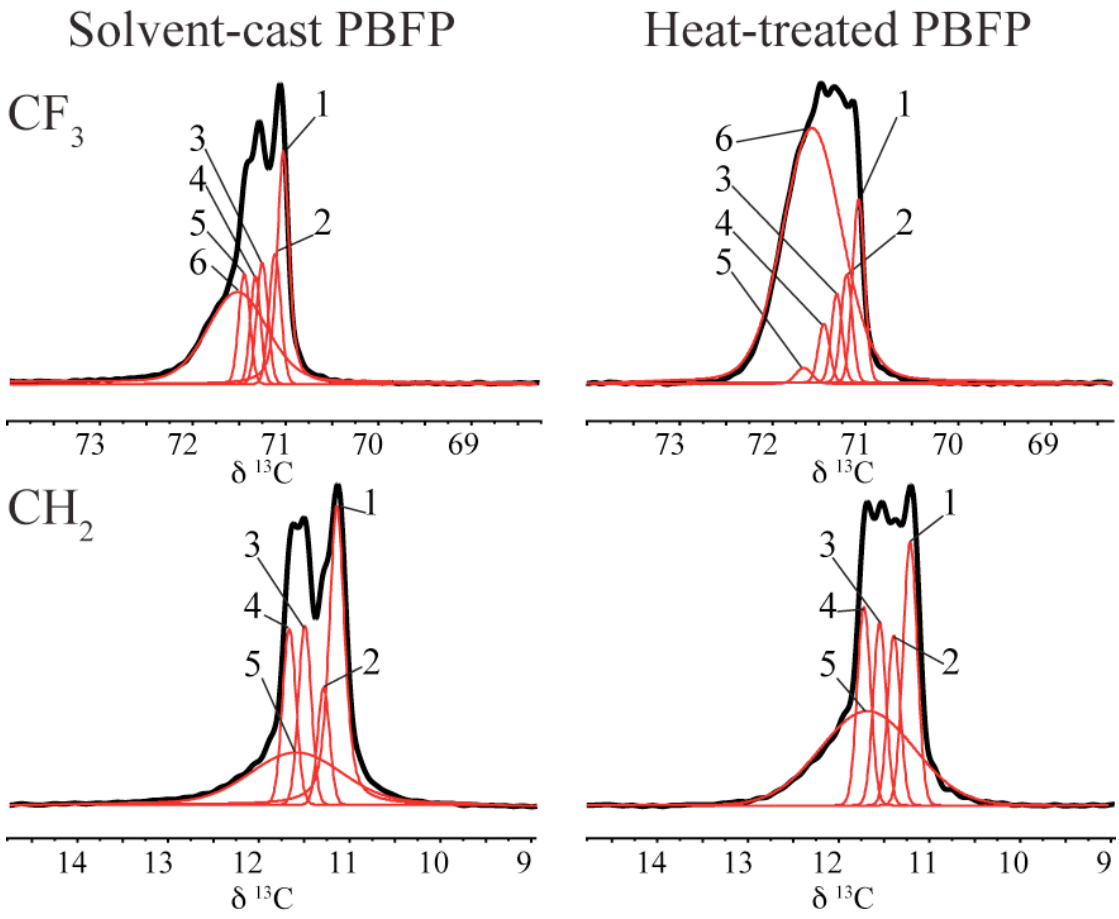

Figure 57 Expansions of the CF_3 and CH_2 signals in the 125 MHz $^{13}C\{^1H,^{19}F\}$ MAS NMR spectra of solvent-cast and heat-treated PBFP. MAS rate 25 kHz.

Table 4 Peak parameters in the $^{13}C\{^{1}H,^{19}F\}$ MAS NMR spectra of solvent-cast and heat-treated PBFP.

Sample	SC						HT					
Peak #	**1**	**2**	**3**	**4**	**5**	**6**	**1**	**2**	**3**	**4**	**5**	**6**
						CF_3						
Chemical shift (ppm)	70.89	71.04	71.38	71.26	71.58	71.75	70.91	71.13	71.31	71.55	71.69	71.79
Normalized intensity†	0.78	0.43	0.40	0.37	0.38	0.31	0.61	0.37	0.29	0.19	0.05	0.85
Width (Hz)	30.5	30.5	28.8	29.2	28.9	123.7	31.8	30.1	30.7	30.1	28.9	135.4
Area (%)	18.6	10.8	10.1	9.70	9.30	41.5	17.7	6.30	5.90	4.70	1.90	63.5
						CH_2						
Chemical shift (ppm)	11.01	11.22	11.45	11.67	11.57		11.01	11.22	11.45	11.66	11.56	
Normalized intensity†	0.98	0.38	0.55	0.54	0.17		0.82	0.52	0.58	0.62	0.30	
Width (Hz)	28.7	28.5	27.8	26.1	194		29.1	28.1	27.4	27.6	195	
Area (%)	26.7	11.5	14.7	15.3	31.8		19.5	12.7	13.9	14.6	39.3	

† Intensities normalized on the basis of the maximum intensity of the respective signal

The bottom of figure 57 shows five contributions to the CH_2 signal that exhibit somewhat different behavior upon heat-treatment, compared to CF_3. This can be mostly due to the differences in locations between the two groups with respect to the backbone. As a result, the magnitude of motion they undergo will be altered, as will be their immediate environments. Correspondingly, an unambiguous assignment for narrow peak 1 and broad peak 5 can be made, to the amorphous and crystalline phases, respectively. On the other hand, narrow peaks 2 through 4 are seen to increase upon heat-treatment, which must reflect either regions with different degrees of order, such as mesophase, or variations in chain conformations.

Further interpretations of the signal composition require additional information, such as rates of polarization transfer for different components and their nutation behavior in DIVAM experiments.

3.5.2 $^{13}C\{^{1}H,^{19}F\}$, $^{19}F \rightarrow {}^{13}C$ and $^{1}H \rightarrow {}^{13}C$ CPMAS NMR

Deconvolution analyses of the CF_3 and CH_2 signals were verified using the previously described consistent peak parameter model preserving chemical shifts, widths and Lorentzian/Gaussian fraction for signals in the $^{19}F \rightarrow {}^{13}C$ and $^{1}H \rightarrow {}^{13}C$ MAS spectra of solvent-cast and heat-treated PBFP, shown in figure 58 and tabulated in Table 5. Similarly, six and five components, for the CF_3 and CF_2 signals, respectively, can be revealed; the distribution in relative intensities is slightly different and depends on the CP efficiency of each component. Changes in the spectra upon heat-treatment are consistent with direct-polarization experiments.

Narrow lines 1 through 5 in the CF_3 signal of SC and HT (figure 58, top) have lower relative intensities with respect to the remaining crystalline peak 6. This is indicative of their high mobility, which hence confirms assignment of lines 1 – 5 to the various amorphous, interfacial or mesophase regions. Similarly, line 1 in the CH_2 signal decreases drastically upon heat-treatment and is therefore assigned to the amorphous domain of the polymer, whilst the remaining peaks increase. Being consistent with previous interpretations component 5 must correspond to the crystalline domain. At this point, the origin of lines 2 through 4 cannot be established with a high degree of

confidence, and the DIVAM experiment was employed to assist with determination of components.

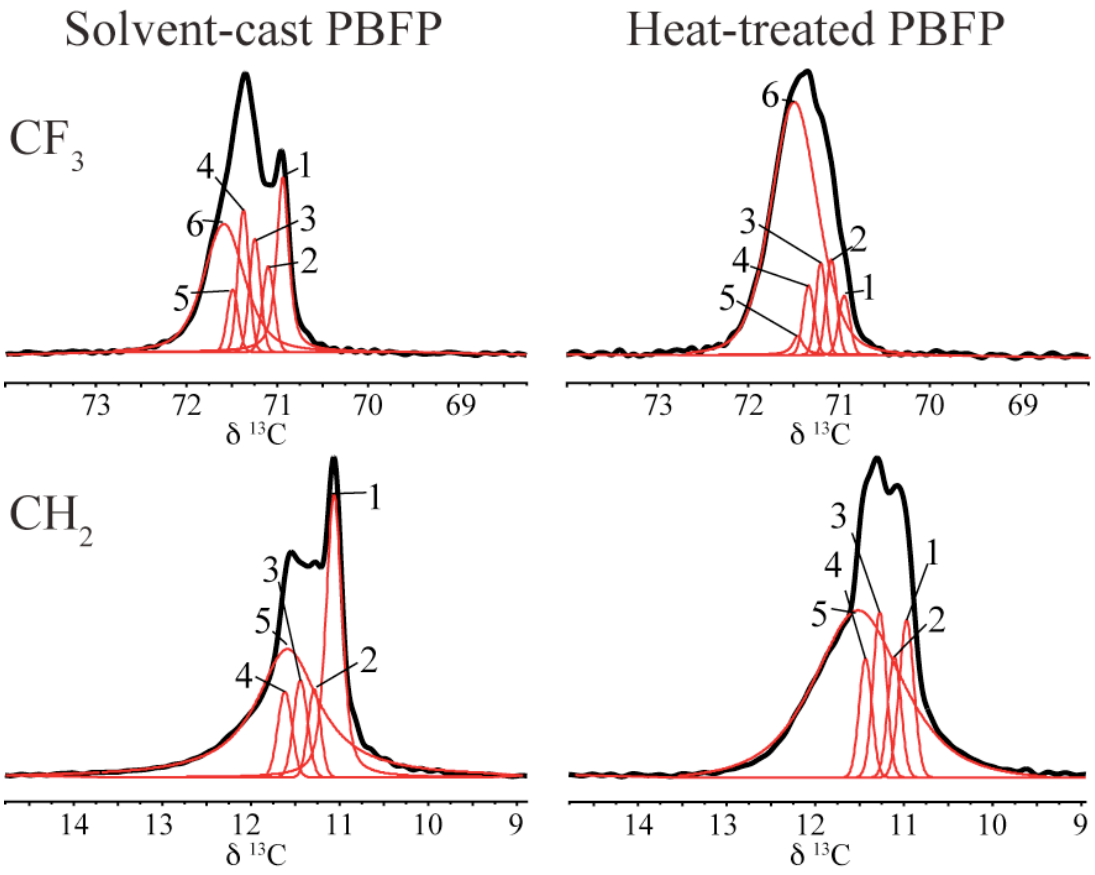

Figure 58 Expansions of the CF_3 and CH_2 signals in the 125 MHz $^{13}C\{^1H,^{19}F\}$ $^{19}F \rightarrow {}^{13}C$ (top) and $^1H \rightarrow {}^{13}C$ (bottom) CPMAS NMR spectra of solvent-cast and heat-treated PBFP. MAS rate 25 kHz.

Table 5 Peak parameters in the $^{13}C\{^{1}H,^{19}F\}$ $^{19}F \rightarrow {}^{13}C$ and $^{1}H \rightarrow {}^{13}C$ CPMAS NMR spectra of solvent-cast and heat-treated PBFP.

Sample	SC						HT					
Peak #	**1**	**2**	**3**	**4**	**5**	**6**	**1**	**2**	**3**	**4**	**5**	**6**
						CF_3						
Chemical shift (ppm)	70.89	71.04	71.38	71.26	71.58	71.75	70.91	71.13	71.31	71.55	71.69	71.79
Normalized intensity†	0.62	0.30	0.40	0.49	0.23	0.46	0.21	0.33	0.31	0.24	0.07	0.89
Width (Hz)	30.5	30.5	28.8	29.2	28.9	124	31.8	30.1	30.7	30.1	28.9	135
Area (%)	18.6	9.32	12.6	17.1	6.98	35.4	5.90	5.51	6.24	5.72	2.53	74.1
						CH_2						
Chemical shift (ppm)	11.01	11.22	11.45	11.67	11.57		11.01	11.22	11.45	11.66	11.56	
Normalized intensity†	0.88	0.28	0.30	0.27	0.40		0.49	0.39	0.51	0.37	0.53	
Width (Hz)	28.7	28.5	27.8	26.1	194		29.1	28.1	27.4	27.6	195	
Area (%)	26.7	9.14	8.34	7.92	47.9		9.15	7.20	9.85	6.9	66.9	

† Intensities normalized on the basis of the maximum intensity of the respective signal

3.5.3 $^{19}F \rightarrow {}^{13}C$ and $^{1}H \rightarrow {}^{13}C$ CP DIVAM experiments

$^{19}F \rightarrow {}^{13}C$ and $^{1}H \rightarrow {}^{13}C$ cross-polarization DIVAM experimental results for solvent-cast and heat-treated PBFP are shown in figure 59 (*vide infra*).

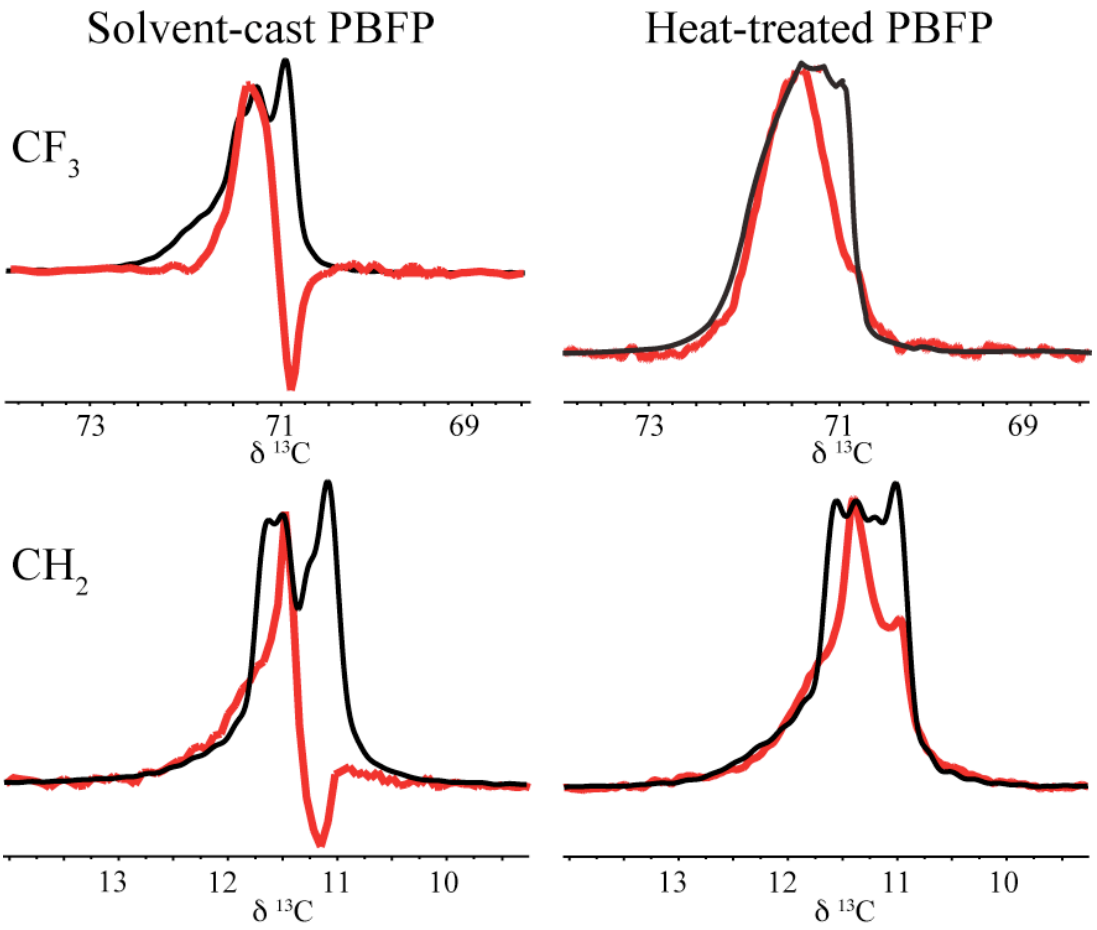

Figure 59 Expansions of the CF_3 and CH_2 signals in the 125 MHz $^{13}C\{^{1}H,^{19}F\}$ $^{19}F \rightarrow {}^{13}C$ (top) and $^{1}H \rightarrow {}^{13}C$ (bottom) CP DIVAM NMR spectra of solvent-cast and heat-treated (shown in red). MAS rate 25 kHz. The respective signals from $^{13}C\{^{1}H,^{19}F\}$ MAS NMR spectra are shown in black for comparison.

Observation of both CF_3 and CH_2 signals suggest that line 1 has the highest mobility, as it inverts at the same mini-pulse angle as the corresponding amorphous components in the ^{19}F and ^{1}H DIVAM nutation arrays.

Total crystallinity, as determined by the area under the crystalline peaks, increases upon heat-treatment, from 76.4% to 89.1% in the CF_3 signal and from 69.1% to 82.2% in the CH_2 signal. This is consistent with conclusions drawn on ^{1}H, ^{19}F and ^{31}P spectra, where solvent-cast PBFP is predominantly crystalline, and the crystallinity is seen to further increase upon thermal treatment.

In conclusion, ^{1}H, ^{19}F, ^{31}P and ^{13}C one-dimensional MAS NMR experiments proved to be capable of distinguishing between different environments within poly[*bis*(trifluoroethoxy)phosphazene]. In all spectra presented, signals were deconvolved into several narrow and broad contributions. The narrow contributions were found to correspond to the amorphous domain and mesophases within the polymer as they all exhibited similar nutation in the DIVAM experiments. This suggests the presence of liquid crystalline phases at ambient temperature. Correspondingly, the broad components in the spectra of the solvent-cast PBFP were assigned to the spherulitic formations of the crystalline lamellae within the polymer consisting of the β-monoclinic and α-orthorhombic crystal units. Also worth mentioning is the difference between the signals in the ^{1}H and ^{13}C, and the ^{19}F and ^{31}P MAS spectra, where the latter only contain three separate lines each. This inconsistency can be explained, on one hand, by the insensitivity of fluorine nuclei to their immediate environment due to high mobility occurring along the C–CF_3 bond in the side-chain, and on the other hand, by the strong

coupling between phosphorous and nitrogen-14, which cannot be effectively removed at this time.

Furthermore, the changes observed in the spectra of PBFP upon heat-treatment indicate that the crystalline region converts to the γ-orthorhombic form characterized by larger unit cell dimensions, and as a result the overall crystallinity is increased. Intensities, widths and areas of separate lines contributing to the signals were extracted using deconvolution analyses, from which it became possible to determine the quantitative information about the distribution between the crystalline and the amorphous regions within the polymer. On the whole, the observed behavior is consistent with the existing model of the morphology of PBFP.

3.6 $^{1}H\{^{19}F\}$, $^{19}F\{^{1}H\}$, $^{31}P\{^{1}H,^{19}F\}$ and $^{13}C\{^{1}H,^{19}F\}$ MAS NMR of batch 1 and batch 2 PBFP and their respective heat-treated samples

As mentioned earlier, variations in certain steps of preparation of PBFP are expected to affect crystalline/amorphous composition of the resulting polymer. According to the discussion in 1.2.4, prolonged reaction times upon substitution, produce materials with larger amount of crystalline environments. This notion is used as the basis for comparison of solvent-cast batch 1 (SCB1) and solvent-cast batch 2 (SCB2) PBFP, where their solutions were stirred for 8 and 24 hours, respectively. In order to retain consistency with the interpretations of the spectra of SC and HT and provide reliable information, the chemical shifts, widths and Lorentzian/Gaussian fractions of the individual lines in deconvolution analyses are consistent between the two samples, and only changes in intensities are allowed.

3.6.1 One-dimensional $^{1}H\{^{19}F\}$ MAS NMR

Figure 60 shows the proton spectra of batch 1 and batch 2 PBFP, which contain a relatively narrow signal at about 4.69 ppm and a less intense broad peak at 7.2 ppm. In order to be consistent with deconvolution analyses of the ^{1}H spectra of SC and HT, signals are expected to contain the same number of contributions from the crystalline and amorphous domains in the polymer, with similar chemical shifts, widths and Gaussian/Lorentzian fractions. Accordingly, the signals are deconvolved into five lines, as seen in figure 60 and tabulated in Table 6.

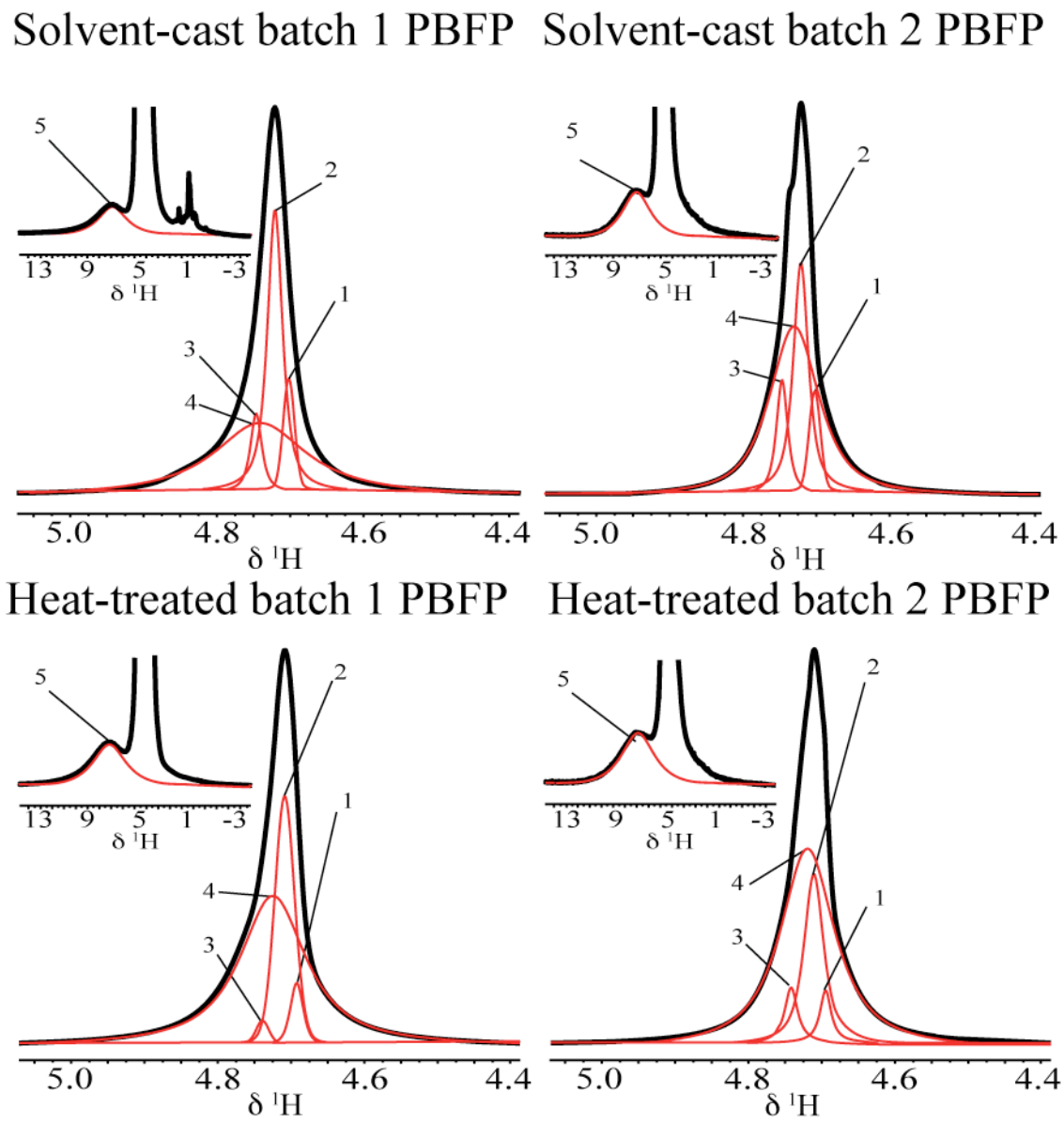

Figure 60 500 MHz $^{1}H\{^{19}F\}$ MAS NMR spectra of solvent-cast batch 1, solvent-cast batch 2, heat-treated batch 1 and heat-treated batch 2 PBFP. MAS rate 25 kHz.

Lorentzian lines 1 through 3 are relatively narrow and therefore are assigned to mobile environments, whilst the remaining mostly Gaussian lines 4 and 5 are much broader and thus would correspond to the crystalline domain. The aforementioned differences in the preparation are expected to increase the overall crystallinity of PBFP, which indeed is the case, where one can readily appreciate significantly higher intensities

of the crystalline peaks 4 and 5 in the spectrum of SCB2, reflecting higher overall crystallinity of batch 2 PBFP.

Spectra of heat-treated batch 1 (HTB1) and batch 2 (HTB2) PBFP exhibit similar composition, where deconvolution results tabulated in table 6 suggest changes in the distribution of relative peak intensities. Such, crystalline components 4 and 5 are seen to increase upon heat-treatment, whilst lines 1 through 3 decrease, which confirms their assignment to mobile environments. Similar to the observations on the ^{1}H MAS NMR spectrum of solvent-cast PBFP, peaks due to trace impurities emerge in the spectrum of SCB1 at about 1.5 ppm, and subsequently disappear upon heat-treatment.

Table 6 Peak parameters in the $^{1}H\{^{19}F\}$ MAS NMR spectra of solvent-cast batch 1, solvent-cast batch 2, heat-treated batch 1 and heat-treated batch 2 PBFP.

Peak #	**1**	**2**	**3**	**4**	**5**	**1**	**2**	**3**	**4**	**5**
Sample			SCB1					SCB2		
Chemical shift (ppm)	4.69	4.70	4.72	4.73	7.20	4.69	4.70	4.72	4.73	7.20
Normalized intensity†	0.30	0.73	0.21	0.18	0.10	0.25	0.57	0.28	0.43	0.19
Width (Hz)	11.1	23.8	21.9	215	478	12.4	21.8	17.8	214	480
Area (%)	6.72	30.4	8.71	47.6	6.57	4.88	15.8	9.41	63.1	6.81
			HTB1					HTB2		
Chemical shift (ppm)	4.69	4.70	4.72	4.73	7.20	4.69	4.70	4.72	4.73	7.20
Normalized intensity†	0.14	0.61	0.04	0.28	0.18	0.14	0.42	0.14	0.49	0.22
Width (Hz)	11.1	23.8	21.9	215	478	12.4	21.8	17.8	216	480
Area (%)	2.77	18.9	3.05	61.88	13.4	1.39	6.34	3.38	79.5	9.39

† Intensities normalized on the basis of the maximum intensity of the respective signal

3.6.2 One-dimensional $^{19}F\{^{1}H\}$ MAS NMR

One-dimensional ^{19}F proton-decoupled MAS NMR spectra of SCB1 and SCB2 contain a main peak near –77 ppm. The lack of detailed structural information complicates deconvolution analyses and makes them less reliable; however, it can be suggested that three components are present in each signal, as seen in figure 61, top.

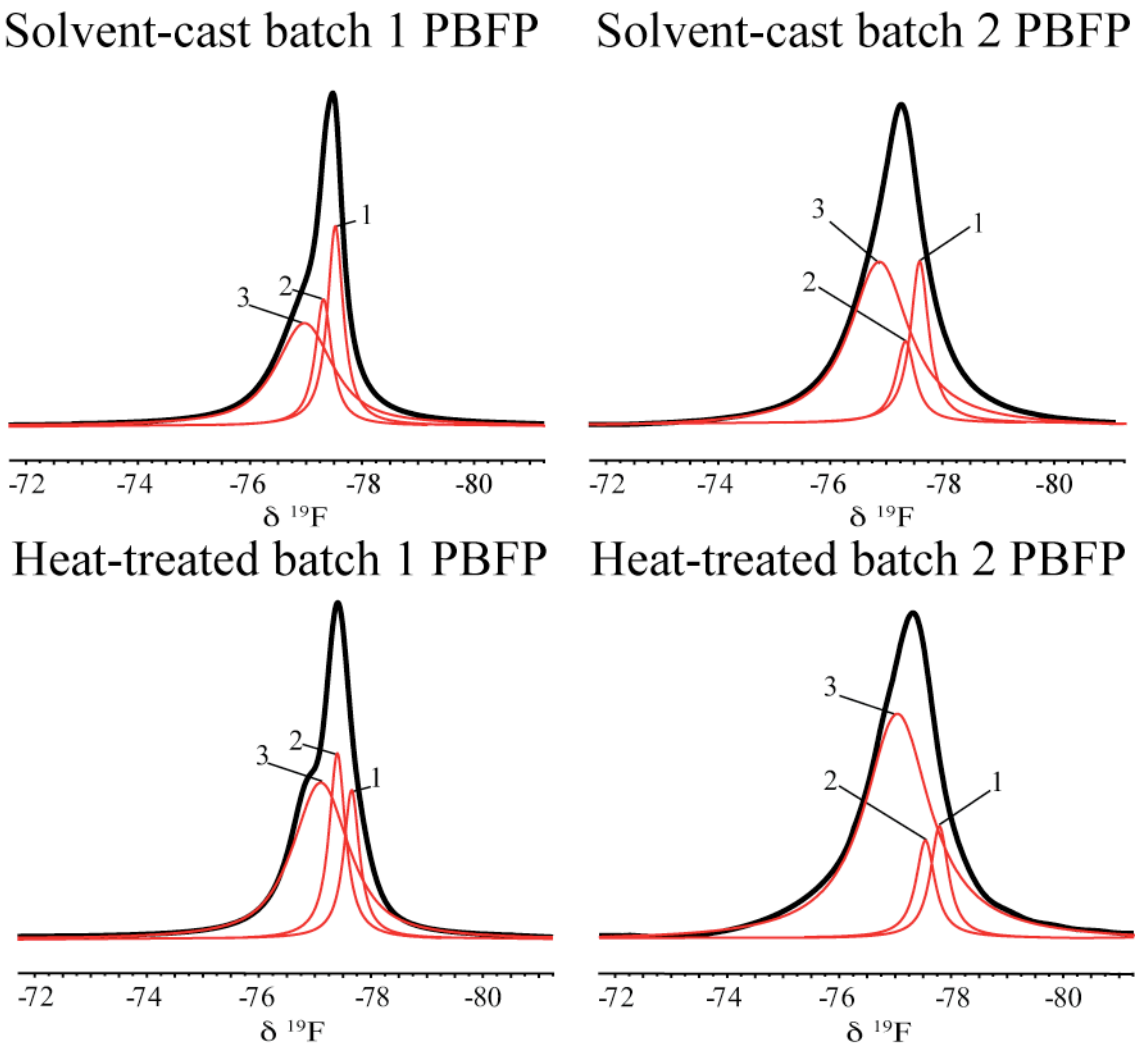

Figure 61 469 MHz $^{19}F\{^{1}H\}$ MAS NMR spectra of solvent-cast batch 1, solvent-cast batch 2, heat-treated batch 1 and heat-treated batch 2 PBFP. MAS rate 25 kHz.

In order ensure consistency and reliability of the results, the same deconvolution model was employed as in the ^{19}F spectra of the original SC and HT. Upon side-by-side comparison of the two signals, shown in figure 61, bottom, one can readily appreciate higher intensities of lines 1 and 2 in SCB1. Their narrow Lorentzian character can be used as a basis of their assignment to the mobile phases of the polymer; however, the behavior of this peak upon heat-treatment also needs to be considered. The Gaussian shaped peak, 3, is broad and therefore must correspond to the crystalline phases of PBFP, and its higher intensity in SCB2 in turn confirms higher crystallinity of that sample. The observed changes upon the heat-treatment are consistent between HTB1 and HTB2, where peak 1 decreases and therefore must correspond to the amorphous domain of PBFP. On the other hand, lines 2 and 3 become more intense, which verifies the assignment of peak 3 to the crystalline phases and also suggests that peak 2 likely corresponds to the mesophase. Peak parameters are tabulated in Table 7.

Table 7 Peak parameters in the $^{19}F\{^{1}H\}$ MAS NMR spectra of solvent-cast batch 1, solvent-cast batch 2, heat-treated batch 1 and heat-treated batch 2 PBFP.

Peak #	**1**	**2**	**3**	**1**	**2**	**3**
Sample		SCB1			SCB2	
Chemical shift (ppm)	–77.6	–77.2	–76.8	–77.6	–77.2	–76.8
Normalized intensity[†]	0.61	0.37	0.30	0.51	0.24	0.49
Width (Hz)	31.0	42.0	176	32.0	39.0	176
Area (%)	27.1	15.1	57.8	26.8	7.3	65.9
		HTB1			HTB2	
Chemical shift (ppm)	–77.6	–77.2	–76.8	–77.6	–77.2	–76.8
Normalized intensity[†]	0.43	0.54	0.46	34.9	29.4	68.9
Width (Hz)	31.0	42.0	176	32.0	39.0	176
Area (%)	11.7	9.60	78.7	10.9	5.90	83.2

[†] Intensities normalized on the basis of the maximum intensity of the respective signal

3.6.3 One-dimensional $^{31}P\{^{1}H, ^{19}F\}$ MAS NMR

The $^{31}P\{^{1}H, ^{19}F\}$ MAS NMR spectra of SCB1 and SCB2 contain a main peak near –7.5 ppm that has a slightly different appearance than in the spectra of solvent-cast and heat-treated PBFP. Signals were deconvolved into three contributions as seen in figure 62, top, and tabulated in Table 8.

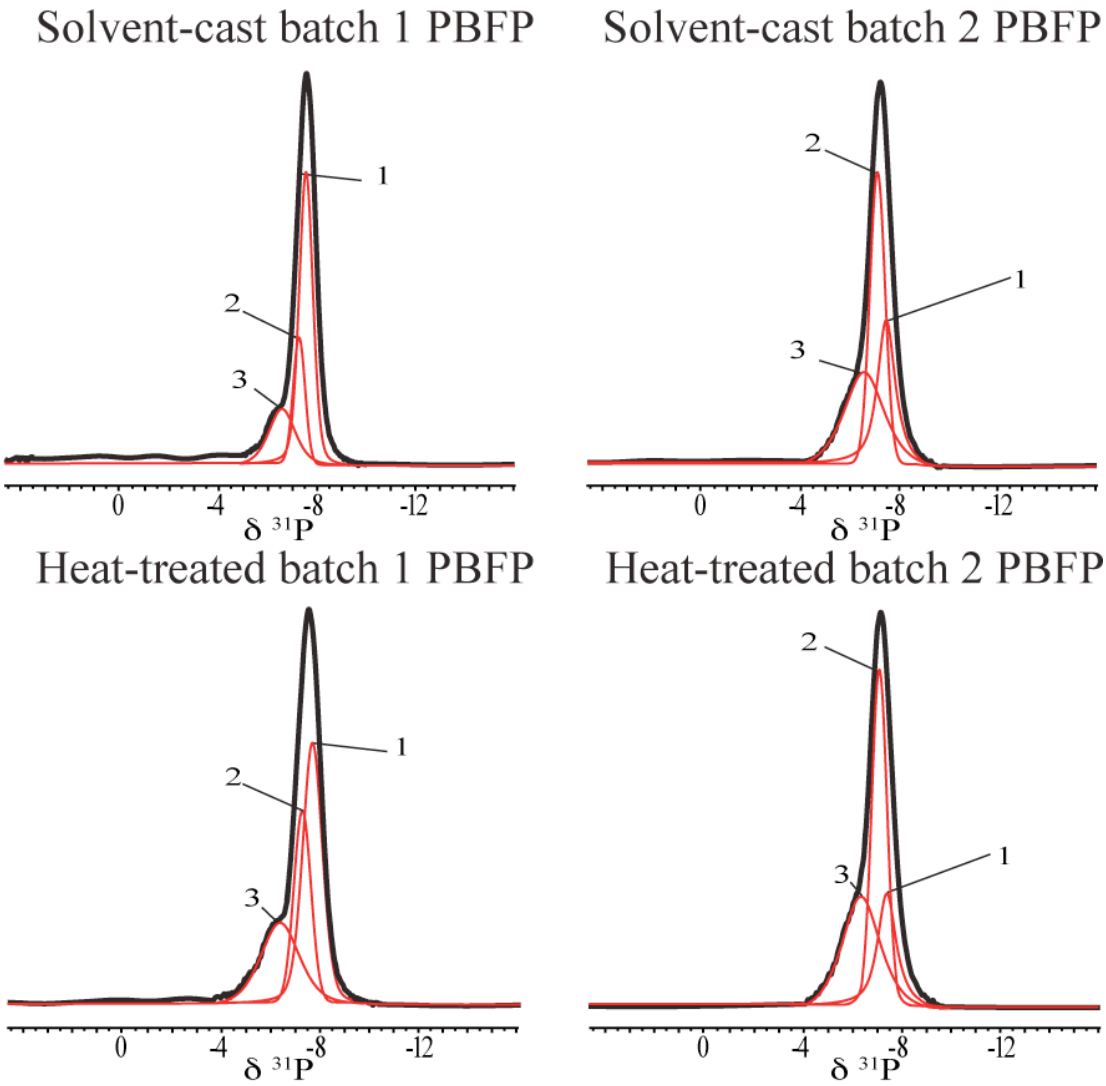

Figure 62 202 MHz $^{31}P\{^{1}H,^{19}F\}$ MAS NMR spectra of solvent-cast batch 1, solvent-cast batch 2, heat-treated batch 1 and heat-treated batch 2 PBFP. MAS rate 25 kHz.

Recall that in the ^{31}P spectra of SC and HT, peak 3 appeared at –3.5 ppm; however, it is not observed in the spectra of SCB1 and SCB2; however, a new Gaussian and broad peak arising near –6.5 ppm, resembles that in the spectra of SC and HT and hence is assigned to the crystalline environments within the polymer. This major departure is not well understood at this moment, although this significant difference in chemical shift of the crystalline signal is likely caused by the variations in the local macromolecular environments and the chain conformations. This behavior could be due to the branching and cross-linking between the polymer chains, and therefore it will be further explored in future studies. From the deconvolution analyses it follows that the ratio between the crystalline peak 3 and the amorphous peak 1 in the spectrum of SCB2 is greater when compared to SCB1, which indicates that the longer reaction times of the nucleophilic substitution, used for the second preparation of PBFP, increases an overall crystallinity. On the other hand, narrow peak 2 is more intense in SCB2, from which it can be inferred that it corresponds to the liquid crystalline regions within the polymer.

Heat-treatment of both preparations of PBFP results in the reduced intensity of the amorphous peak 1, as seen in figure 62, bottom. Correspondingly, peaks 2 and 3 are seen to increase in the spectra of HTB1 and HTB2, which is consistent with their assignment to the mesophase and the crystalline regions, respectively.

Table 8 Peak parameters in the $^{31}P\{^{1}H,^{19}F\}$ MAS NMR spectra of solvent-cast batch 1, solvent-cast batch 2, heat-treated batch 1 and heat-treated batch 2 PBFP.

Peak #	**1**	**2**	**3**	**1**	**2**	**3**
Sample		SCB1			SCB2	
Chemical shift (ppm)	–7.51	–7.11	–6.52	–7.51	–7.11	–6.52
Normalized intensity†	0.75	0.33	0.15	0.38	0.76	0.24
Width (Hz)	149	123	341	149	123	342
Area (%)	38.8	16.4	44.8	13.6	27.5	58.9
		HTB1			HTB2	
Chemical shift (ppm)	–7.51	–7.11	–6.52	–7.51	–7.11	–6.52
Normalized intensity†	0.65	0.48	0.21	0.27	0.83	0.26
Width (Hz)	149	123	341	149	123	342
Area (%)	23.1	23.8	53.1	6.50	30.7	62.8

† Intensities normalized on the basis of the maximum intensity of the respective signal

3.6.4 One-dimensional $^{13}C\{^{1}H,^{19}F\}$ MAS NMR

$^{13}C\{^{1}H,^{19}F\}$ MAS NMR spectra of SCB1 and SCB2 were obtained using high-power simultaneous XY-16 double decoupling at a MAS rate of 25 kHz. Signals from CF_3 and CH_2 carbons exhibit complex structures which are somewhat similar to those in the spectra of solvent-cast and heat-treated PBFP. Correspondingly, the deconvolution model from previous experiments was applied to the CF_3 and CH_2 signals, revealing six and five contributions to the signals, respectively. The results of the deconvolution analyses of the spectra of SCB1 and SCB2 are shown in figure 63 and Table 9.

One can readily appreciate significantly different distributions between the line intensities in the CF_3 signal of SCB1 and SCB2 (figure 63, top). Narrow lines 1, 2 and 5 are more intense in SCB1, whilst narrow lines 3, 4 and broad line 6 are seen to increase in SCB2. This is consistent with the CH_2 signal, shown also in figure 63, where component 1 and 2 are increased in SCB1, and the remaining lines 3 through 5 are more intense in SCB2. This distribution was preserved upon heat-treatment, where relative changes in line intensities are consistent, as seen in figure 63. In the CF_3 signals of both heat-treated preparations of PBFP, lines 1, 4 and 5 decrease, and lines 2, 3 and 6 become more intense. The same behavior is observed in the CH_2 signals, with lines 1 and 4 becoming less intense and lines 2, 3 and 5 increasing upon heat-treatment. This allows for the assignment of the components seen in SCB1 and SCB2 to the various domains within PBFP. As such, narrow lines 1 and 5 in the CF_3 signals correspond to the amorphous domain of the polymer, as they are initially less intense in the more crystalline batch 2 PBFP and further decrease upon heat-treatment. Correspondingly, the remaining narrow components must represent the mesophase environments within the polymer, as they

become more intense upon heat-treatment. Finally, the broad line, 6, can be unmistakably assigned to the crystalline domain of the polymer, as it is initially higher in SCB2, and proportionally increases in both heat-treated samples. Similar principles are employed for the peak assignment in the CH_2 signals. As a result, line 1 corresponds to the amorphous domain, lines 2 through 4 to mesophase, and line 5 to the crystalline region of PBFP.

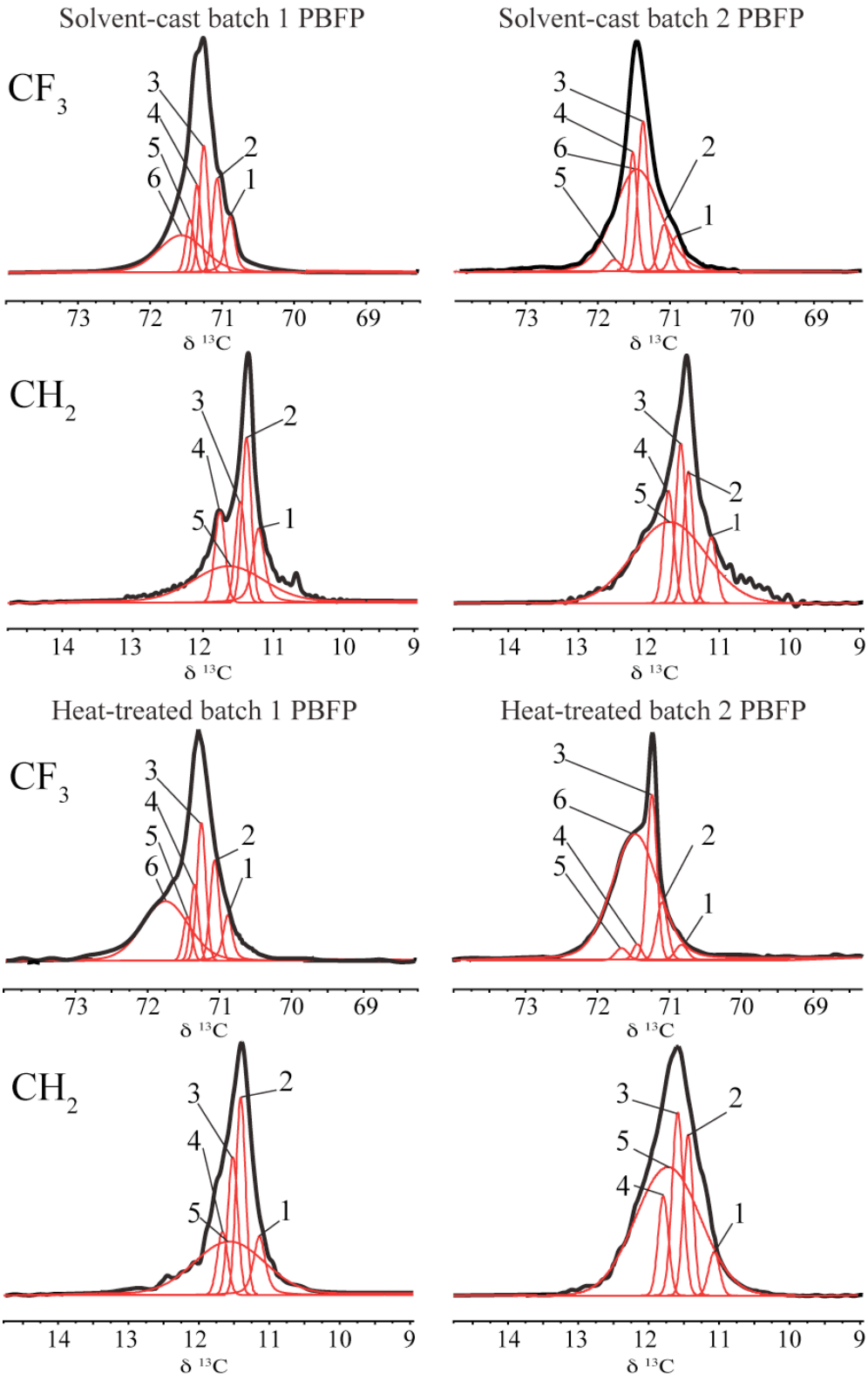

Figure 63 Expansions of the CF_3 and CH_2 signals in the 125 MHz $^{13}C\{^1H,^{19}F\}$ MAS NMR spectra of solvent-cast batch 1, solvent-cast batch 2, heat-treated batch 1 and heat-treated batch 2 PBFP. MAS rate 25 kHz.

Table 9 Peak parameters in the $^{13}C\{^{1}H,^{19}F\}$ MAS NMR spectra of SCB1, SCB2, HTB1 and HTB2 PBFP.

Peak #	**1**	**2**	**3**	**4**	**5**	**6**	**1**	**2**	**3**	**4**	**5**	**6**
Sample	SCB1						SCB2					
						CF_3						
Chemical shift (ppm)	70.89	71.04	71.38	71.26	71.58	71.62	70.91	71.13	71.31	71.55	71.69	71.49
Normalized intensity†	0.32	0.44	0.53	0.42	0.29	0.14	0.13	0.16	0.67	0.61	0.08	0.50
Width (Hz)	30.5	30.5	28.8	29.2	28.9	124	31.8	30.1	30.7	30.1	28.9	135
Area (%)	15.6	17.8	20.1	17.1	13.2	16.2	6.21	7.17	22.5	22.1	5.34	36.7
						CH_2						
Chemical shift (ppm)	11.01	11.22	11.45	11.67	11.57		11.01	11.22	11.45	11.66	11.56	
Normalized intensity†	0.26	0.81	0.48	0.45	0.14		0.25	0.73	0.83	0.68	0.40	
Width (Hz)	28.7	28.5	27.8	26.1	194		29.1	28.1	27.4	27.6	195	
Area (%)	10.1	28.2	18.6	18.1	25.0		9.09	18.6	19.8	17.1	35.4	
	HTB1						HTB2					
						CF_3						
Chemical shift (ppm)	70.89	71.04	71.38	71.26	71.58	71.75	70.91	71.13	71.31	71.55	71.69	71.69
Normalized intensity†	0.18	0.51	0.69	0.46	0.17	0.39	0.08	0.19	0.82	0.08	0.08	0.75
Width (Hz)	30.5	30.5	28.8	29.2	28.9	124	31.8	30.1	30.7	30.1	28.9	135
Area (%)	11.4	18.3	22.6	17.4	9.81	20.5	5.90	8.43	23.8	5.78	5.56	50.6
						CH_2						
Chemical shift (ppm)	11.01	11.22	11.45	11.67	11.57		11.01	11.22	11.45	11.66	11.56	
Normalized intensity†	0.20	0.92	0.74	0.22	0.19		0.18	0.72	0.76	0.40	0.59	
Width (Hz)	28.7	28.5	27.8	26.1	194		29.1	28.1	27.4	27.6	195	
Area (%)	9.76	29.6	22.4	8.56	29.7		9.15	18.1	18.4	10.3	44.1	

† Intensities normalized on the basis of the maximum intensity of the respective signal

In summary, observations on the ^{1}H, ^{19}F, ^{31}P and ^{13}C MAS NMR spectra of batch 1 and batch 2 PBFP are consistent with the conclusions drawn on solvent-cast and heat-treated PBFP discussed in the previous section. The results of the deconvolution analyses suggest there are significant differences between the two preparations of PBFP. As increasing reaction time of the nucleophilic substitution of the high molecular weight poly(dichlorophosphazene) results in increased crystallinity of the product, correspondingly the intensity of the broad component in the spectrum of batch 2, which is assigned to the crystalline region, was found to be greater than in batch 1. Heat-treatment of both samples exhibited increased area of the crystalline signal, presumably due to the formation of γ-orthorhombic crystal structures. Accordingly, the differences between narrow components were also observed in the ^{13}C MAS NMR spectra of SCB1 and SCB2; however, changes in their contributions were not uniform between the two preparations and upon heat-treatment. Differences between contributions from a few narrow components indicate that some mesophases are more predisposed to crystallizing.

In general, the results presented hereby are consistent with the existing morphological model of PBFP[308] and support the interpretations of the spectra of SC and HT PBFP.

3.7 ^{1}H, ^{19}F, ^{31}P and ^{13}C MAS NMR of PBFP obtained via the living cationic polymerization at ambient temperature

Poly[*bis*(trifluoroethoxy)phosphazene] was synthesized via the ambient temperature living cationic polymerization (AT), as described in 2.2.3. This substantially different approach to obtaining phosphazene polymers is expected to cause changes in morphology of the polymer and hence should alter the appearance of ^{1}H, ^{19}F, ^{31}P and ^{13}C MAS NMR spectra. Indeed, all spectra of AT PBFP, collected under identical experimental conditions to the previously discussed SC, HT, SCB1, SCB2, HTB1 and HTB2, are very different in appearance, as shown in what follows.

3.7.1 One-dimensional $^{1}H\{^{19}F\}$, $^{19}F\{^{1}H\}$, $^{31}P\{^{1}H, ^{19}F\}$ MAS NMR

The $^{1}H\{^{19}F\}$ MAS NMR spectrum of AT shows a major signal near 4.7 ppm, which was subsequently deconvolved into four components, as seen in the right hand side of figure 64. The narrow lines, 1 through 3, are predominant whilst the broad line, 4, has much lower intensity. Based upon the deconvolution model used previously for ^{1}H signals it can be inferred that the narrow components correspond to the mobile regions of PBFP, possibly either a disordered amorphous phase or partially ordered mesophase, or both. This leads to an assignment of the remaining broad line, 4, to the crystalline phases. Peak parameters are tabulated in Table 10 and suggest that AT PBFP is less crystalline than previously studied samples. In addition, line 4 is narrower than determined previously, which could be the result of smaller sized and more mobile crystalline lamellae.

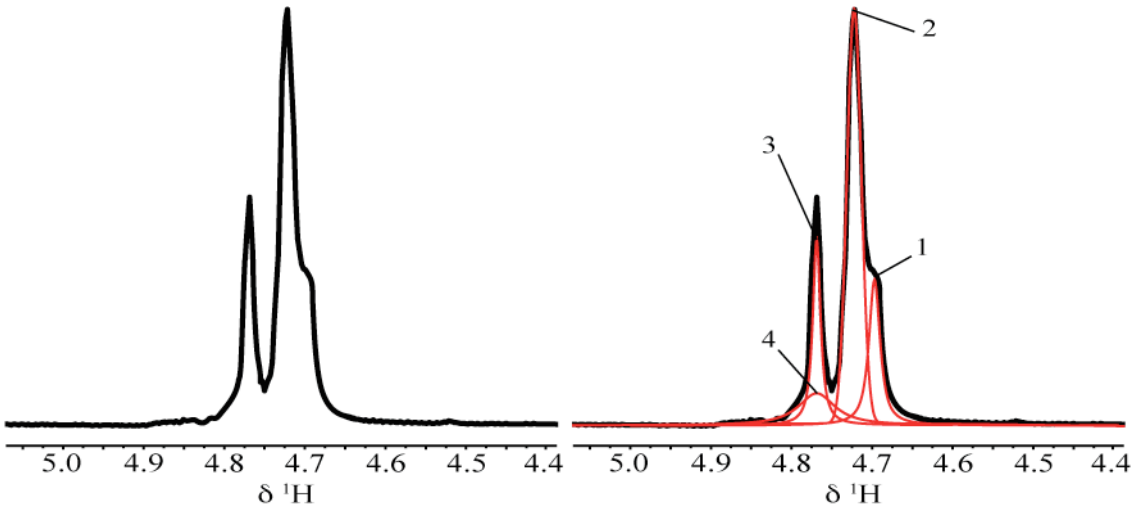

Figure 64 500 MHz $^{1}H\{^{19}F\}$ MAS NMR spectrum of AT PBFP. MAS rate 25 kHz

Table 10 Peak parameters in the $^{1}H\{^{19}F\}$ MAS NMR spectrum of AT PBFP.

Peak #	**1**	**2**	**3**	**4**
Chemical shift (ppm)	4.69	4.72	4.77	4.77
Normalized intensity†	0.37	1	0.46	0.09
Width (Hz)	15.8	21.3	16.7	122
Area (%)	23.9	43.4	27.2	5.5

† Intensities normalized on the basis of the maximum intensity of the respective signal

A signal in the $^{19}F\{^{1}H\}$ spectrum of AT PBFP is deconvolved into four contributions, all of which are narrow (figure 65, *vide supra*), where the crystalline signal is not observed. This can be explained by the low overall crystallinity of this preparation of PBFP and the high rotational motion of the CF_3 group along the C–C bond in the side-chain. As a result, increased mobility makes the broad crystalline signal elusive.

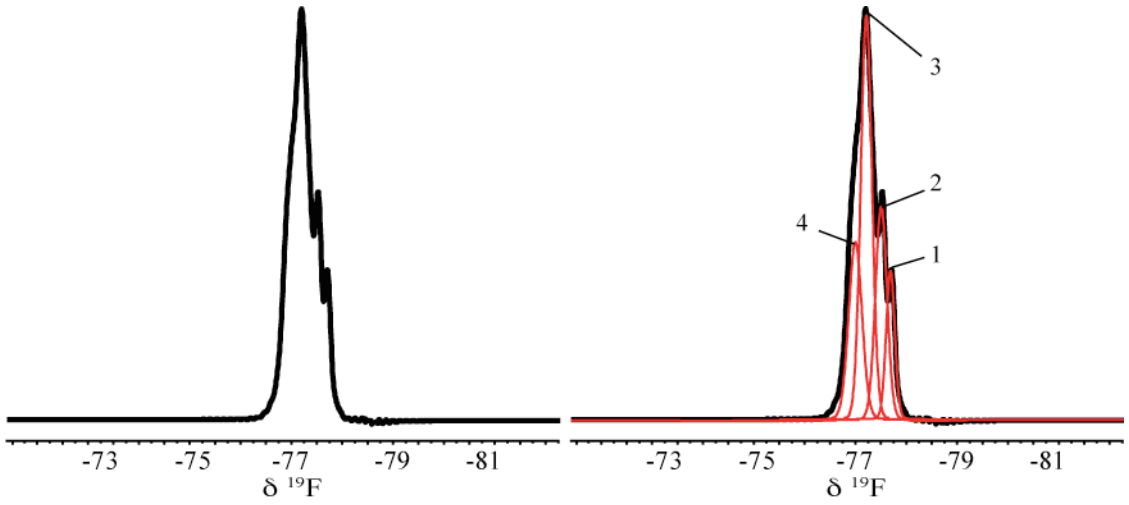

Figure 65 469 MHz $^{19}F\{^{1}H\}$ MAS NMR spectrum of AT PBFP. MAS rate 25 kHz.

Table 11 Peak parameters in the $^{19}F\{^{1}H\}$ MAS NMR spectrum of AT PBFP.

Peak #	**1**	**2**	**3**	**4**
Chemical shift (ppm)	–77.6	–77.4	–77.2	–76.9
Normalized intensity†	0.36	0.51	0.98	0.43
Width (Hz)	33	34	33	35
Area (%)	16.8	22.6	41.1	19.5

† Intensities normalized on the basis of the maximum intensity of the respective signal

The $^{31}P\{^{1}H, ^{19}F\}$ spectrum of AT PBFP is shown in figure 66. The signal emerging at about –7.5 ppm is deconvolved into 3 lines, of which the narrow component, 2, is the most intense. Line 3 is broad and hence corresponds to the crystalline region. Currently the origin of the two remaining components cannot be determined with any degree of confidence; however, their narrow character suggests that they correspond to either the amorphous domain, the mesophase region, or both.

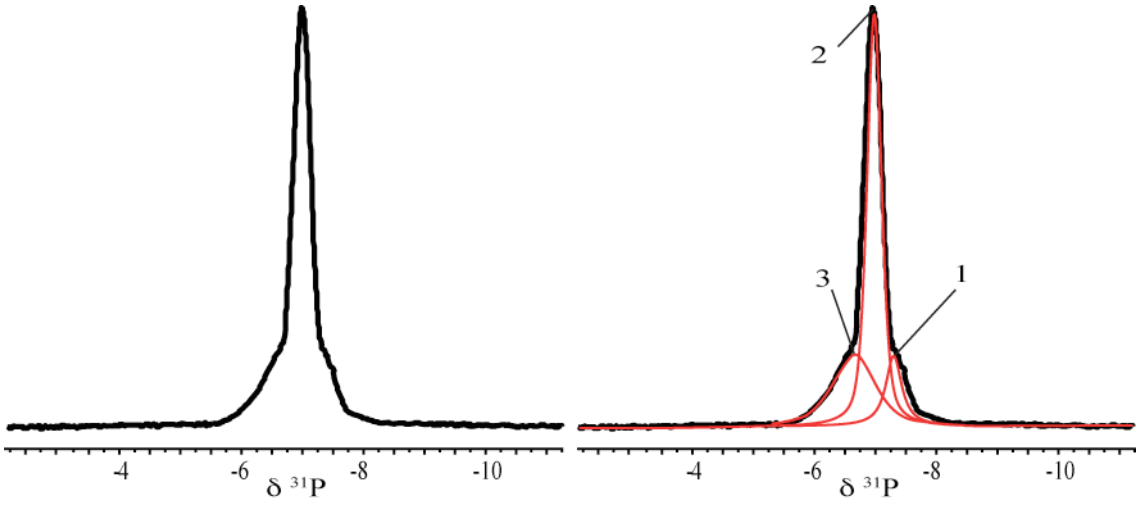

Figure 66 202 MHz $^{31}P\{^{1}H,^{19}F\}$ MAS NMR spectrum of AT PBFP. MAS rate 25 kHz.

Table 12 Peak parameters in the $^{31}P\{^{1}H,^{19}F\}$ MAS NMR spectrum of AT PBFP.

Peak #	**1**	**2**	**3**
Chemical shift (ppm)	–7.38	–6.99	–6.63
Normalized intensity†	0.17	0.98	0.17
Width (Hz)	177	133	412
Area (%)	14.2	57.8	28.0

† Intensities normalized on the basis of the maximum intensity of the respective signal

3.7.2 One-dimensional $^{13}C\{^{1}H, ^{19}F\}$ MAS NMR

By analogy with the spectra of solvent-cast, heat-treated, batch 1 and batch 2 PBFP, the $^{13}C\{^{1}H, ^{19}F\}$ spectrum of AT contains two signals with complex structures, at 11 and 71 ppm. Deconvolution analyses revealed five contributions to each signal, as shown in figure 67. Peak parameters are listed in table 13.

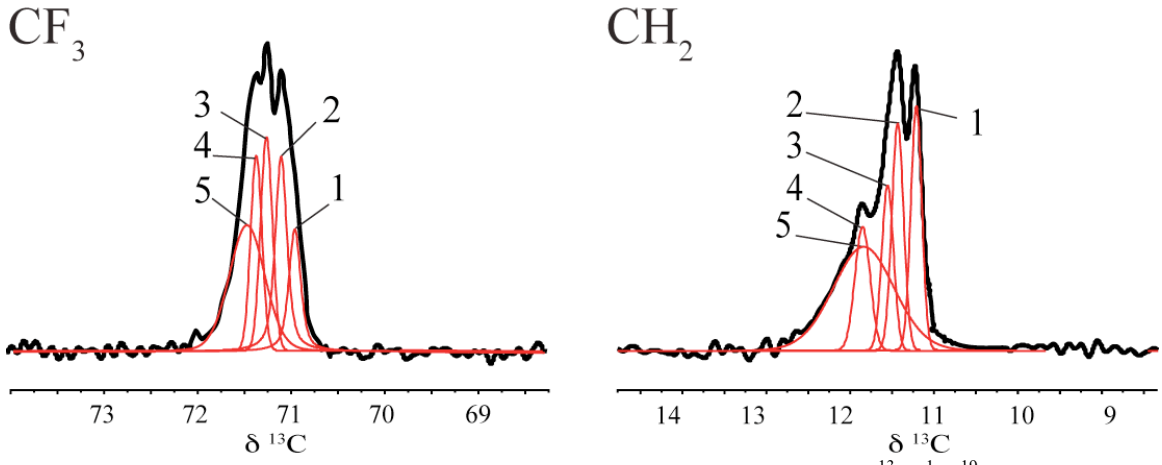

Figure 67 Expansions of the CF_3 and CH_2 signals in the 125 MHz $^{13}C\{^{1}H,^{19}F\}$ MAS NMR spectrum of AT PBFP. MAS rate 25 kHz.

One can readily appreciate the narrow Lorentzian character of lines 1 through 4, which therefore represent the distribution between the amorphous and the mesophase regions of the polymer. Correspondingly, component 5 is much broader and can be assigned to the various crystalline phases.

In summary, observations on the ^{1}H, ^{19}F, ^{31}P and ^{13}C MAS NMR spectra of PBFP obtained via living cationic polymerization at ambient temperature exhibit drastic differences when compared to the previously discussed preparations of PBFP. As such,

the ratio between the contributions from the narrow and the broad components to the signals in the MAS NMR spectra of AT, is considerably larger. As a result, it can be inferred that the preparation at ambient temperature does not lead to the formation of large crystalline regions within the polymer. This is consistent with the fact that this preparation is done at ambient temperature, and therefore there is not enough thermal energy to allow the polymer to reorganize into its crystalline forms.

Table 13 Peak parameters in the $^{13}C\{^{1}H,^{19}F\}$ MAS NMR spectrum of AT PBFP.

Signal	CF_3					CH_2				
Peak #	**1**	**2**	**3**	**4**	**5**	**1**	**2**	**3**	**4**	**5**
Chemical shift (ppm)	70.99	71.14	71.25	71.39	71.50	11.23	11.48	11.52	11.82	11.81
Normalized intensity†	0.42	0.65	0.71	0.65	0.43	0.81	0.76	0.56	0.42	0.36
Width (Hz)	29.5	30.1	29.8	29.9	122	31.1	31.5	29.7	29.9	121
Area (%)	12.6	18.8	21.4	18.5	28.7	22.1	20.9	15.2	14.1	27.7

† Intensities normalized on the basis of the maximum intensity of the respective signal

3.8 ^{31}P MAS NMR variable-temperature studies of solvent-cast PBFP

^{31}P direct polarization MAS NMR spectra of solvent-cast PBFP were acquired at temperatures from 21ºC to 150ºC to determine whether NMR can provide information about morphological transitions in the polymer upon heating.

In order to extract useful information about changes in the material upon heating, parameters such as peak area, intensity and linewidths have to be determined for spectra at all temperatures. This data was obtained through deconvolution analyses on each peak in the spectrum. This method is somewhat complicated due to non-uniqueness of the results, which in the case of variable temperature NMR becomes even more problematic. At high temperatures the NMR signal tends to decrease and the noise tends to increase; therefore, sensitivity decreases with temperature. When analyzing VT NMR spectra, this can obscure observations about changes in signals that are due to transfomations within the material. Therefore, only relative variations are considered accurate.

As shown previously, the phosphorous spectra of the solvent-cast PBFP at room temperature only contains two peaks, one of which is intense at –7.5 ppm and the other is significantly broader and smaller at –3.5 ppm. Current resolution limits any further observasion on the number of components present in the signal. At this stage, it can only be speculated that the peak at –7.5 ppm is composed of a single contribution, as opposed to being a complex signal containing several lines. In order to avoid ambiguity and inaccuracy, it will be assumed that phosphorous spectra of the solvent-cast PBFP at lower temperatures has only two peaks. At 90ºC and above, the signal at –7.5 ppm is seen to separate into two overlapping lines and thus it is possible to extract their individual parameters. This is demonstrated in figure 68, where the deconvolved ^{31}P spectra of the

solvent-cast PBFP at room temperature and 150ºC are shown side by side for comparison.

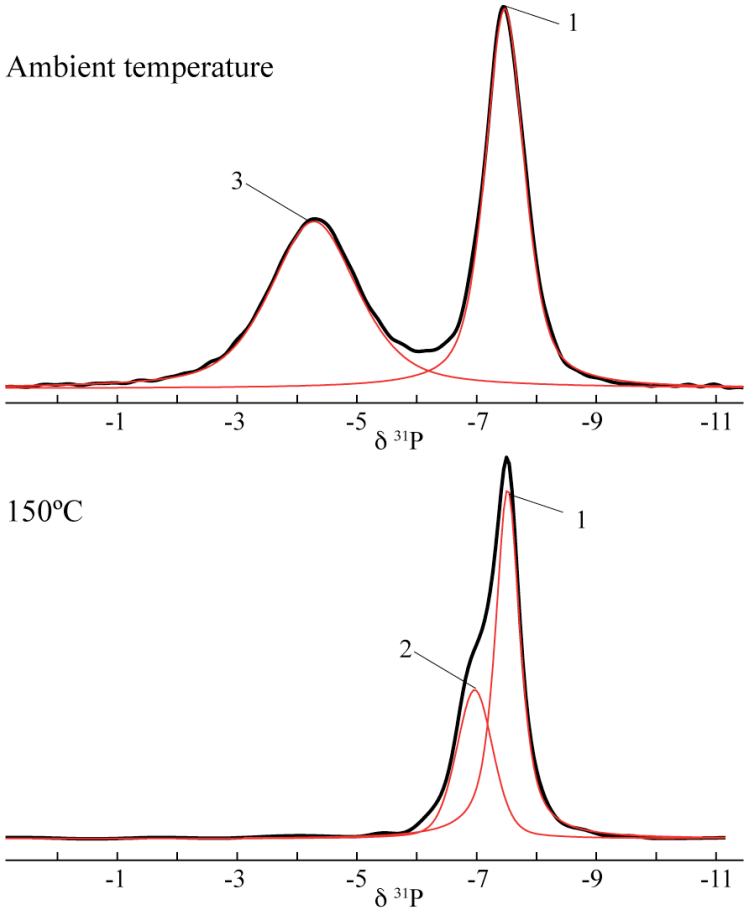

Figure 68 202 MHz $^{31}P\{^{1}H,^{19}F\}$ MAS NMR spectra of solvent-cast PBFP at ambient temperature and 150ºC. MAS rate 10 kHz.

Based on this working model, spectra at each temperature were subjected to deconvolution analysis. Normally the height and the width of a peak is sufficient to determine its area, nevertheless, in the spirit of completeness areas were recorded seperately. The Gaussian/Lorentizan fraction of the line shape is strongly influenced by the origin of the signal. As such, the inhomogeneity in the crystalline environments results in broadened lines that are predominatly Gaussian. In contrast, amorphous contributions are displayed as narrow intense peaks, that are mostly Lorentzian. These may change with temperature due to increased mobilities and, as a result, smaller Gaussian/Lorentzian fractions are observed.

In order to observe relative changes, raw data for all three parameters needs to be normalized. Intensities and linewidths were normalized based on their respective maximum values in the entire array of temperatures. The total sum of areas of the three peaks was used as the normalization factor for their respective values at each temperature. This data was used to construct plots of area, linewidth and intensity as a function of temperature, which are discussed below.

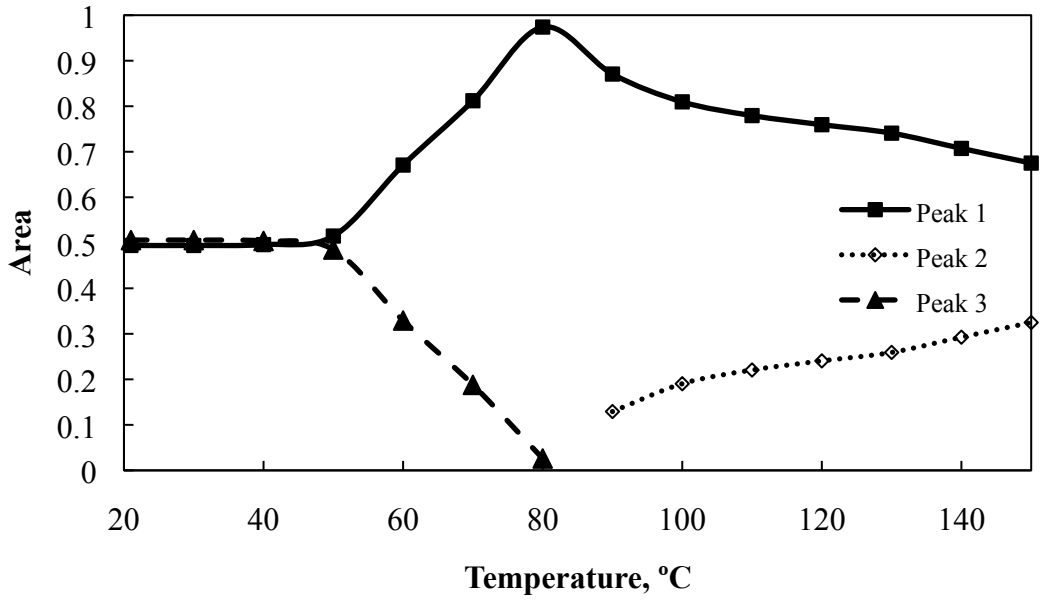

Figure 69 Normalized areas of the peaks in the $^{31}P\{^{1}H,^{19}F\}$ MAS NMR spectra of solvent-cast PBFP at variable temperatures, as determined by the deconvolution analyses. MAS rate 10 kHz

First, at temperatures from 21ºC to 50ºC, peaks 1 and 3 each account for 50% of the total area, then the ratio of peak 1/peak 3 starts to increase rapidly, nearly reaching 1 at 80ºC. At 90ºC, peak 3 completely diminishes and peak 2 starts to emerge, contributing ~15% to the total area. Upon further heating, the area of peak 1 becomes smaller, as that of peak 2 sees a two-fold increase, making up 30% of the total signal.

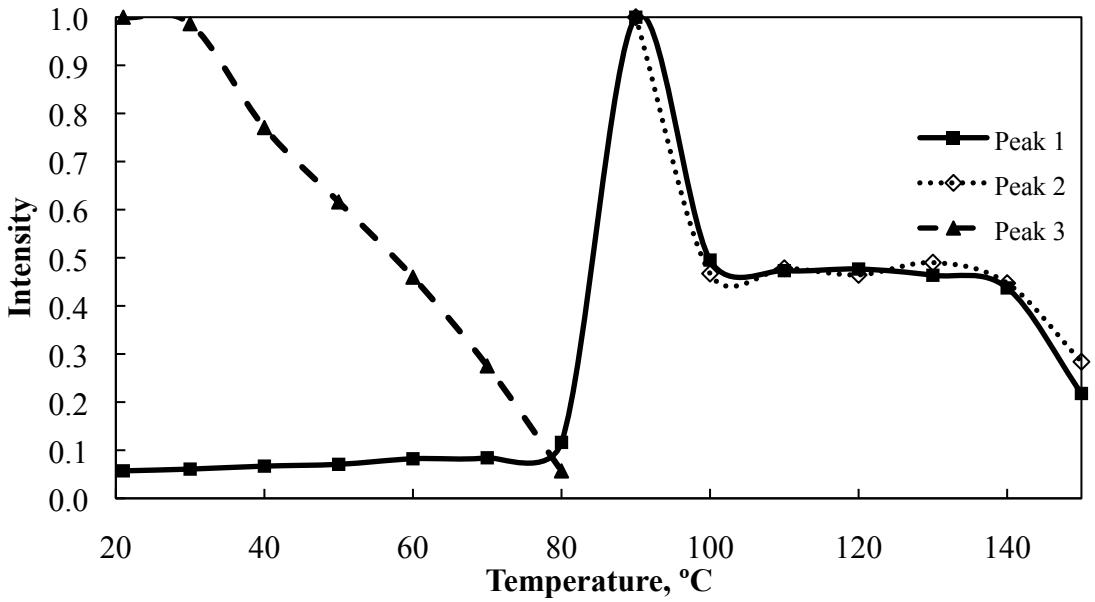

Figure 70 Normalized intensities of the peaks in the $^{31}P\{^{1}H,^{19}F\}$ MAS NMR spectra of solvent-cast PBFP at variable temperatures, as determined by the deconvolution analyses. MAS rate 10 kHz.

Curves of line intensities with temperature exhibit somewhat different behaviour. Line 1 increases by less than 5% over the range from room temperature to 90ºC. This slight deviation can be caused by errors in deconvolution, in which case one could say that line 1 does not experience any significant changes. In contrast peak 3 decreases rapidly over the same range, with intensity at 80ºC of only 5% of its maximum. It essentially disappears at temperatures above 90ºC, where peak 2 is seen to emerge. Peaks 1 and 2 reach their maximum intensities at 90ºC, and subsequently decrease by 50% after an additional 10 degree increase. Intensities reach a plateau from 100ºC to 140ºC, after which they see a further two-fold decrease at 150ºC. In this temperature regime the intensities of peaks 1 and 2 seem to change equally.

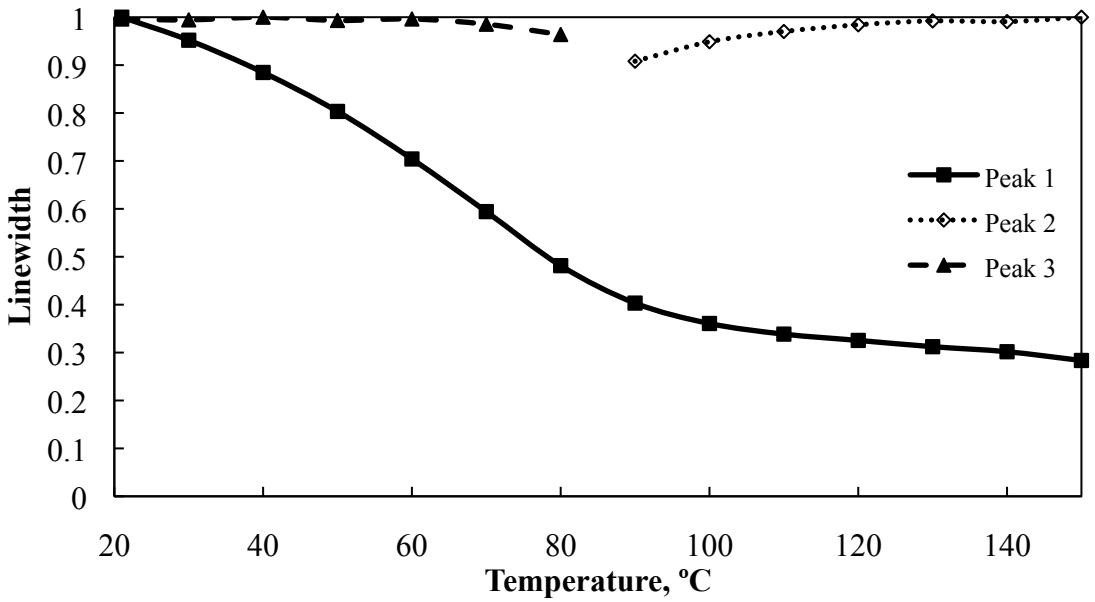

Figure 71 Normalized linewidths of the peaks in the $^{31}P\{^{1}H,^{19}F\}$ MAS NMR spectra of solvent-cast PBFP at variable temperatures, as determined by the deconvolution analyses. MAS rate 10 kHz.

Since the intensity of peak 1 experiences virtually no change up to 90ºC, it is obvious that any alteration in its area should be primarily governed by changes in its linewidth. Indeed, the width of peak 1 decreases by 70% over the entire temperature range to about 0.4 ppm (80 Hz) wide at 150ºC. In contrast, peak 3, is approximately 3 ppm wide (600 Hz), and remains unchanged from RT to 90ºC where it essentially disappears. Beyond this point, peak 2 emerges with linewidth roughly equal to that of peak 1 and increases upon further heating by 10%.

The results from the deconvoluiton analyses presented in terms of line area, intensity and width can be summarized as follows Over the temperature range from ambient to 80ºC, the intensity of peak 1 remains essentially unaffected, whilst that of peak 3 decreases by at least 95%. At the same time the linewidth of peak 1 declines in a linear fashion by a factor of two, and peak 3 is unchanged. For temperatures beyond 90ºC peak 3 vanishes completely, and peak 2 emerges. The linewidth of peak 2 is

roughly equal to that of peak 1 and is virtually unaffected by temperature. Note that the different behaviour exhibited by temperature dependence of the widths of peaks 1 and 2 suggests that they most likely originate from different environments from within the polymer. This notion; however, is not supported by the data from the intensities curve, where the lines are seen to have a similar rate of decrease. In theory, this could well be caused by the loss of sensitivity at high temperatures, as discussed previously. These facts should be sufficient to make preliminary conclusions about temperature behaviour of PBFP as monitored with ^{31}P MAS NMR.

Before any further discussion about peak assignments and interpretations of determinations of temperatures at which the polymer undergoes specific structural transformations, it would be helful to recall some basic concepts of the behaviour observed in different types of domains within the material. The amorphous domain is characterized by a high degree of disorder and is often accompanied by a high degree of mobility. Its respective NMR signal is expected to be narrow and as a result tends to have significant intensity. In theory, heating the polymer above T(1) should not significantly affect the appearance of the amorphous signal; however, multiple cycles of heating result in the increased crystallinity of PBFP below T(1). Therefore, the hypothetical signal from the amorphous domain should appear as a narrow intense line that does not experience severe changes upon temperature increase. However, it would be expected to experience lose intensity to the crystalline signal with heat cycling.

Out of three peaks found in the phosphorous spectrum, only peak 1 seems to match these criteria. Peak 3, on the other hand, most likely originates from the crystalline environment, as it has purely Gaussian character with a linewidth of 3 ppm which is

unaffected by heating and its intensity decreases with temperature. At ambient temperature the crystalline domain is highly rigid and has organized macromolecular packing and alignment, which imposes restrictions on moleucular motion resulting in significant linewidth broadening. These crystalline regions are bound to adjacent macromolecules in the amorphous environment in a random fashion. When exposed to higher temperatures major changes in polymer morphology can occur, as inevitably increased thermal motion allows the macromolecules to take on different arrangements, resulting in a significant degree of reorientation within the crystalline domain accompanied by the increased mobility. As a consequence, these polymer chains are not expected to contribute to the same broad crystalline signal. According to the data above, peak 3 vanishes at 90ºC, which falls within the transition temperature range of this polymer determined by DSC. At temperatures above T(1), crystalline phases are transformed into the liquid crystalline chain extended form, as explained previously in the phase diagram. As a result of this transformation from the crystalline to the liquid chrystalline phase the appearance of NMR spectra at higher temperatures is expected to be altered. It can therefore be assumed that peak 3 corresponds to the crystalline domain of PBFP, and that peak 2 is likely to correspond to the liquid crystalline phase as it is not seen below T(1) and exhibits linewidth behaviour similar to that of peak 3 upon heating.

3.9 Spin-lattice relaxation in the rotating frame measurements on solvent-cast PBFP at variable temperatures

As mentioned in the introduction the spin-lattice relaxation time in the rotating frame, $T_{1\rho}$, is expected to vary between signals from components with different mobilities and depends on the timescale of the locking field. Phosphorous MAS NMR of solvent-cast PBFP was acquired over a temperature range from ambient to 130ºC, as seen in figure 72.

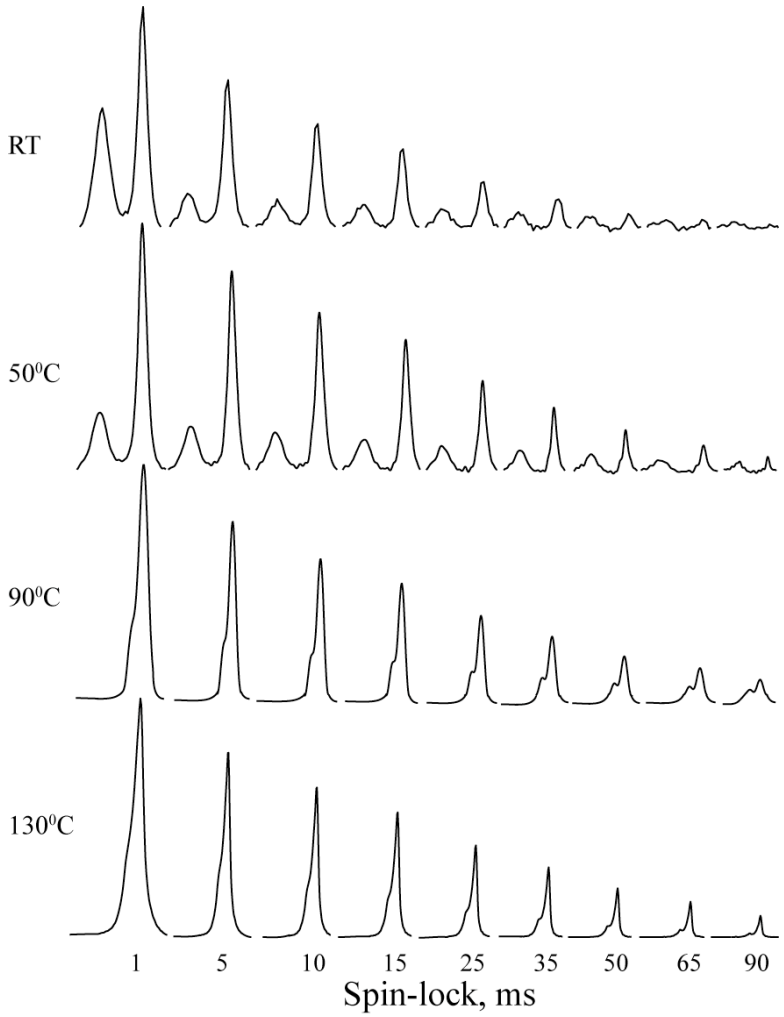

Figure 72 ^{31}P MAS NMR spectra in the $T_{1\rho}$ experiment on solvent-cast PBFP at variable temperatures.

The spectra are consistent with those obtained from the direct polarization VT experiments (*vide supra*). Two distinct signals are present at lower temperatures, with the loss of peak 3 and appearance of peak 2 at 90ºC. An array of 9 spin-lock times was used, ranging from 1 ms to 90 ms. In order to extract quantitative information about relaxation rates for each component, intensities of individual signals were extracted using deconvolution analyses. Raw peak intensity values are subsequently normalized based on the maximum intensity, from which spin-lock time dependence curves were constructed. For each peak, rates of decay were fit to an exponential decay function, in the following form: $f(t) = I \times e^{-\frac{t}{T_{1\rho}}}$; where I is the maximum initial intensity, t is value of spin-lock time along the x-axis and $T_{1\rho}$ is the relaxation constant. Simulation of an exponentially decaying line and adjustment of its parameters to achieve the best fit with the experimental curve allowed the calculation of the relaxation time for each peak. The curve for peak 1 intensity at ambient temperature as a function of lock time is shown below.

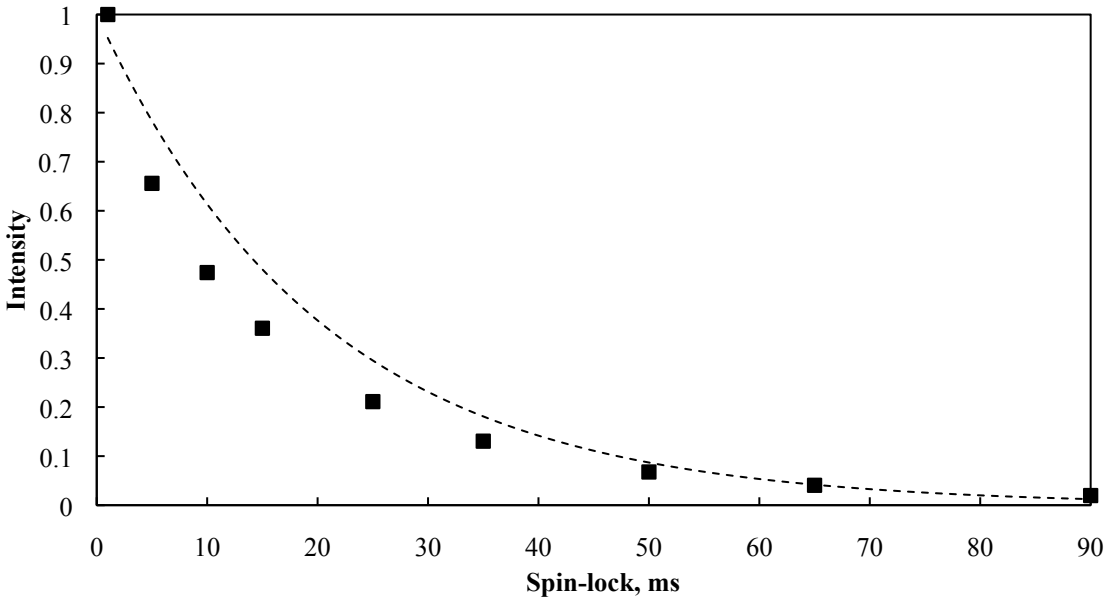

Figure 73 Intensity of peak 1 in the ^{31}P MAS NMR spectrum of solvent-cast PBFP at ambient temperature as a function of spin-lock time. Experimental decay denoted with square markers, dashed line indicates fitted simulated exponential decay.

In the example shown above, the following expression can be derived: $f(t) = e^{-\frac{t}{23.8}}$. This procedure was repeated for each observable peak in the spectrum for each temperature. Table 14 shows relaxation constants of the individual peaks at various temperatures. These values were plotted as functions of temperature as seen in figure 74.

Table 14 Spin-lattice relaxation rates in the rotating frame, $T_{1\rho}$, for the peaks in the ^{31}P VT MAS NMR spin-lock experiment on solvent-cast PBFP.

Temperature, °C	$T_{1\rho}$, ms		
	Line 1	Line 2	Line 3
21	23.8		64.5
30	26.3		60.6
40	29.1		56.5
50	32.3		51.5
60	37.9		47.2
70	38		42.6
80	37.5		39.2
90	37	36	
100	37	35.6	
110	37	35.5	
120	37	35.5	
130	37	35.7	

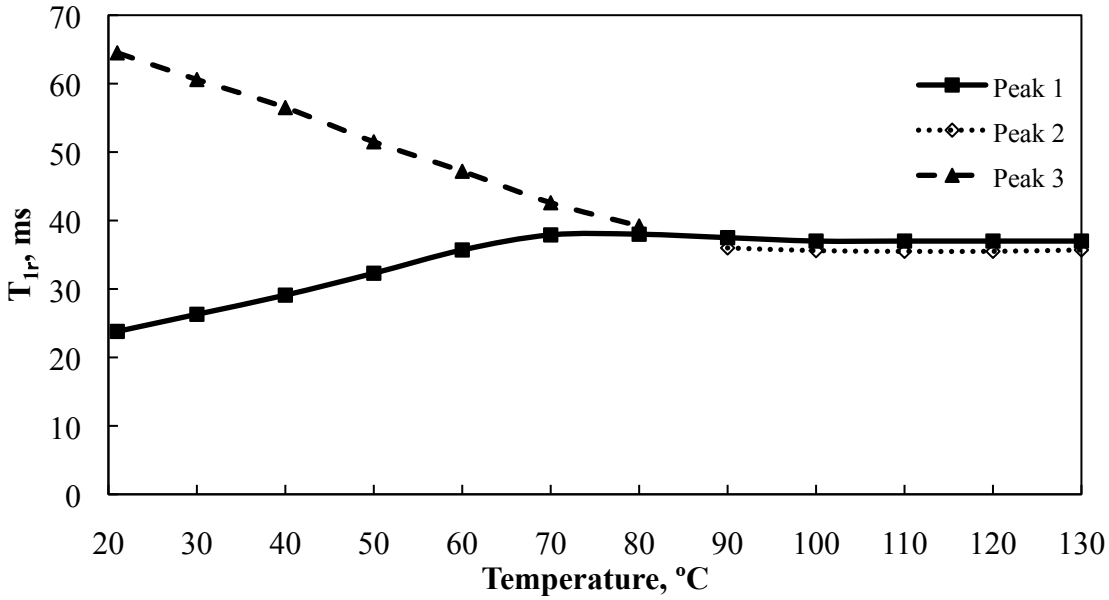

Figure 74 Spin-lattice relaxation rates in rotating frame, $T_{1\rho}$, as functions of temperature for the peaks in the ^{31}P VT MAS NMR spin-lock experiment on solvent-cast PBFP. MAS rate 10 kHz

The curve in figure 74 exhibits somewhat complex yet informative behavior. At room temperature the relaxation time constant of peak 1 is about 25 ms, which results in ~2.5 times faster recovery than that of peak 3. Upon further heating, this signal relaxes more slowly, where its $T_{1\rho}$ increases linearly to ~37 ms at 80ºC. This is accompanied by a decrease in the relaxation rate of peak 3 at roughly the same rate between ambient temperature and 80ºC. To conform with the data from the direct polarization phosphorous VT NMR experiments on the solvent-cast PBFP, where peak 3 disappears above 90ºC where peak 2 emerges, it seems that the relaxation rate of peak 2 takes over where that of peak 3 leaves off.

In order to interpret these results, it is crucial to take into account information discussed in the previous section of this chapter. It was hypothesized that peak 1 corresponds to the amorphous domain of the polymer whilst the crystalline portion is

represented by peak 3. The rigidity and restricted mobility of the crystalline environment must therefore result in much slower relaxation at room temperature, which is exhibited by peak 3. Its relaxation rate at ambient temperature is about 65 ms, which is significantly larger than that of peak 1, which is 25 ms. This two-fold difference indicates that there is a considerable difference in molecular motional regimes experienced. The graph in figure 74 suggests that this difference in $T_{1\rho}$ values decreases until they are roughly equal near 80ºC.

To explain this phenomenon, one has to assume that several complex processes take place at the same time. Recall the high-temperature behavior in the ^{31}P MAS NMR of the solvent-cast PBPF, where it was suggested that heating the polymer reduces the spatial restrictions of the molecules and results in increased mobility in the crystalline domain. At this stage, it is not clear what this motional threshold is that determines which regions of the polymer end up corresponding to the amorphous or the crystalline signals, but the model which follows is supported by the experimental results. Assume that an arbitrary macromolecule is located within the crystalline domain. The closely packed neighbors effectively restrict its mobility resulting in strong homonuclear dipolar couplings to remain causing a high degree of homogeneous broadening of the signal. As there is little motion these interactions do not lead to significant relaxation hence the signal relaxes slowly. As the temperature increases, this macromolecule is allowed to take on higher degrees of freedom. Even though this increased mobility decreases the homonuclear dipolar interactions it is not sufficiently removed to quench the relaxation caused by the motion. As a result faster relaxation is observed. As the temperature increases the dipolar interactions are removed to a point where they no longer contribute

significantly to the relaxation and the relaxation behavior is expected to be similar to that seen for the amorphous domain. This transformation occurs gradually upon heating, involving neighboring macromolecules and propagating throughout an entire volume of the crystalline domain with time, until the thermotropic transition temperature is reached. At the same time, the relaxation constant for these components is expected to decrease. In essence, this is supported by the data in figure 74, where the relaxation of peak 3 decreases with temperature, as it contributes to peak 1, until exchange reaches equilibrium at about 38 ms. Peak 2, which is believed to correspond to the mesophase of PBFP, emerges at 90ºC and has slightly shorter relaxation than that of peak 1. This confirms that transformation of the rigid crystalline domain into a mobile extended chain morphological conformation occurs at temperatures between 90ºC and 100ºC.

The results offered by ^{31}P VT MAS NMR spinlock experiments on the solvent-cast PBFP, provide useful information about spin-lattice relaxation rates in the rotating frame for all three peaks observed in the spectra. The interpretation of these results is consistent with behavior of the working theoretical model for transformations within PBFP upon heating.

3.10 ^{31}P MAS NMR of a reaction mixture at different stages of thermal ring-opening polymerization of hexachlorocyclotriphosphazene

Different stages of the thermal ring-opening polymerization of hexachlorocyclotriphosphazene $(NPCl_2)_3$ were probed using ^{31}P MAS NMR. Figure 75 shows spectra of the starting material and the products mixture after 3, 8 and 17.5 h of polymerization.

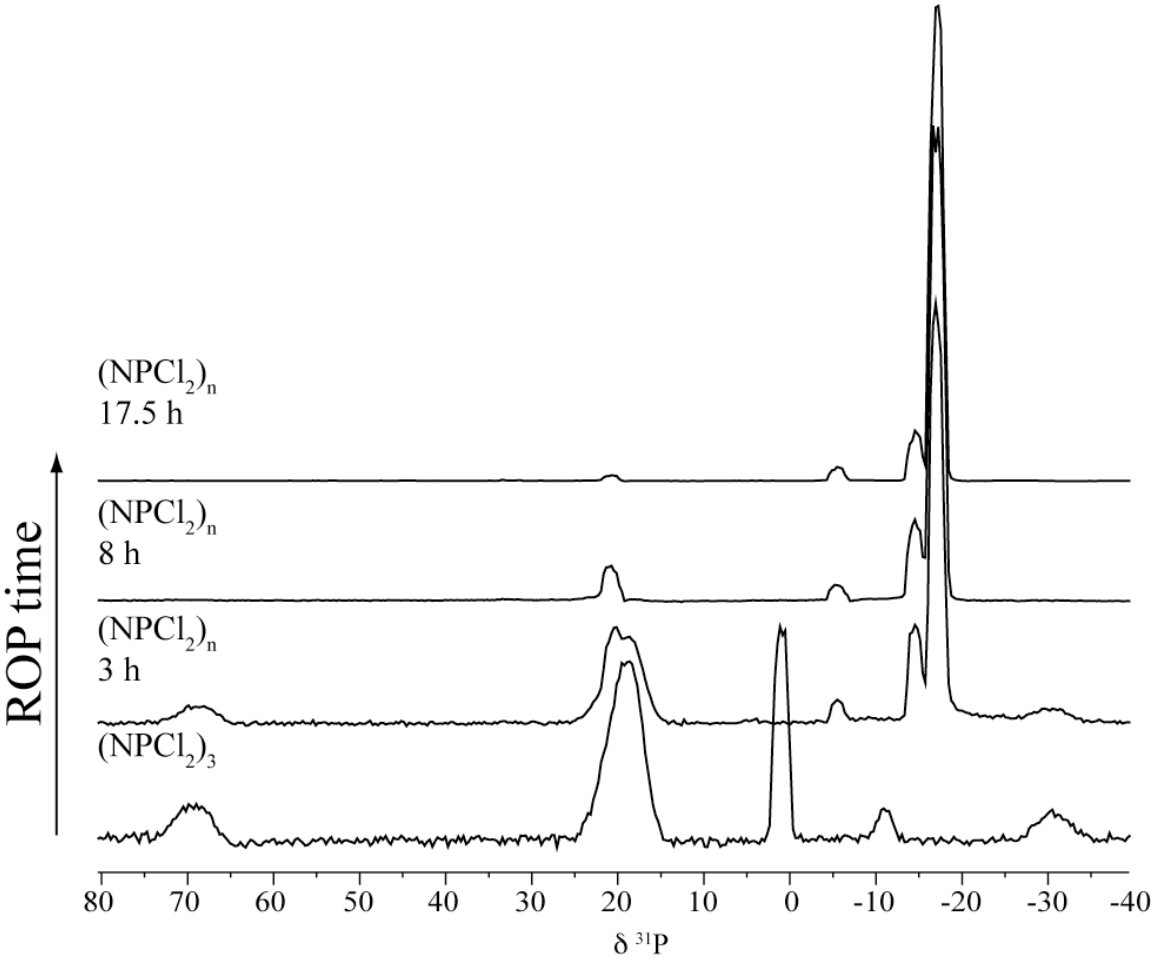

Figure 75 One-dimensional 202 MHz ^{31}P MAS NMR of the reaction mixture during different stages of the thermal ring-opening polymerization of hexachlorocyclotriphosphazene. MAS rate 10 kHz.

The spectrum of unreacted $(NPCl_2)_3$, in the bottom of figure 75, contains a side-band pattern centered at 19 ppm which is assigned to cyclic three- and four-member species. The inhomogeneous broadening of the signal is caused by residual couplings to ^{14}N, and by a distribution of frequencies due to a large distribution in CSA's of the rigid phosphazene rings. Two peaks found at 0.8 and –11 ppm correspond to the partially polymerized cyclic species and to the hydrolysis products, respectively. The deceptive high intensity of the signal at 0.8 ppm is due to its much shorter T_1 (as determined by a saturation-recovery experiment) than that of the trimer. As a result, relaxation delays used in these spectra were too short to allow for the longitudinal relaxation of the trimer signal between successive RF pulses. This caused the disproportionate distribution of the intensities between the signals observed in the spectra. After 3 h of heating at 250ºC, a new peak arises at –17 ppm, which represents the superimposition of signals from linear high molecular weight poly[dichlorophosphazene] of different chain lengths. The additional signal at –6 ppm corresponds to the high member cyclic $(NPCl_2)_n$, where n can be as high as 8.[125] The shoulder on the down-field side of the main polymer signal appears at –15 ppm and is assigned to low molecular weight oligomers, in which chains are short enough to be affected by the end-units. Furthermore, the peaks at 0.8 and –11 ppm disappear indicating the loss of hydrolysis products due to their conversion to polymer chains at high temperature. Depletion of the trimer and tetramer starting materials is reflected by a lower intensity of the signal at 19 ppm. Similar behavior can be observed in the spectrum at 8 h of ROP, where the ratio between absolute intensities of $(NPCl_2)_n$ and $(NPCl_2)_3$, is further increased, and the intensity of the signal at –6 ppm indicates that the ROP leads to chain propagation without producing additional five-

member cyclic phosphazenes. Finally, at 17.5 h one can readily appreciate the very low intensity of the signal at 19 ppm due to only trace amounts of cyclic trimer and tetramer species present in the reaction mixture. Meanwhile the unchanged intensity of the signal at –6 ppm confirms that most of the starting material has been converted to high molecular weight poly[dichlorophosphazene] chains.

The origin of the signal at 19 ppm was independently verified by ^{31}P MAS NMR of the phenoxy-substituted hexachlorocyclotriphosphazene. Purification via recrystallization has proven effective in removing all tetramer and higher member cyclic species leaving one signal from chlorinated trimer. Substitution of chlorines in the phosphazene ring results in the non-equivalence of phosphorous atoms, which in turn will alter the appearance of the ^{31}P NMR spectrum. Reaction of $(NPCl_2)_3$ with sodium phenoxide (1.2 equiv) produces a mixture of un-substituted (**I**), mono-substituted (**II**) and di-substituted (**III**) cyclotriphosphazenes, as depicted in figure 76 *vide infra.*

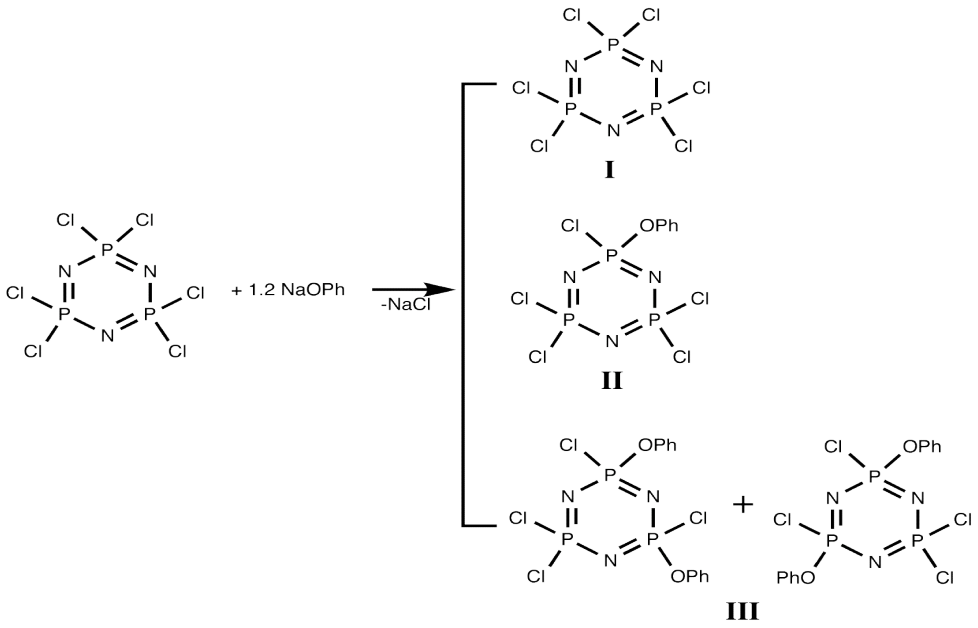

Figure 76 Preparation of the phenoxy-substituted hexachlorocyclotriphosphazene.

As expected, the corresponding ^{31}P MAS NMR spectrum shown in figure 77 contains the following signals: δ ^{31}P 23.71 (td, J_{PP} 66.1 and 23.0), 21.36 (d, J_{PP} 62.3), 14.65 (dd, J_{PP} 66.4 and 47.3), 11.42 (t, J_{PP} 62.5).

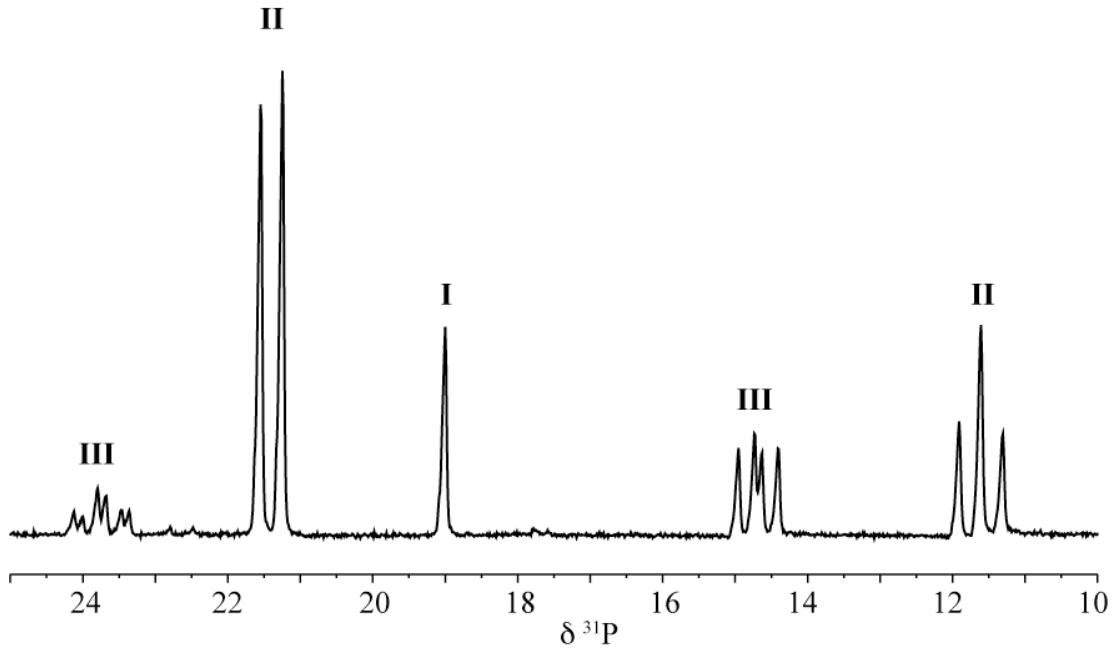

Figure 77 One-dimensional 202 MHz ^{31}P MAS NMR spectrum of the phenoxy-substituted hexachlorocyclotriphosphazene. MAS rate 10 kHz.

The narrow character of lines indicates that: firstly, no high-member phosphazene rings are present in the mixture, and secondly, that a high degree of molecular motion results in the very narrow frequency offsets between species of the same type, which indicates that no branching due to hydrolysis occurs between the trimer rings. This makes it a particularly convenient structural model system to validate two-dimensional ^{31}P–^{31}P RFDR and INADEQUATE MAS NMR experiments for obtaining information about P–N–P connectivities and couplings. These would be further modified so that they can be subsequently applied to the high molecular polymers of interest.

3.11 Two-dimensional ^{31}P – ^{31}P MAS NMR of polyphosphazenes

First, the RFDR spectrum of the phenoxy-substituted hexachlorocyclotriphosphazene is presented. Recall that this experiment selects signals from directly coupled spins pairs, where peaks from identical spin species appear along the diagonal of the spectrum, whilst cross-peaks indicate through-space connectivities in the molecule. This indeed is seen to be the case, as shown in figure 78, where three groups of signals can be discriminated on the basis of their connectivities.

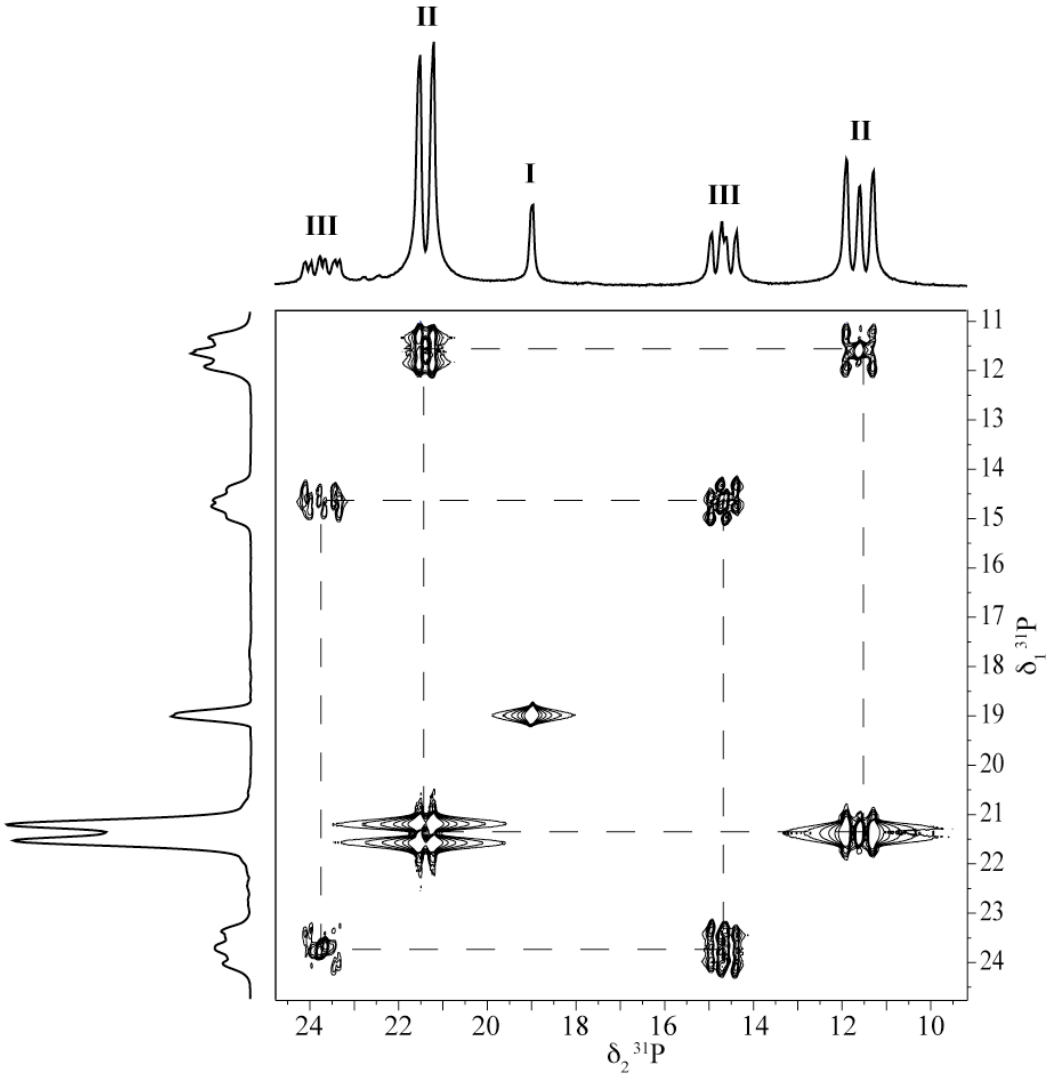

Figure 78 Two-dimensional 202 MHz ^{31}P – ^{31}P RFDR MAS NMR spectrum of the phenoxy-substituted hexachlorocyclotriphosphazene. MAS rate 10 kHz.

As such, this spectrum suggests that the doublet at 21.36 ppm correlates to the triplet at 11.42 ppm, which corresponds to **II**; the triplet of doublets at 23.71 ppm correlates to the doublet of doublets at 14.65 ppm, which is assigned to **III**; and finally, the singlet at 19 ppm corresponds to **I**.

This peak assignment was independently verified by the 2D ^{31}P INADEQUATE NMR experiment, which resulted in the spectrum shown in figure 79.

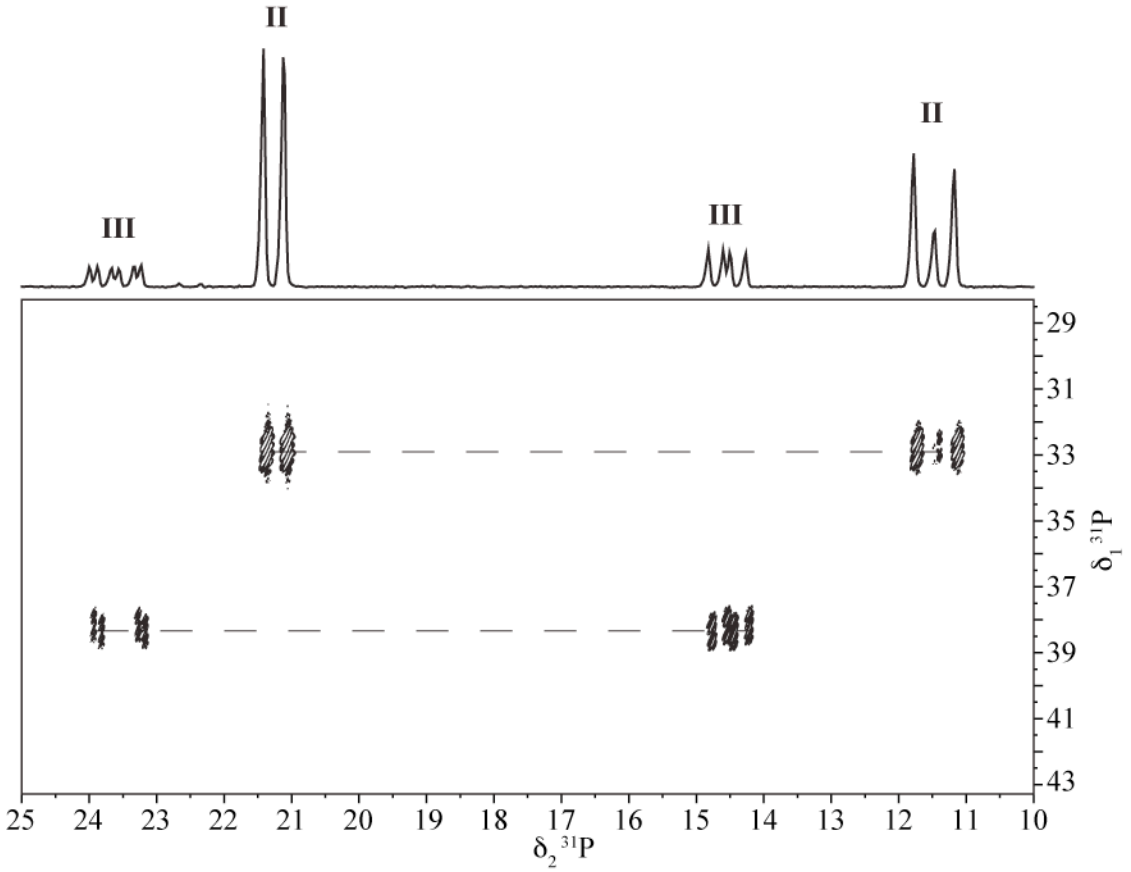

Figure 79 Two-dimensional 202 MHz ^{31}P – ^{31}P INADEQUATE MAS NMR spectrum of the phenoxy-substituted hexachlorocyclotriphosphazene. MAS rate 10 kHz.

The INADEQUATE experiment only selects signals from through-bond coupled spin pairs while suppressing signals from isolated spins. Unlike the RFDR spectrum shown previously, signals along the diagonal are not observed; instead the spectrum in figure 79 contains correlation peaks resulting from the evolution of the double quantum coherences under J-coupling. Correspondingly, the peaks in the indirect dimension appear at the double quantum frequency, $\nu_{DQ} = \nu_A + \nu_X$. It becomes apparent that J-coupling occurs between signals at 21.36 and 11.42 ppm, and 23.71 and 14.65 ppm confirming their assignment to **II** and **III**, while the signal at 19 ppm corresponding to the un-substituted hexachlorocyclotriphosphazene is suppressed.

At this stage, it would be useful to apply these two-dimensional MAS NMR experiments to the high molecular weight substituted phosphazene polymers. One such system of particular interest is a partially trifluoroethoxy-substituted poly[dichlorophosphazene] as it can potentially provide valuable insight on the chain structure and the mechanism of nucleophilic substitution. The polymer was prepared as described in section 2.2.8 and was expected to show a complex ^{31}P NMR spectrum, which would contain signals from the high molecular weight un-substituted poly[dichlorophosphazene] and fully substituted poly[*bis*(trifluoroethoxy)phosphazene], as well as a mixture of unreacted cyclic phosphazenes, short-chain oligomers, hydrolysis products, cross-linked chains and polymer chains with heterogeneous side chains containing chlorines and trifluoroethoxy units in various proportions and conformations. Accordingly, the $^{31}P\{^{1}H,^{19}F\}$ spectrum of the partially substituted $(NPCl_2)_3$, shown in figure 80, reveals complex structure with 10 different peaks being distinguished. The preliminary assignment of the peaks will be performed on the basis of known chemical

shifts in the spectra of hexachlorocyclotriphosphazene, poly[dichlorophosphazene] and poly[*bis*(trifluoroethoxy)phosphazene], and will be supported by two-dimensional ^{31}P RFDR and INADEQUATE homonuclear experiments.

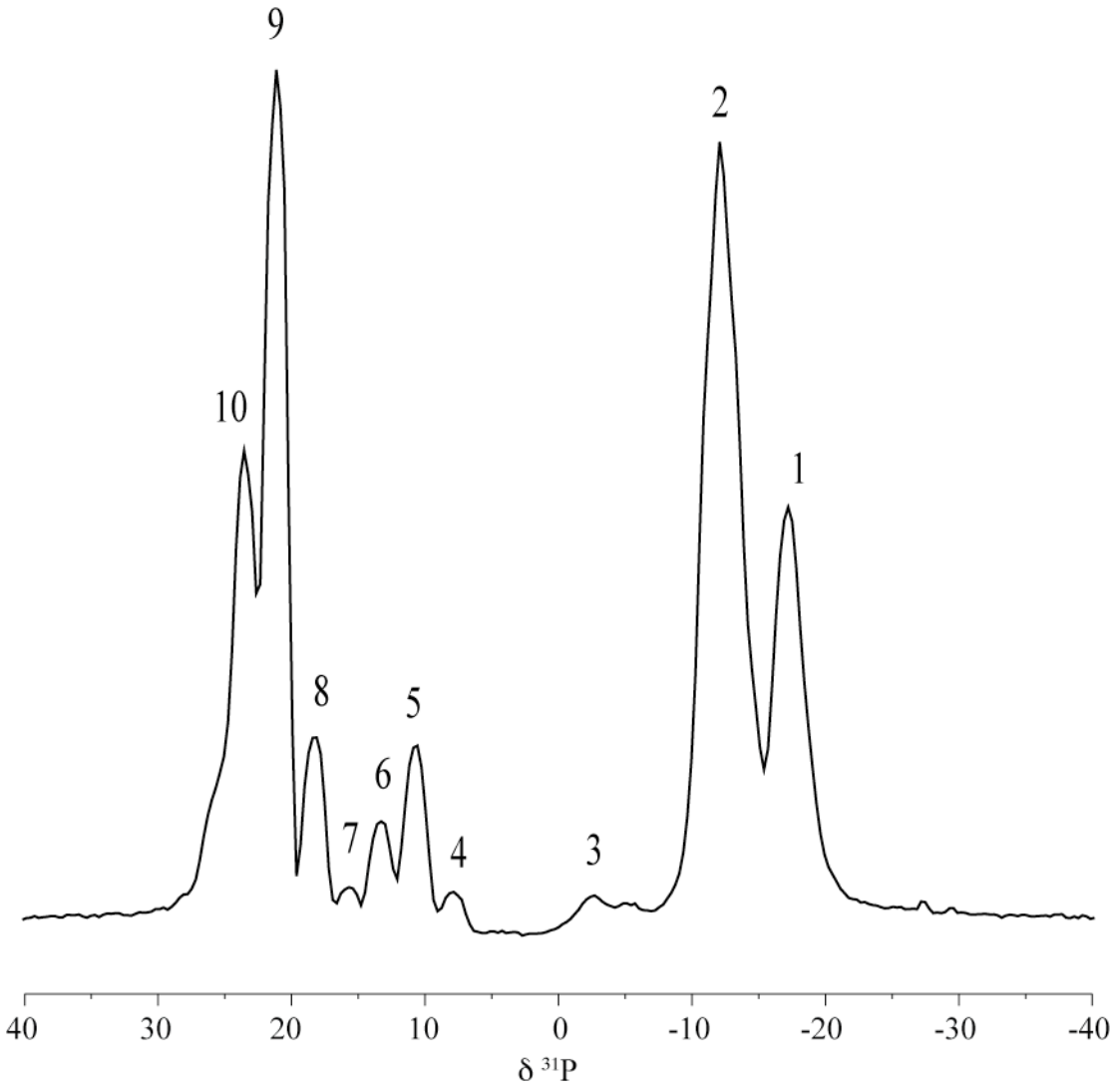

Figure 80 One-dimensional 202 MHz $^{31}P\{^{1}H,^{19}F\}$ MAS NMR spectrum of the partially trifluoroethoxy-substituted poly(dichlorophosphazene). MAS rate 10 kHz.

In order to assist with spectral assignment it is best to superimpose the spectrum of the partially substituted polymer with the previously discussed spectra of the starting cyclic phosphazenes, chlorinated polymer and solvent-cast PBFP as a structural model of the fully substituted poly[*bis*(trifluoroethoxy)phosphazene]. This is shown in figure 81.

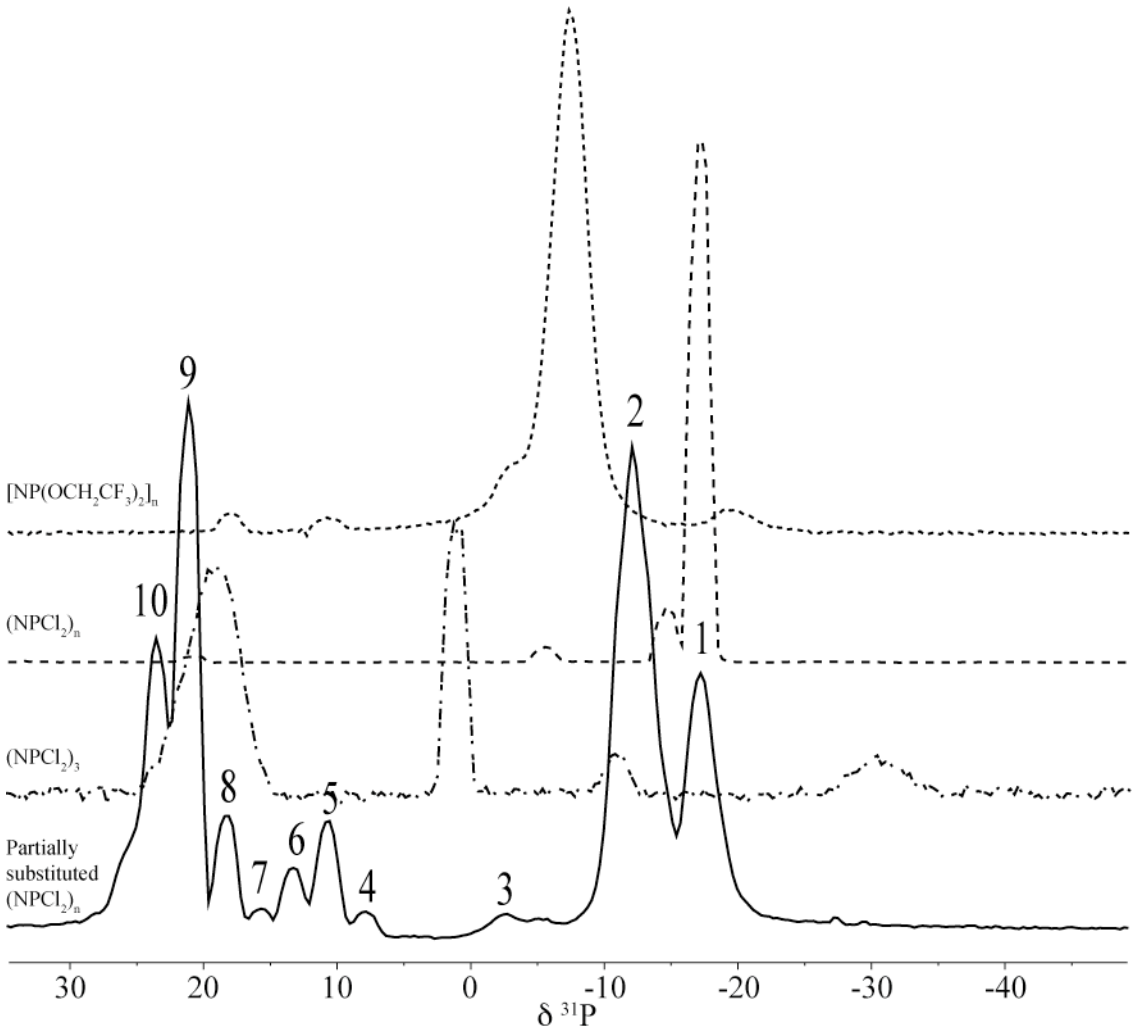

Figure 81 Superimposed 202 MHz ^{31}P MAS NMR spectra of the partially substituted $(NPCl_2)_n$, $(NPCl_2)_3$, $(NPCl_2)_n$ and $[NP(OCH_2CF_3)]_n$. MAS rate 10 kHz.

Peak 1 arises at –17.1 ppm, which corresponds to the chemical shift of the high molecular weight poly(dichlorophosphazene). The line is broadened compared to the original signal from the chlorinated polymer (730 Hz *vs* 402 Hz), which can be explained by the branching and cross-linking between macromolecular chains that in turn restricts their mobility and hence results in a larger CSA. The next major resonance, 2 (δ –12.1), does not occur in any of the presented spectra, which leads to the conclusion that it must therefore correspond to a new type of species. It has been shown previously[125] that the substitution of chlorine atoms by various alkoxy nucleophiles causes a positive shift of the δ ^{31}P. Taking into account that line 2 appears between the resonances of the poly(dichlorophosphazene) (–17 ppm) and the fully substituted solvent-cast PBFP (–7.5 ppm), it can therefore be inferred that peak at –12.1 ppm corresponds to the chloro-polymer chains that contain approximately 50% trifluoroethoxy side-chains. This signal, at 731 Hz wide, is very similar in appearance to peak 1, and their intensities suggest a 2:1 ratio between the respective polymer species. The broad signal 3 centered at –3.5 ppm is characterized by low intensity and upon closer inspection appears to be composed of several contributions. When correlated to the chemical shifts of the signals found in the spectra of the $(NPCl_2)_n$ and the fully substituted solvent-cast PBFP, one can notice that the resonance group 3 contains two lines corresponding to the high-member cyclic phosphazenes and the crystalline region in the spectrum of the $[NP(OCH_2CF_3)_2]_n$, at –5.6 and –3.5 ppm, respectively. Accordingly, this indicates that the final mixture of products contains trace amount of cyclic species, and that the fully trifluoroethoxy-substituted polymer chains formed rigid lamellae; however, their relative amount is insignificant compared to the unsubstituted and partially substituted polymer. Subsequently, peaks 4

through 7 likely represent a distribution of a variety of cyclic chlorophosphazenes containing different number of phosphorus atoms in the ring. Noteworthy is resonance 5 at 10.7 ppm, which can be also observed in the spectrum of solvent-cast PBFP. At this point, definite assignment of this peak remains elusive; however, based on the notion that increased size of the phosphazene ring causes the negative shift of the corresponding frequency, it can be suggested that peak 5 represents the hexamer species. Similarly, signals 7, 6 and 4 would correspond to the four-, five- and seven-member cyclic phosphazenes, respectively. Subsequently, this working model allows for the assignment of peak 8 (δ 18) to the hexachlorocyclotriphosphazene, which is consistent with its chemical shift determined previously. Origins of the intense narrow signal 9 at 21.2 ppm and the narrow line overlapped with a broad shoulder centered at 23.7 ppm, are yet to be determined. At this stage, their assignment is not supported by chemical shifts of the known signals, nor can their high relative intensities be explained. In congruence with the current understanding of the behavior of cyclic phosphazenes upon heteroatom substitution, it can be therefore hypothesized that signals 9 and 10 correspond to the partially trifluoroethoxy-substituted chlorocyclophosphazenes.

Two-dimensional RFDR and INADEQUATE NMR experiments were employed in order to verify the preliminary assignments of the signals in the ^{31}P spectrum of the partially trifluoroethoxy-substituted poly(dichlorophosphazene) as well as to confirm the accuracy of the working model of the polymer behavior upon reaction with nucleophiles.

The RFDR phase-sensitive spectrum is presented in figure 82. Notice the very high resolution in the direct dimension. All signals identified in the one-dimensional ^{31}P spectrum become resolved into separate narrow components, which likely correspond to

low molecular weight species, while the higher molecular weight species are not observed due to their short T_2's, which is caused by the fast quadrupolar relaxation of ^{14}N that is transferred to ^{31}P through scalar couplings.

One can readily appreciate that two separate groups are formed by signals 1 and 2, and 5 through 10. Signals 3 and 4 are not observed due to their low intensity.

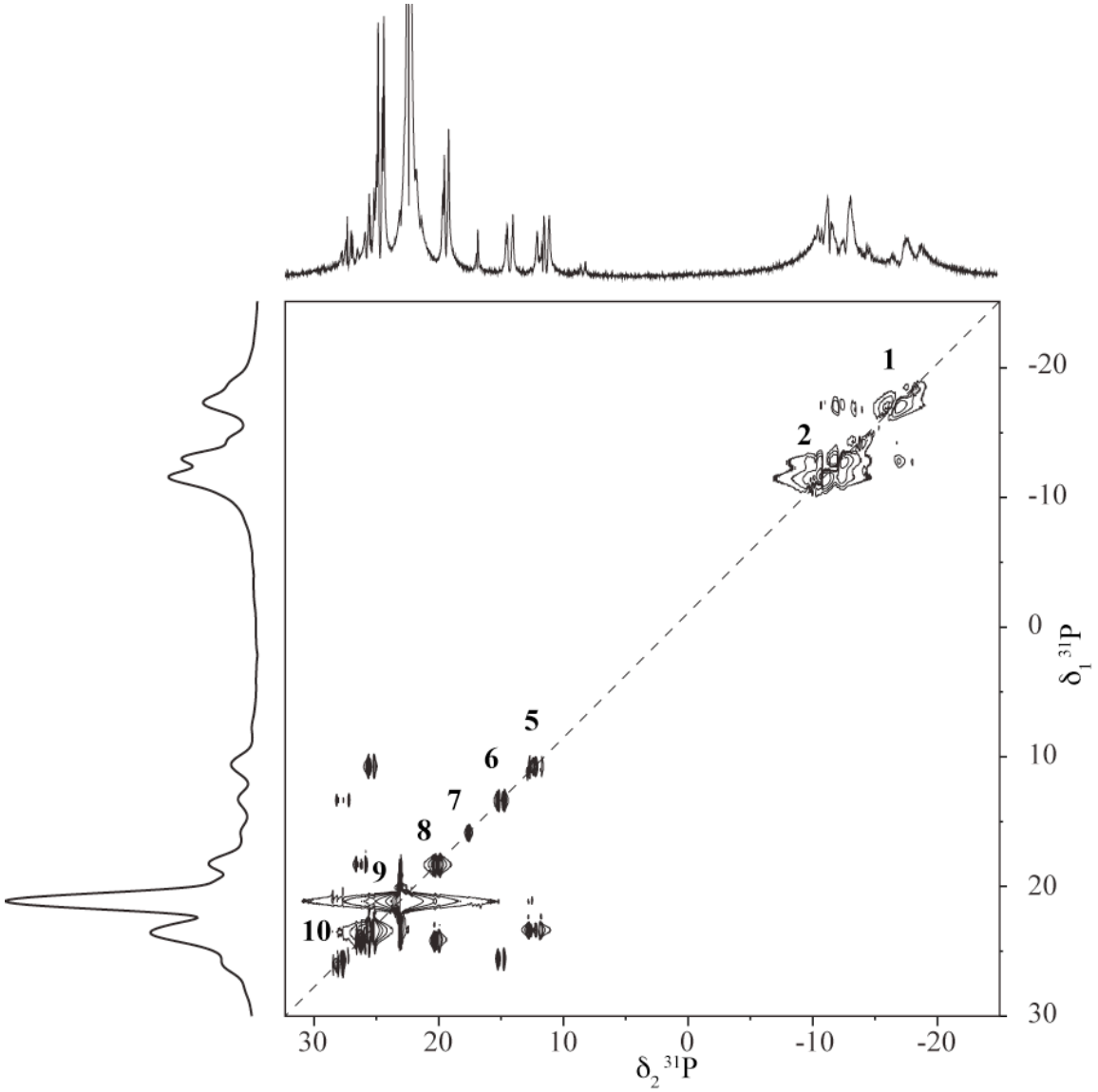

Figure 82 Two-dimensional 202 MHz ^{31}P – ^{31}P RFDR MAS NMR spectrum of the partially trifluoroethoxy-substituted poly(dichlorophosphazene). MAS rate 10 kHz.

Recall that signals 1 and 2 were assigned to the high molecular weight poly(dichlorophosphazene) and to the chlorinated polymer with partially trifluoroethoxy-substituted side-chains, respectively, which appear to be close in spatial geometry, as suggested by the cross-peaks between multiple components in 1 and 2 observed in the spectrum. Figure 83 shows the expansion of this particular region of the spectrum.

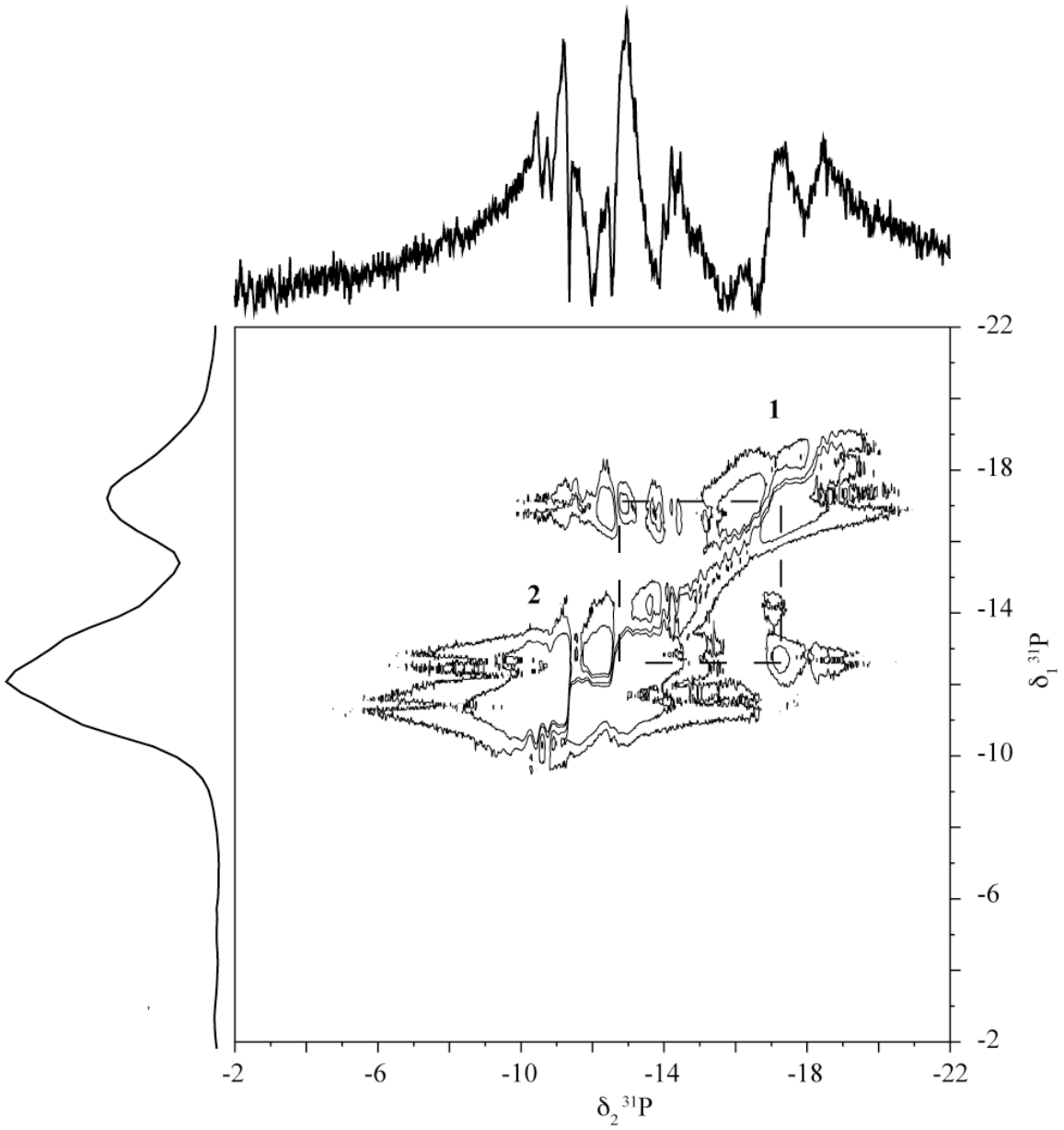

Figure 83 Expansion of the two-dimensional 202 MHz ^{31}P – ^{31}P RFDR MAS NMR spectrum of the partially trifluoroethoxy-substituted poly(dichlorophosphazene) showing the resonance groups 1 – 2. MAS rate 10 kHz.

On the other hand, signals 4 through 10 form a complex dipolar coupling pattern, with multiple cross-peaks between different frequencies observed in the spectrum. In order to assist with the interpretation of the spectrum, the expansion of that region is shown in figure 84.

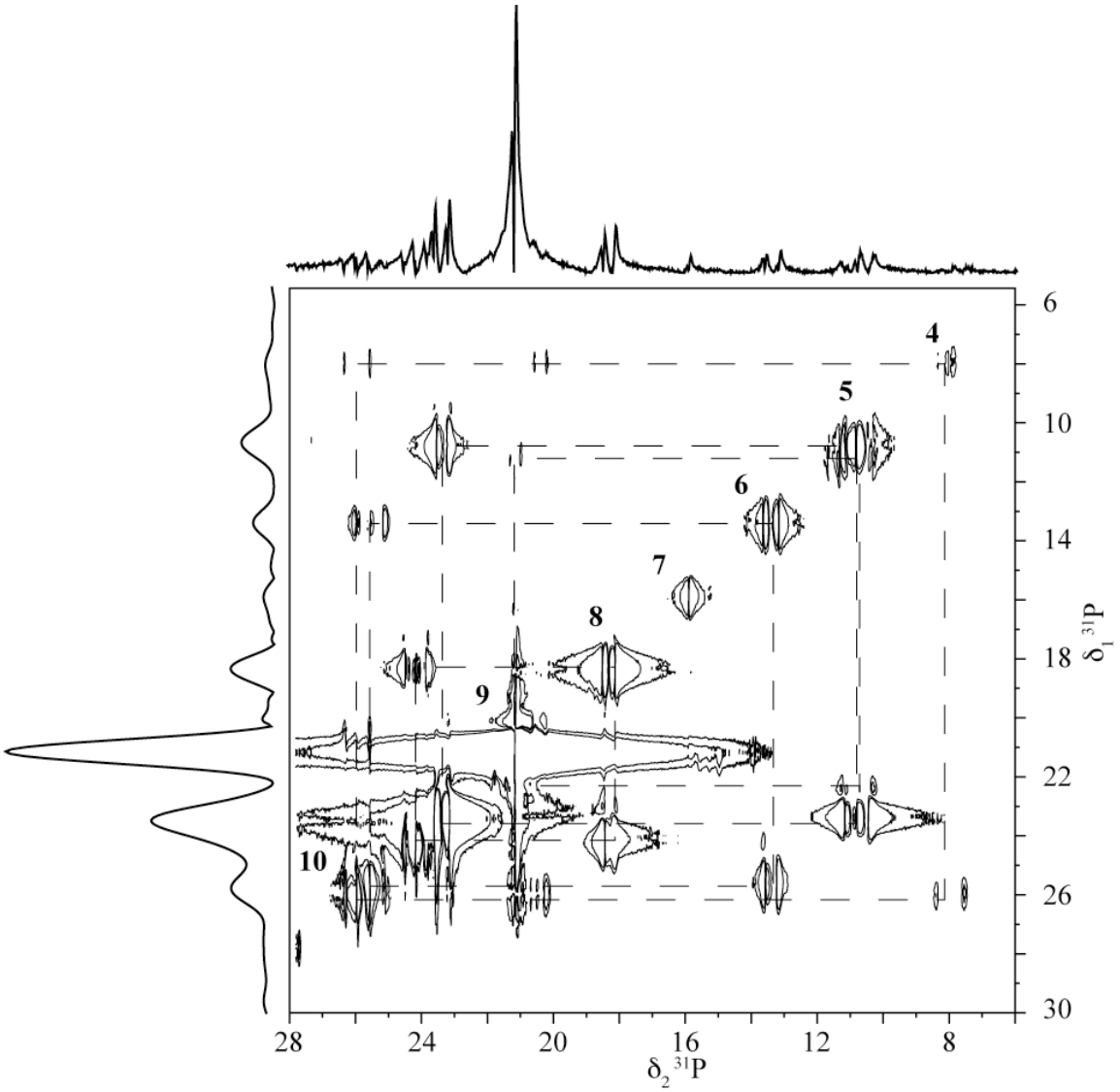

Figure 84 Expansion of the two-dimensional 202 MHz ^{31}P – ^{31}P RFDR MAS NMR spectrum of the partially trifluoroethoxy-substituted poly(dichlorophosphazene) showing the resonance groups 4 – 10. MAS rate 10 kHz.

It is clear that peaks 4, 5, 6 and 8 correlate with different contributions to the signal identified as 10. In addition, peak 5 also forms cross-peaks with resonance 9, and peak 7 does not seem to correlate to any of the signals in the spectrum. Definite interpretation of this complex behavior requires additional information about through-spatial and through-bond connectivities in the material, and hence two-dimensional INADEQUATE was employed to distinguish between J-coupled signals, as seen in figure 85.

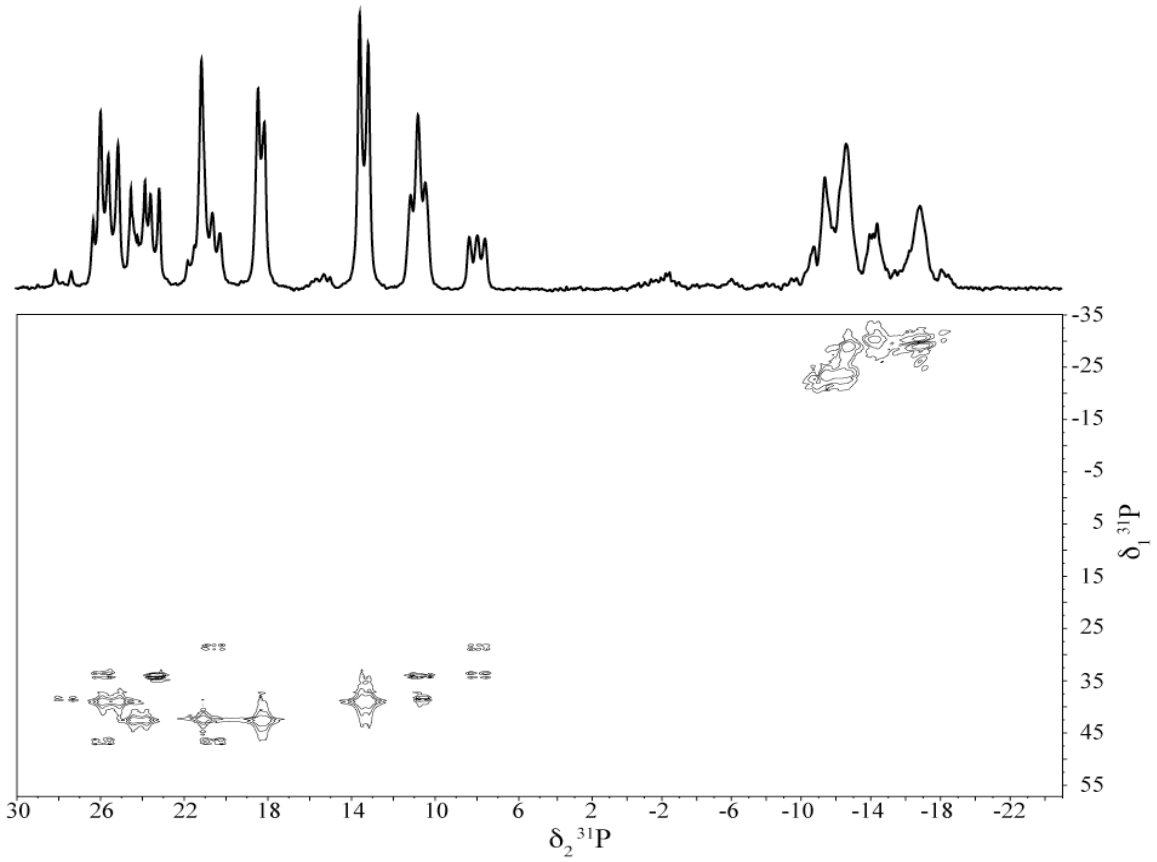

Figure 85 Two-dimensional 202 MHz ^{31}P – ^{31}P refocused INADEQUATE MAS NMR spectrum of the partially trifluoroethoxy-substituted poly(dichlorophosphazene). MAS rate 10 kHz.

Consistent with the RFDR spectrum, a very detailed signal structure is observed in the direct dimension, which is indicative of the presence of low molecular weight species in the sample and, on the other hand, elimination of the signal from the high molecular

weight chains on the basis of their short T_2. This allows for detailed correlation of the different components in the identified signals through J-coupling. At a glance, one can notice that two separate groups of correlating signals are present in the spectrum, where no cross-peaks are formed between signals 1 and 2, and the remaining ones, and therefore it would be useful to examine them independently, as shown in the expansions of the spectrum in figure 86.

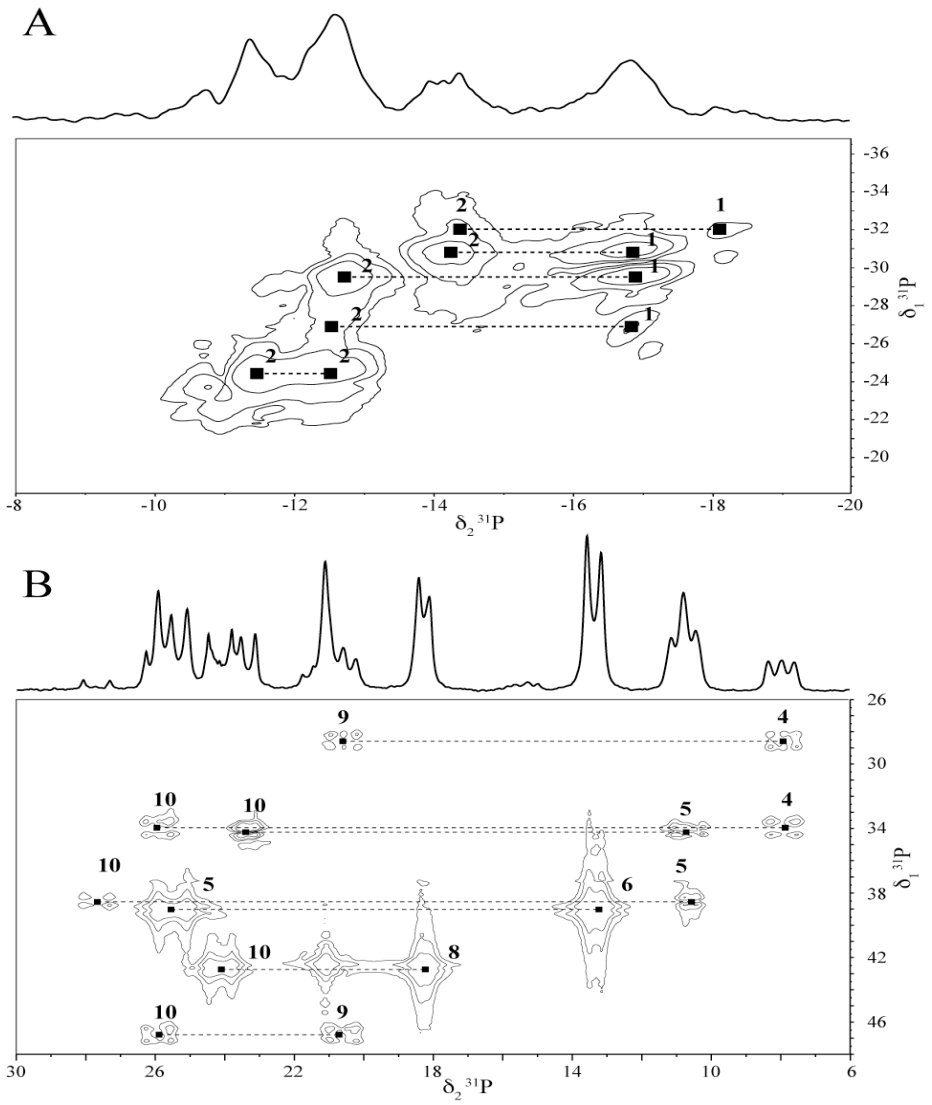

Figure 86 Expansions of the two-dimensional 202 MHz ^{31}P – ^{31}P refocused INADEQUATE MAS NMR spectrum of the partially trifluoroethoxy-substituted poly(dichlorophosphazene) showing the resonance groups 1 – 2 (A) and 4 – 10 (B). MAS rate 10 kHz.

From the expansion of the INADEQUATE spectrum in figure 86 A it follows that the chains of the poly(dichlorophosphazene) and the partially trifluoroethoxy-substituted poly(dichlorophosphazene) are branched, and this interpretation is consistent with the results obtained from the RFDR experiment. As such, four correlations through J-coupling between 1 and 2 are readily noticeable. In addition, the doublet centered at about –12 ppm indicates that the branching occurs not only between chains with different side-chain units, but also between chains of the similar type. Accordingly, it is apparent that high molecular weight polymers are not bonded to the cyclic species since no correlation peaks can be observed.

Upon closer examination of the expansion of the INADEQUATE spectrum shown in figure 86 B, it is possible to establish connectivities between different cyclic phosphazene species. Recall that the low molecular weight chlorocyclophosphazenes were assigned to signals 4 through 8, according to the number of phosphorous atoms they contain. Therefore, from this interpretation it follows that the smaller cyclic species are attached to the larger partially trifluoroethoxy-substituted cyclic chlorophosphazenes as pendant groups. This is seen in the spectrum, which contains very distinct peaks correlating signals 4, 5, 6, and 8 to signals 9 and 10. Surprisingly, no coupling partner could be indentified for the intense peak near 21.2 ppm; however, as it is clear that this signal has not been cancelled it cannot correspond to an isolated spin species. Taking into account its characteristic frequency in the double quantum domain as well as the broad shape, it can be suggested that this peak correlates signals within group 9 that are very close in frequencies. Furthermore, notice the correlation between peaks 9 and 10, which indicates the connectivity between different partially-substituted

chlorocyclophosphazenes. Similar to the RFDR spectrum, no information about relative location or connectivities can be obtained for signal 7.

In conclusion, interpretations of the two-dimensional RFDR and INADEQUATE spectra are consistent between each other and support the suggested assignment of signals in the one-dimensional ^{31}P MAS NMR spectrum of the partially trifluoroethoxy-substituted PBFP. Moreover, of significant importance is the dramatically improved resolution of the signal in the direct dimension in both 2D experiments presented. Figure 87 shows the comparison between the original one-dimensional spectrum as opposed to the projections of the direct dimension in the RFDR and INADEQUATE spectra.

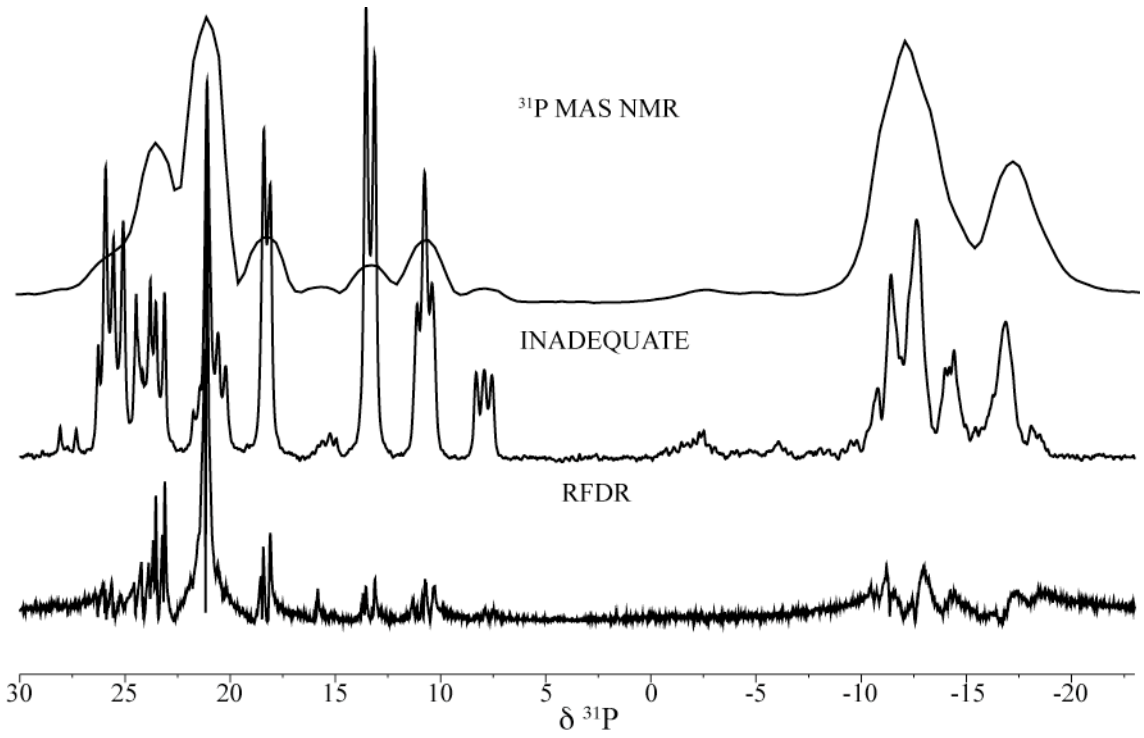

Figure 87 Superimposition of the 202 MHz ^{31}P MAS NMR spectrum of the partially trifluoroethoxy-substituted poly(dichlorophosphazene), and the projections of direct dimension in the 2D RFDR and INADEQUATE spectra of the same sample.

It can be seen that signals in the one-dimensional spectrum become resolved into narrow multiplet structures. From such spectra, very interesting insight about chain arrangement, branching, cross-linking and molecular structure can be obtained. At this stage it would be useful to perform these experiments at variable temperatures, as the differences in mobilities of various environments of the material will be reflected by changes in corresponding signals in the spectrum. In addition, it is essential to conduct similar studies observing all NMR sensitive nuclei in a polymer, which would to a great extent contribute to the existing body of knowledge about its morphology and other parameters of importance. Finally, results offered by the RFDR and INADEQUATE experiments have led to a possibility of the development of new one-dimensional NMR experiments employing pulse sequences for the dipolar recoupling or the double quantum coherence evolution under J-coupling, as effective filtering techniques that can provide very high resolution.

With these successful and convincing results in mind, two-dimensional RFDR and INADEQUATE experiments were applied to the fully substituted solvent-cast batch 1 PBFP; however, they proved completely ineffective for probing such a polymer system. Likewise, the 2D INADEQUATE spectra did not contain any signal, most likely due to the high flexibility of the long polymer chains, and hence short T_2. As a result, the signal relaxes too fast compared to t_1, and hence the time allowed for the double quantum coherence evolution is insufficient to produce any signals.

Similarly, the 2D RFDR spectrum only shows two correlating peaks common to the one-dimensional ^{31}P MAS NMR of PBFP. An expansion of the region of interest is

shown in figure 88, and from such a spectrum no information other than the dipolar-based correlation between the peaks at –7.5 and –6.5 ppm, can be extracted.

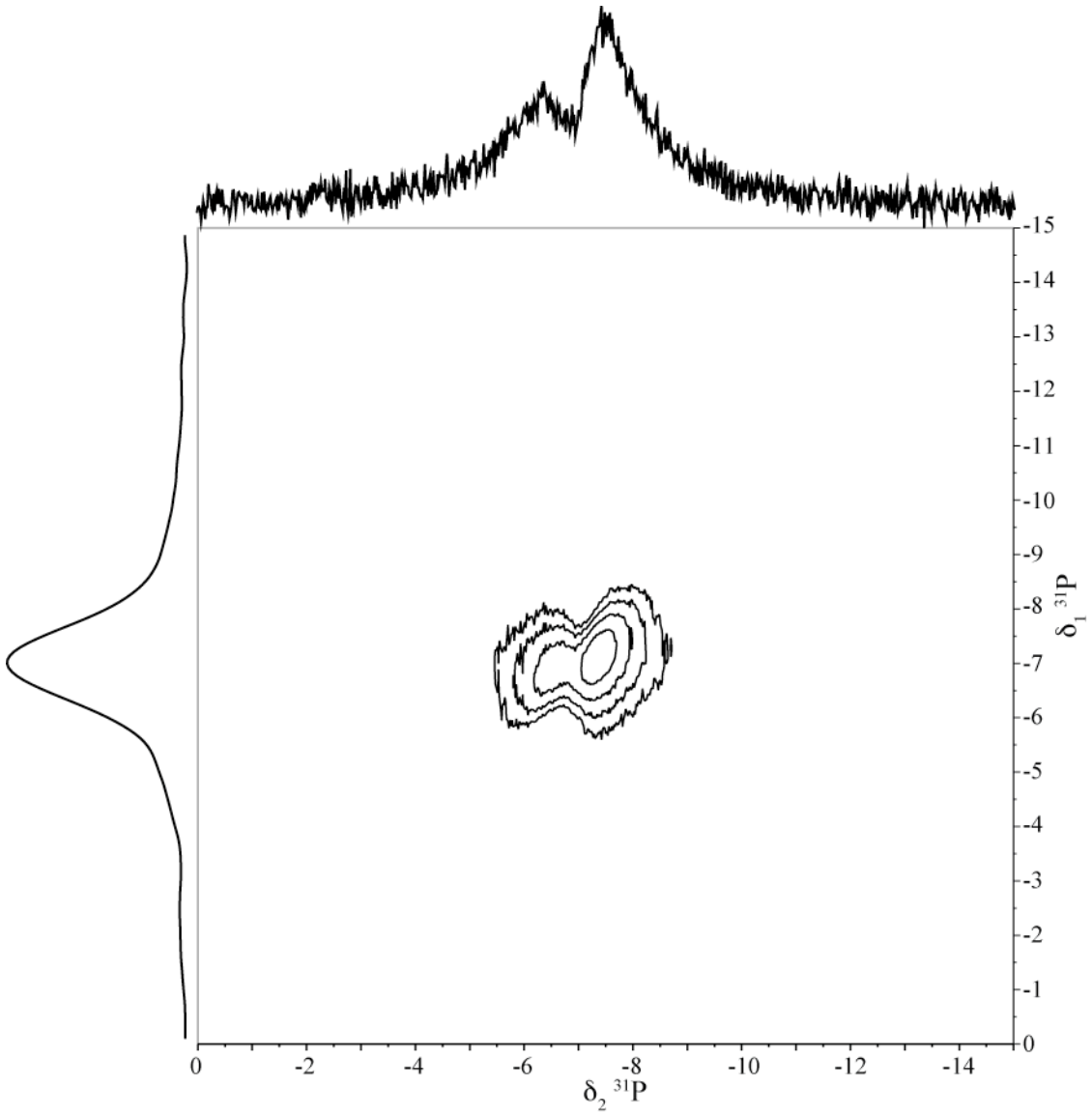

Figure 88 Two-dimensional 202 MHz ^{31}P – ^{31}P MAS NMR spectrum of solvent-cast batch 1 PBFP. MAS rate 10 kHz.

Significant differences in the resolution between the RFDR and INADEQUATE spectra of the partially and fully trifluoroethoxy-substituted polyphosphazene must be caused by the much higher chain flexibility and mobility of the latter. Correspondingly,

it can be suggested that the branching between long chains of the partially substituted polymer occurs to a considerable degree, which to an extent restricts the macromolecular flexibility and dynamics. Hence, the increased relaxation time and efficient selectivity on the basis of dipolar interactions. In addition, a lack of any information in the RFDR and INADEQUATE spectra of the fully substituted PBFP indicates that the polymer has been separated from the low molecular weight species during the purification process, and hence their signals are not observed.

Repeating two-dimensional RFDR and INADEQUATE MAS NMR experiments on the fully substituted high molecular weight PBFP at temperatures below the glass transition should dramatically reduce the chain mobility within various environments in the polymer, allowing for efficient discrimination between separate contributions to the signal and their assignment to the corresponding macromolecular species.

4 CONCLUSIONS

Deconvolution analyses of the ^{1}H, ^{19}F, ^{31}P and ^{13}C one-dimensional MAS NMR spectra of three different samples of poly[*bis*(trifluoroethoxy)phosphazene] prepared via thermal ring-opening polymerization of hexachlorocyclotriphosphazene, suggest that at ambient temperature the polymer exhibits complex morphological behavior. All spectra contained signals from the crystalline, amorphous and mesophase environments within the material. Deconvolution analyses gave intensities, widths, areas and shapes of the corresponding lines. Significant contributions from the crystalline domain within the polymer cast from solvent were observed as broad Gaussian lines. According to the existing morphological model of PBFP, these signals were assigned to the spherulitic structures with lamellae consisting of either β-monoclinic or γ-orthorhombic crystallites, or a combination of the two. Heat-treatment of the samples increased the overall crystallinity of the polymer as the contribution from the broad lines increased dramatically. As such the crystallinity of PBFP, batch 1 and batch 2 PBFP increased on average by 20%, as determined by the areas under the crystalline peaks. On the other hand, changes exhibited by the narrow contributions were not uniform between preparations and therefore indicate that different mesophases within the polymer either increase or convert to the crystalline lamellae; however, the mechanism defining this behavior is not well understood at this time. In addition, comparison was made between batch 1 and batch 2 PBFP, which differed in reaction time for the nucleophilic substitution, where deconvolution results confirm that increased reaction time results in

higher overall crystallinity, as was demonstrated by the higher intensity of the crystalline peak in the spectra of batch 2 PBFP.

Quite the opposite observations were drawn on the spectra of PBFP prepared via living cationic polymerization. The ratio between contributions from narrow and broad components in the signals suggests that the polymer contains mostly amorphous and mesophase regions. This follows from the low thermal energy regime of the synthesis, which does not allow the formation of large crystalline structures within the polymer.

Variable-temperature ^{31}P MAS NMR spectra of the solvent-cast PBFP initially contained both crystalline and the amorphous signals at ambient temperature, and as the temperature was increased to 80ºC, the contribution from the crystalline region decreased dramatically. It completely vanished at 90ºC, where also a new narrow component emerged which was assigned to the mesophase. This behavior is consistent with the known temperature range of the thermotropic phase transition determined by DSC.[131]

^{31}P spin-lock experiments on solvent-cast PBFP allowed for the determination of $T_{1\rho}$ for each component in the signal. At ambient temperatures the crystalline component exhibited a nearly three times greater $T_{1\rho}$ than that of the amorphous component. These observations confirm that the crystalline and the amorphous environments within the polymer are characterized by significantly different mobilities. Upon further heating, the $T_{1\rho}$ of the broad peak decreased, which is indicative of the increasing degree of molecular motion occurring in the crystalline domain with temperature. Finally, the thermotropic transition caused the crystalline region to convert to a liquid crystalline phase, and hence the respective broad peak disappeared at a temperature near 80ºC, as the new narrow peak from the mesophase became observable upon thermotropic phase transition. As the

amorphous and mesophase components can be resolved, their respective $T_{1\rho}$ were determined independently. The temperature dependence of their relaxation rates beyond 90ºC suggests that these regions are characterized by comparable mobilities.

^{31}P MAS NMR spectra of the reaction mixture were obtained at different stages of thermal ring-opening polymerization of hexachlorocyclotriphosphazene in order to monitor the polymerization process. It was determined that heating of the starting material at 250ºC for 17.5 h causes most of the cyclic low molecular weight phosphazenes to convert to various poly(dichlorophosphazene) species of different chain lengths. Formation of the trace amounts of the higher member cyclic species was also observed during earlier stages of the polymerization. This can be potentially employed for determining the quantitative rates of the cyclic phosphazenes depletion, chain propagation, branching and cross-linking.

A mixture of the partially phenoxy-substituted hexachlorocyclotriphosphazene was prepared as a model sample to test the two-dimensional ^{31}P – ^{31}P RFDR and INADEQUATE NMR experiments that were subsequently applied to polymers of interest.

The 2D ^{31}P RFDR and INADEQUATE homonuclear experiments were applied to the partially trifluoroethoxy-substituted poly(dichlorophosphazene). Ten components were identified in both spectra and were preliminarily assigned to the fully substituted poly(dichlorophosphazene), partially substituted poly(dichlorophosphazene), cyclic phosphazenes of different sizes and the partially substituted cyclic species. It was noted that the high resolution in the direct dimension of the RFDR and INADEQUATE spectra was attributed to low molecular weight species rather than long polymer chains.

Molecular motion in the polymer entered a regime where the fast quadrupolar relaxation in the nitrogen was effectively transferred to phosphorous through scalar coupling, leading to very short T_2's for ^{31}P. For the low molecular weight species the quadrupolar relaxation rate greatly exceeds the scalar coupling and hence quenched this relaxation process for ^{31}P leading to longer T_2's. As a result, the signals of the higher molecular weight species are broad, characterized by T_2's that are too short to allow for significant coherence buildup required in 2D experiments. Despite this limitation the two-dimensional methods proved very useful in determining the detailed connectivities and spatial conformations within the polymer, as the low molecular weight species should have significant structure features in common with their larger counter parts.

REFERENCES

1. Encyclopedia of Nuclear Magnetic Resonance. Grant, D. M.; Harris, R. K., Eds. Wiley: 2002.
2. Levitt, M. H., *Spin Dynamics : Basics of Nuclear Magnetic Resonance*. 2 ed.; John Wiley & Sons Ltd: 2008.
3. Duer, M. J., *Solid-state NMR spectroscopy principles and applications*. Blackwell Science: Malden, Mass., 2002; p xvii, 567 p.
4. Raleigh, D. P.; Levitt, M. H.; Griffin, R. G., *Chemical Physics Letters* **1988,** *146* (1-2), 71-76.
5. Pan, Y.; Gullion, T.; Schaefer, J., *Journal of Magnetic Resonance* **1990,** *90* (2), 330-340.
6. Tycko, R.; Dabbagh, G., *Chemical Physics Letters* **1990,** *173* (5-6), 461-465.
7. Bennett, A. E.; Ok, J. H.; Griffin, R. G.; Vega, S., *Journal of Chemical Physics* **1992,** *96* (11), 8624-8627.
8. Samoson, A.; Tuherm, T.; Gan, Z., *Solid State Nuclear Magnetic Resonance* **2001,** *20* (3-4), 130-136.
9. Andrew, E. R.; Bradbury, A.; Eades, R. G., *Nature* **1958,** *182* (4650), 1659-1659.
10. Lowe, I. J., *Physical Review Letters* **1959,** *2* (7`), 285-287.
11. Schaefer, J.; Stejskal, E. O., *Journal of the American Chemistry Society* **1976,** *98* (4), 1031-1032.
12. Bennett, A. E.; Rienstra, C. M.; Auger, M.; Lakshmi, K. V.; Griffin, R. G., *Journal of Chemical Physics* **1995,** *103* (16), 6951-6958.
13. Gullion, T.; Baker, D. B.; Conradi, M. S., *Journal of Magnetic Resonance* **1990,** *89* (3), 479-484.
14. Liu, S. F.; Schmidt-Rohr, K., *Macromolecules* **2001,** *34* (24), 8416-8418.
15. Borisov, A. S.; Hazendonk, P.; Hayes, P. G., *Journal of Inorganic and Organometallic Polymers and Materials* **2008,** *18* (1), 163-174.
16. Yannoni, C. S., *Accounts of Chemical Research* **1982,** *15* (7), 201-208.
17. Redfield, A. G., *Physical Review* **1955,** *98* (6), 1787-1809.
18. Connor, T. M., *NMR, Basic Principles and Progress*. Springer-Verlag: New York, 1971; Vol. 4.
19. Lyerla, J. R.; Yannoni, C. S.; Fyfe, C. A., *Journal of the American Chemistry Society* **1982,** *15* (7), 208-216.
20. Spiess, H. W., *Abstracts of Papers of the American Chemical Society* **1991,** *202*, 137-PHYS.
21. Pelczer, I.; Szalma, S., *Chemical Reviews* **1991,** *91* (7), 1507-1524.
22. Blumich, B., *Molecular Physics* **1983,** *48* (5), 969-980.
23. Blumich, B.; Ziessow, D., *Journal of Magnetic Resonance* **1983,** *52* (1), 42-56.
24. Manassen, Y.; Navon, G.; Moonen, C. T. W., *Journal of Magnetic Resonance* **1987,** *72* (3), 551-555.
25. Griesinger, C.; Bruschweiler, R.; Madi, Z. L.; Sorensen, O. W.; Ernst, R. R., *Makromolekulare Chemie-Macromolecular Symposia* **1990,** *34*, 17-31.
26. Geen, H.; Freeman, R., *Journal of Magnetic Resonance* **1990,** *87* (2), 415-421.

27. Kessler, H.; Mronga, S.; Gemmecker, G., *Magnetic Resonance in Chemistry* **1991,** *29* (6), 527-557.
28. Marigheto, N.; Venturi, L.; Hibberd, D.; Wright, K. M.; Ferrante, G.; Hills, B. P., *Journal of Magnetic Resonance* **2007,** *187* (2), 327-342.
29. Lescop, E.; Schanda, P.; Rasia, R.; Brutscher, B., *Journal of the American Chemical Society* **2007,** *129* (10), 2756-2757.
30. Kupce, E.; Freeman, R., *Magnetic Resonance in Chemistry* **2007,** *45* (1), 2-4.
31. Baskaran, K.; Kirchhofer, R.; Huber, F.; Trenner, J.; Brunner, K.; Gronwald, W.; Neidig, K. P.; Kalbitzer, H. R., *Journal of Biomolecular NMR* **2009,** *43* (4), 197-210.
32. Bax, A.; Freeman, R.; Kempsell, S. P., *Journal of American Chemical Society* **1980,** *102* (14), 4849-4851.
33. Bennett, A. E.; Ok, J. H.; Griffin, R. G.; Vega, S., *Journal of Chemical Physics* **1992,** *96* (11).
34. Mark, J. E.; Allcock, H. R.; West, R., *Inorganic Polymers*. Oxford University Press: New York, 2004.
35. Pitcher, M. W.; Arslan, Y.; Edinc, P.; Kartal, M., *Phosphorous, Sulfur, and Silicon* **2007,** *182* (12), 2861-2880.
36. Rahimi, A., *Iranian Polymer Journal* **2004,** *13* (2), 149-164.
37. Chojnowski, J.; Cypryk, M.; Kurjata, J., *Progress in Polymer Science* **2003,** *28* (5), 691-728.
38. Rahimi, A., *Iranian Polymer Journal* **2004,** *13* (2), 149-164.
39. Sheats, J. E.; Carraher, C. E.; Pittmann, C. U.; Zeldin, M., *Macromolecular Symposia* **2000,** *156*, 79-85.
40. Mustafa, A.; Achilleos, M.; Ruiz-Iban, J.; Davies, J.; Benfield, R. E.; Jones, R. G.; Grandjean, D.; Holder, S. J., *Reactive & Functional Polymers* **2006,** *66* (1), 123-135.
41. Sacarescu, L.; Ardeleanu, R., *High Performance Polymers* **2007,** *19* (5-6), 501-509.
42. Zhou, J. G.; Addison, A.; He, Z., *Material Design* **2005,** *26* (270).
43. Rahimi, A., *International Journal of Inorganic Materials* **2001,** *3* (7), 843-847.
44. Jamshidi, H.; Rahimi A., *Phosphorous, Sulfur, and Silicon* **2006,** *181* (11), 2565-2576.
45. Lanian, S. Y., *Med. Prog. Through Technol.* **1992,** *18* (2), 134-135.
46. Xia, Y.; Whitesides, G. M., *Angew. Chem.* **1998,** *37* (5), 551-575.
47. Shah, K.; Shin, W. C., *Sens. Actuators* **2004,** *97* (2-3), 157-167.
48. Abd-El-Aziz, A. S.; Todd, E. K., *Coordination Chemistry Reviews* **2003,** *246* (1-2), 3-52.
49. Abd-El-Aziz, A. S.; Pereira, N. M.; Boraie, W.; Todd, E. K.; Afifi, T. H.; Budakowski, W. R.; Friesen, K. J., *Journal of Inorganic and Organometallic Polymers and Materials* **2005,** *15* (4), 497-509.
50. Abd-El-Aziz, A. S.; Okasha, R. M.; Todd, E. K.; Afifi, T. H.; Shipman, P. O.; Copping, K. M. D., *Macromolecular Symposia* **2004,** *209*, 185-193.
51. Abd-El-Aziz, A. S.; Okasha, R. M.; Afifi, T. H., *Macromolecular Symposia* **2004,** *209*, 195-205.

52. Abd-El-Aziz, A. S.; Carruthers, S. A.; Todd, E. K.; Afifi, T. H.; Gavina, J. M. A., *Journal of Polymer Science Part a-Polymer Chemistry* **2005,** *43* (7), 1382-1396.
53. de Denus, C. R.; Hoffa, L.; Abd-El-Aziz, A. S.; Todd, E., *Abstracts of Papers of the American Chemical Society* **2000,** *219*, U396-U396.
54. Abd-El-Aziz, A. S.; Todd, E. K.; de Denus, C. R.; Dembek, A. A.; Fagan, P. J., *Abstracts of Papers of the American Chemical Society* **1999,** *218*, U470-U470.
55. Abd-El-Aziz, A. S.; McFarlane, S. L., *Abstracts of Papers of the American Chemical Society* **2001,** *222*, U581-U582.
56. Abd-El-Aziz, A. S.; Carraher, C. E.; Pittman, C. U.; Sheats, J. E.; Zeldin, M., *Abstracts of Papers of the American Chemical Society* **2002,** *223*, D88-D88.
57. Abd-El-Aziz, A. S., *Macromolecular Rapid Communications* **2002,** *23* (17), 995-1031.
58. Abd-El-Aziz, A. S.; Corkery, T. C.; Todd, E. K.; Afifi, T. H.; Ma, G. Z., *Journal of Inorganic and Organometallic Polymers* **2003,** *13* (3), 113-130.
59. Abd-El-Aziz, A. S.; Carraher, C. E.; Pittman, C. U.; Zeldin, M.; Sheats, J. E., *Abstracts of Papers of the American Chemical Society* **2005,** *230*, U3720-U3721.
60. Manners, I., *Macromolecular Symposia* **2003,** *196*, 57-62.
61. MacLachlan, M. J.; Manners, I.; Ozin, G. A., *Advanced Materials* **2000,** *12* (9), 675-+.
62. Manners, I., *Chemical Communications* **1999,** (10), 857-865.
63. Manners, I., *Chemistry in Britain* **1996,** *32* (1), 46-49.
64. Manners, I., *Angewandte Chemie-International Edition in English* **1996,** *35* (15), 1603-1621.
65. Manners, I., *Phosphorus Sulfur and Silicon and the Related Elements* **1994,** *93* (1-4), 143-151.
66. Foucher, D. A.; Petersen, R.; Tang, B. Z.; Ziembinski, R.; Coombs, N.; Macdonald, P. M.; Sodhi, R. N. S.; Massey, J.; Vancso, G. J.; Manners, I., *Abstracts of Papers of the American Chemical Society* **1993,** *205*, 314-POLY.
67. Foucher, D. A.; Manners, I., *Makromolekulare Chemie-Rapid Communications* **1993,** *14* (2), 63-66.
68. Soto, A. P.; Manners, I., *Macromolecules* **2009,** *42* (1), 40-42.
69. Meyers, R. A., Encyclopedia of Physical Science and Technology. 3rd ed.; Academic Press: 2001; Vol. 3.
70. Allcock, H. R.; Cook, W. J., *Macromolecules* **1974,** *7* (3), 284-290.
71. Schmutz, J. L.; Allcock, H. R., *Inorganic Chemistry* **1975,** *14* (10), 2433-2438.
72. Allcock, H. R.; Austin, P. E.; Neenan, T. X., *Macromolecules* **1982,** *15* (3), 689-693.
73. Allcock, H. R.; Neenan, T. X.; Kossa, W. C., *Macromolecules* **1982,** *15* (3), 693-696.
74. Allcock, H. R., *Journal of Polymer Science-Polymer Symposia* **1983,** (70), 71-77.
75. Blonsky, P. M.; Shriver, D. F.; Austin, P.; Allcock, H. R., *Journal of the American Chemical Society* **1984,** *106* (22), 6854-6855.
76. Blonsky, P. M.; Shriver, D. F.; Austin, P.; Allcock, H. R., *Abstracts of Papers of the American Chemical Society* **1985,** *190* (Sep), 25-PME.
77. Allcock, H. R.; Neenan, T. X.; Boso, B., *Inorganic Chemistry* **1985,** *24* (17), 2656-2662.

78. Tonge, J. S.; Blonsky, P. M.; Shriver, D. F.; Allcock, H. R.; Austin, P. E.; Neenan, T. X.; Sisko, J. T., *Journal of the Electrochemical Society* **1986,** *133* (8), C293-C293.
79. Dubois, R. A.; Garrou, P. E.; Lavin, K. D.; Allcock, H. R., *Organometallics* **1986,** *5* (3), 460-466.
80. Blonsky, P. M.; Shriver, D. F.; Austin, P.; Allcock, H. R., *Solid State Ionics* **1986,** *18-9*, 258-264.
81. Laurencin, C. T.; Koh, H. J.; Neenan, T. X.; Allcock, H. R.; Langer, R., *Journal of Biomedical Materials Research* **1987,** *21* (10), 1231-1246.
82. Tonge, J. S.; Shriver, D. F.; Blonsky, P. M.; Chengming, L.; Allcock, H. R.; Austin, P. E.; Neenan, T. X.; Sisko, J. T., *Abstracts of Papers of the American Chemical Society* **1987,** *193*, 72-ANYL.
83. Allcock, H. R., *Abstracts of Papers of the American Chemical Society* **1987,** *193*, 228-INOR.
84. Allcock, H. R., *Acs Symposium Series* **1988,** *360*, 250-267.
85. Allcock, H. R., *Current Opinion in Solid State & Materials Science* **2006,** *10* (5-6), 231-240.
86. Gleria, M.; Bertani, R.; De Jaeger, R., *Journal of Inorganic and Organometallic Polymers* **2004,** *14* (1), 1-28.
87. Honeyman, C. H.; Manners, I.; Morrissey, C. T.; Allcock, H. R., *Journal of the American Chemical Society* **1995,** *117* (26), 7035-7036.
88. Schneider, N. S., *Liquid Crystalline Order in Polymers*. Academic Press: New York, 1978.
89. Allcock, H. R.; Kugel, R. L.; Valan, J. K., *Inorganic Chemistry* **1966,** *5* (10).
90. Wang, B.; Rivard, E.; Manners, I., *Inorganic Chemistry* **2001,** *41* (7), 1690-1691.
91. Rivard, E.; Lough, A. J.; Manners, I., *Inorganic Chemistry* **2004,** *43* (9), 2765-2767.
92. Gleria, M.; De Jaeger, R., Polyphosphazenes: A review. In *New Aspects in Phosphorus Chemistry V*, Springer-Verlag Berlin: Berlin, 2005; Vol. 250, pp 165-251.
93. Allcock, H. R.; Reeves, S. D.; Nelson, J. M.; Crane, C. A.; Manners, I., *Macromolecules* **1997,** *30* (7), 2213-2215.
94. Singler, R. E.; Hagnauer, G. L.; Sicka, R. W., *Acs Symposium Series* **1982,** *193*, 229-242.
95. Abraham, K. M.; Alamgir, M.; Perrotti, S. J., *Journal of the Electrochemical Society* **1988,** *135* (2), 535-536.
96. Lora, S.; Carenza, M.; Palma, G.; Pezzin, G.; Caliceti, P.; Battaglia, P.; Lora, A., *Biomaterials* **1991,** *12* (3), 275-280.
97. Peterson, E. S.; Stone, M. L.; Mccaffrey, R. R.; Cummings, D. G., *Abstracts of Papers of the American Chemical Society* **1991,** *202*, 70-INOR.
98. Crommen, J. H. L.; Schacht, E. H.; Mense, E. H. G., *Biomaterials* **1992,** *13* (9), 601-611.
99. Crommen, J. H. L.; Schacht, E. H.; Mense, E. H. G., *Biomaterials* **1992,** *13* (8), 511-520.
100. Schacht, E.; Crommen, J.; Vandorpe, J., *Abstracts of Papers of the American Chemical Society* **1992,** *203*, 17-CELL.

101. Crommen, J.; Vandorpe, J.; Schacht, E., *Journal of Controlled Release* **1993,** *24* (1-3), 167-180.
102. Landry, C. J. T.; Ferrar, W. T.; Teegarden, D. M.; Coltrain, B. K., *Macromolecules* **1993,** *26* (1), 35-46.
103. Laurencin, C. T.; Norman, M. E.; Elgendy, H. M.; Elamin, S. F.; Allcock, H. R.; Pucher, S. R.; Ambrosio, A. A., *Journal of Biomedical Materials Research* **1993,** *27* (7), 963-973.
104. Allcock, H. R., Macromolecular and Materials Design Using Polyphosphazenes. In *Inorganic and Organometallic Polymers Ii*, 1994; Vol. 572, pp 208-231.
105. Allcock, H. R., *Chemistry of Materials* **1994,** *6* (9), 1476-1491.
106. Allcock, H. R., *Advanced Materials* **1994,** *6* (2), 106-115.
107. Peterson, E. S.; Stone, M. L.; Orme, C. J.; Reavill, D. A., *Separation Science and Technology* **1995,** *30* (7-9), 1573-1587.
108. Allcock, H. R., Water-soluble polyphosphazenes and their hydrogels. In *Hydrophilic Polymers*, 1996; Vol. 248, pp 3-29.
109. Anchisini, R.; Faglia, G.; Gallazzi, M. C.; Sberveglieri, G.; Zerbi, G., *Sensors and Actuators B-Chemical* **1996,** *35* (1-3), 99-102.
110. Golemme, G.; Drioli, E., *Journal of Inorganic and Organometallic Polymers* **1996,** *6* (4), 341-365.
111. Schacht, E.; Vandorpe, J.; Dejardin, S.; Lemmouchi, Y.; Seymour, L., *Biotechnology and Bioengineering* **1996,** *52* (1), 102-108.
112. Allcock, H. R., *Bioartificial Organs* **1997,** *831*, 13-31.
113. Orme, C. J.; Stewart, F. F.; Peterson, E. S.; Stone, M. L., *Abstracts of Papers of the American Chemical Society* **1997,** *213*, 2-TECH.
114. Peterson, E. S.; Stone, M. L.; Orme, C. J.; Stewart, F. F.; Cowan, R. L., *Separation Science and Technology* **1997,** *32* (1-4), 541-556.
115. Allcock, H. R., *Applied Organometallic Chemistry* **1998,** *12* (10-11), 659-666.
116. Graves, R.; Pintauro, P. N., *Journal of Applied Polymer Science* **1998,** *68* (5), 827-836.
117. Caliceti, P.; Veronese, F. M.; Lora, S., *International Journal of Pharmaceutics* **2000,** *211* (1-2), 57-65.
118. Chen-Yang, Y. W.; Hwang, J. J.; Huang, A. Y., *Macromolecules* **2000,** *33* (4), 1237-1244.
119. Kawakami, H.; Kanezaki, S.; Sudo, M.; Kanno, M.; Nagaoka, S.; Kubota, S., *Artificial Organs* **2002,** *26* (10), 883-890.
120. Lakshmi, S.; Katti, D. S.; Laurencin, C. T., *Advanced Drug Delivery Reviews* **2003,** *55* (4), 467-482.
121. Lvov, S. N.; Allcock, H. R.; Ambler, C. M.; Maher, A. E.; Zhou, X. Y. Y.; Chalkova, E.; Weston, J. A., *Abstracts of Papers of the American Chemical Society* **2003,** *225*, U878-U878.
122. Patat, F.; Kollinsky, F., *Makromolekulare Chemie-Macromolecular Symposia* **1951,** *6* (MAR), 292-317.
123. Knoesel, R.; Parrod, J., *Comp. Rend.* **1960,** *251* (25), 2944-2946.
124. Breza, M., *European Polymer Journal* **1998,** *135* (6), 931-940.
125. Allcock, H. R.; Kugel, R. L., *Inorganic Chemistry* **1972,** *11* (5), 1120-1125.

126. Gleria, M.; Bertani, R.; De Jaeger, R.; Lora, S., *Journal of Fluorine Chemistry* **2004,** *125* (2), 329-337.
127. Antipov, E. M.; Kulichikhin, V. G., *Vysokomolek. Soedin.* **1990,** *32* (1), 108-115.
128. Golemme, G., *Journal of Inorganic and Organometallic Polymers* **1996,** *6* (4), 341-365.
129. Wade, C. W. R.; Gourlay, S., *Organometallic Polymers*. Academic Press: New York, 1978.
130. Desper, C. R.; Schneider, N. S., *Bulletin of the American Physical Society* **1976,** *21* (3), 445-445.
131. Alexander, M. N.; Desper, C. R.; Sagalyn, P. L.; Schneider, N. S., *Macromolecules* **1977,** *10* (3), 721-723.
132. Vega, A. J.; English, A. D., *Macromolecules* **1980,** *13* (6), 1635-1647.
133. Kojima, M.; Magill, J. H., *Polymer Communications* **1983,** *24* (11), 329-331.
134. Ritchey, W. M., *Abstracts of Papers of the American Chemical Society* **1984,** *187* (APR), 193-POLY.
135. Ferrar, W. T.; Marshall, A. S., *Abstracts of Papers of the American Chemical Society* **1985,** *190* (Sep), 54-POY.
136. Ferrar, W. T.; Marshall, A. S.; Whitefield, J., *Macromolecules* **1987,** *20* (2), 317-322.
137. Veregin, R. P.; Marchessault, R. H.; Fyfe, C. A., *Abstracts of Papers of the American Chemical Society* **1988,** *195*, 208-POLY.
138. Gomez, M. A.; Marco, C.; Fatou, J. G.; Chichesterhicks, S. V.; Haddon, R. C., *Polymer Communications* **1990,** *31* (8), 308-312.
139. Tonelli, A. E.; Gomez, M. A.; Tanaka, H.; Schilling, F. C.; Cozine, M. H.; Lovinger, A. J.; Bovey, F. A., *Advances in Chemistry Series* **1990,** (227), 409-451.
140. Abraham, K. M.; Alamgir, M.; Moulton, R. D., *Journal of the Electrochemical Society* **1991,** *138* (4), 921-927.
141. Mujumdar, A. N.; Kojima, M.; Young, S. G.; Chan, E. K.; Magill, J. H., *Polymer Engineering and Science* **1991,** *31* (10), 743-752.
142. Tzou, D. L.; Huang, T. H.; Saraf, A. W.; Desai, P.; Abhiraman, A. S., *Abstracts of Papers of the American Chemical Society* **1991,** *201*, 215-PMSE.
143. Coltrain, B. K.; Ferrar, W. T.; Landry, C. J. T.; Molaire, T. R.; Zumbulyadis, N., *Chemistry of Materials* **1992,** *4* (2), 358-364.
144. Schmidtrohr, K.; Clauss, J.; Spiess, H. W., *Macromolecules* **1992,** *25* (12), 3273-3277.
145. Takegoshi, K.; Tanaka, I.; Hikichi, K.; Higashida, S., *Macromolecules* **1992,** *25* (13), 3392-3398.
146. Taylor, S. A.; White, J. L.; Elbaum, N. C.; Crosby, R. C.; Campbell, G. C.; Haw, J. F.; Hatfield, G. R., *Macromolecules* **1992,** *25* (13), 3369-3376.
147. Maunu, S. L.; Rinne, H.; Sundholm, R. F. R., *Macromolecular Chemistry and Physics* **1994,** *195* (11), 3735-3745.
148. Miyata, T.; Masuko, T.; Kojima, M.; Magill, J. H., *Macromolecular Chemistry and Physics* **1994,** *195* (1), 253-261.
149. Kojima, M.; Magill, J. H.; White, M. L.; Matyjaszewski, K., *Macromolecular Chemistry and Physics* **1995,** *196* (5), 1713-1737.

150. Nakamura, H.; Kojima, M.; Masuko, T., *Nippon Kagaku Kaishi* **1996,** (8), 706-713.
151. Pivin, J. C.; Brusatin, G.; Guglielmi, M.; Facchin, G.; Gleria, M., *Nuclear Instruments & Methods in Physics Research Section B-Beam Interactions with Materials and Atoms* **1996,** *112* (1-4), 294-297.
152. Simonutti, R.; Comotti, A.; Sozzani, P., *Journal of Inorganic and Organometallic Polymers* **1996,** *6* (4), 313-324.
153. Simonutti, R.; Veeman, W. S.; Ruhnau, F. C.; Gallazzi, M. C.; Sozzani, P., *Macromolecules* **1996,** *29* (14), 4958-4962.
154. Battiste, J.; Newmark, R. A., *Progress in Nuclear Magnetic Resonance Spectroscopy* **2006,** *48* (1), 1-23.
155. Rocha, J.; Morais, C. M.; Fernandez, C., Progress in multiple-quantum magic-angle spinning NMR spectroscopy. In *New Techniques in Solid-State Nmr*, 2005; Vol. 246, pp 141-194.
156. Ramamoorthy, A.; Wu, C. H.; Opella, S. J., *Journal of Magnetic Resonance* **1999,** *140* (1), 131-140.
157. Harris, D. J.; Bonagamba, T. J.; Hong, M.; Schmidt-Rohr, K., *Macromolecules* **2000,** *33* (9), 3375-3381.
158. Fayon, F.; Le Saout, G.; Emsley, L.; Massiot, D., *Chemical Communications* **2002,** (16), 1702-1703.
159. Fayon, F.; King, I. J.; Harris, R. K.; Evans, J. S. O.; Massiot, D., *Comptes Rendus Chimie* **2004,** *7* (3-4), 351-361.
160. Wormald, P.; Apperley, D. C.; Beaume, F.; Harris, R. K., *Polymer* **2003,** *44* (3), PII S0032-3861(02)00821-2.
161. Kanehashi, K.; Nemoto, T.; Saito, K., *Journal of Non-Crystalline Solids* **2007,** *353* (44-46), 4227-4231.
162. Fu, R.; Truong, M.; Saager, R. J.; Cotten, M.; Cross, T. A., *Journal of Magnetic Resonance* **2007,** *188* (1), 41-48.
163. Luliucci, R.; Taylor, C.; Hollis, W. K., *Magnetic Resonance in Chemistry* **2006,** *44* (3), 375-384.
164. Bose, A. B.; Gangoda, M.; Jaroniec, M.; Gilpin, R. K.; Bose, R. N., *Surface Science* **2006,** *600* (1), 143-154.
165. Porbeni, F. E.; Shin, I. D.; Shuai, X. T.; Wang, X. W.; White, J. L.; Jia, X.; Tonelli, A. E., *Journal of Polymer Science Part B-Polymer Physics* **2005,** *43* (15), 2086-2096.
166. Huang, Y. N.; Yan, Z. M., *Journal of the American Chemical Society* **2005,** *127* (8), 2731-2740.
167. Murata, K.; Kono, H.; Katoh, E.; Kuroki, S.; Ando, I., *Polymer* **2003,** *44* (14), 4021-4027.
168. Hou, S. S.; Bonagamba, T. J.; Beyer, F. L.; Madison, P. H.; Schmidt-Rohr, K., *Macromolecules* **2003,** *36* (8), 2769-2776.
169. Masuda, K.; Kaji, H.; Horii, F., *Polymer Journal* **2001,** *33* (2), 190-198.
170. White, J. L.; Mirau, P. A., *Macromolecules* **1994,** *27* (6), 1648-1650.
171. Li, S.; Rice, D. M.; Karasz, F. E., *Macromolecules* **1994,** *27* (8), 2211-2218.
172. Kaplan, S., *Macromolecules* **1993,** *26* (5), 1060-1064.

173. Bielecki, A.; Burum, D. P.; Rice, D. M.; Karasz, F. E., *Macromolecules* **1991,** *24* (17), 4820-4822.
174. Bax, A.; Summers, M. F., *Journal of the American Chemical Society* **1986,** *108* (8), 2093-2094.
175. Lesage, A.; Emsley, L., *Journal of Magnetic Resonance* **2001,** *148* (2), 449-454.
176. Ando, I.; Asakura, T., Solid State NMR of Polymers. In *Studies in Physical and Theoretical Chemistry*, Elsevier: New York, 1998; Vol. 84.
177. Schmidtrohr, K., *Abstracts of Papers of the American Chemical Society* **1994,** *208*, 111-PMSE.
178. Zhu, B.; Kai, W. H.; Pan, P. J.; Yazawa, K.; Nishida, H.; Sakurai, M.; Inoue, Y., *Journal of Physical Chemistry B* **2008,** *112* (32), 9684-9692.
179. Tatsuno, H.; Koseki, Y.; Ando, S., *Polymer* **2008,** *49* (11), 2709-2716.
180. Le Bouch, N.; Auger, M.; Leclerc, M., *Macromolecular Chemistry and Physics* **2008,** *209* (24), 2455-2462.
181. Gandhi, S.; Melian, C.; Demco, D. E.; Brar, A. S.; Blumich, B., *Macromolecular Chemistry and Physics* **2008,** *209* (15), 1576-1585.
182. Zhang, L. M.; Tang, H. R.; Hou, G. J.; Shen, Y. D.; Deng, F., *Polymer* **2007,** *48* (10), 2928-2938.
183. Yao, Y. F.; Graf, R.; Spiess, H. W.; Lippits, D. R.; Rastogi, S., *Physical Review E* **2007,** *76* (6), 060801.
184. Wickham, J. R.; Mason, R. N.; Rice, C. V., *Solid State Nuclear Magnetic Resonance* **2007,** *31* (4), 184-192.
185. Wang, M. T.; Bernard, G. M.; Wasylishen, R. E.; Choi, P., *Macromolecules* **2007,** *40* (18), 6594-6599.
186. Saalwachter, K., *Progress in Nuclear Magnetic Resonance Spectroscopy* **2007,** *51* (1), 1-35.
187. Gaborieau, M.; Graf, R.; Kahle, S.; Pakula, T.; Spiess, H. W., *Macromolecules* **2007,** *40*, 6249-6256.
188. Cypry, M., *Polimery* **2007,** *52*, 730-735.
189. Asano, A., *Kobunshi Ronbunshu* **2007,** *64* (7), 406-418.
190. Saito, H.; Ando, I.; Naito, A., *Solid State NMR Spectroscopy for Biopolymers: Principles and Applications* **2006**.
191. Odin, C., *Annual Reports on NMR Spectroscopy* **2006,** *59*, 117-205.
192. Miyayama, K.; Seki, T.; Iwahori, A.; Hiraoka, K., *Ferroelectrics* **2006,** *343*, 111-118.
193. Gabrielse, W.; Gaur, H. A.; Feyen, F. C.; Veeman, W. S., *Macromolecules* **1994,** *27* (20), 5811-5820.
194. Inoue, Y.; Miyauchi, M.; Nakajima, H.; Takashima, Y.; Yamaguchi, H.; Harada, A., *Macromolecules* **2007,** *40* (9), 3256-3262.
195. Weldeghiorghis, T. K.; Stueber, D.; Schaefer, J., *Journal of Polymer Science Part B-Polymer Physics* **2008,** *46* (11), 1062-1066.
196. Miyoshi, T.; Pascui, O.; Reichert, D., *Macromolecules* **2004,** *37* (17), 6460-6471.
197. Becker-Guedes, F.; deAzevedo, E. R.; Bonagamba, T. J.; Schmidt-Rohr, K., *Applied Magnetic Resonance* **2004,** *27* (3-4), 383-400.
198. Harris, D. J.; de Azevedo, E. R.; Bonagamba, T. J., *Journal of Magnetic Resonance* **2003,** *162* (1), 67-73.

199. Bovey, F. A.; Mirau, P. A., *NMR of Polymers*. Academic Press: San Diego, 1996.
200. Yoshie, N.; Azuma, Y.; Sakurai, M.; Inoue, Y., *Journal of Applied Polymer Science* **1995,** *56* (1), 17-24.
201. Egger, N.; Schmidtrohr, K.; Blumich, B.; Domke, W. D.; Stapp, B., *Journal of Applied Polymer Science* **1992,** *44* (2), 289-295.
202. Wilson, M. A.; Pugmire, R. J.; Karas, J.; Alemany, L. B.; Woolfenden, W. R.; Grant, D. M.; Given, P. H., *Analytical Chemistry* **1984,** *56* (6), 933-943.
203. Alemany, L. B.; Grant, D. M.; Pugmire, R. J.; Stock, L. M., *Fuel* **1984,** *63* (4), 513-521.
204. Alemany, L. B.; Grant, D. M.; Alger, T. D.; Pugmire, R. J., *Journal of the American Chemical Society* **1983,** *105* (22), 6697-6704.
205. Opella, S. J.; Frey, M. H.; Cross, T. A., *Journal of the American Chemical Society* **1979,** *101* (19), 5856-5857.
206. Opella, S. J.; Frey, M. H., *Journal of the American Chemical Society* **1979,** *101* (19), 5854-5856.
207. Nielsen, N. C.; Sangill, R.; Bildsoe, H.; Jakobsen, H. J., *Macromolecules* **1995,** *28* (6), 2009-2015.
208. Hazendonk, P.; Wormald, P.; Montina, T., *Journal of Physical Chemistry A* **2008,** *112* (28), 6262-6274.
209. Wormald, P.; Ameduri, B.; Harris, R. K.; Hazendonk, P., *Solid State Nuclear Magnetic Resonance* **2006,** *30* (2), 114-123.
210. Hazendonk, P.; Harris, R. K.; Ando, S.; Avalle, P., *Journal of Magnetic Resonance* **2003,** *162* (1), 206-216.
211. Ando, S.; Harris, R. K.; Reinsberg, S. A., *Magnetic Resonance in Chemistry* **2002,** *40* (2), 97-106.
212. Ando, S.; Harris, R. K.; Holstein, P.; Reinsberg, S. A.; Yamauchi, K., *Polymer* **2001,** *42* (19), 8137-8151.
213. Caravatti, P.; Neuenschwander, P.; Ernst, R. R., *Macromolecules* **1985,** *18* (1), 119-122.
214. Caravatti, P.; Neuenschwander, P.; Ernst, R. R., *Macromolecules* **1986,** *19* (7), 1889-1895.
215. Assink, R. A., *Macromolecules* **1978,** *11* (6), 1233-1237.
216. Cheung, T. T. P.; Gerstein, B. C., *Journal of Applied Physics* **1981,** *52* (9), 5517-5528.
217. Cheung, T. T. P.; Gerstein, B. C.; Ryan, L. M.; Taylor, R. E.; Dybowski, D. R., *Journal of Chemical Physics* **1980,** *73* (12), 6059-6067.
218. Douglass, D. C.; Jones, G. P., *Journal of Chemical Physics* **1966,** *45* (3), 956-961.
219. Lind, A. C., *Journal of Chemical Physics* **1977,** *66* (8), 3483-3490.
220. McBrierty, V. J.; Douglass, D. C.; Kwei, T. K., *Macromolecules* **1978,** *11* (6), 1265-1267.
221. McCall, D. W.; Douglass, D. C., *Polymer* **1963,** *4* (4), 433-444.
222. Obrien, J.; Cashell, E.; Wardell, G. E.; McBrierty, V. J., *Macromolecules* **1976,** *9* (4), 653-660.
223. Obrien, J.; Cashell, E.; Wardell, G. E.; McBrierty, V. J., *Rubber Chemistry and Technology* **1977,** *50* (4), 747-764.

224. Vanderhart, D. L., *Makromolekulare Chemie-Macromolecular Symposia* **1990,** *34*, 125-159.
225. Vanderhart, D. L.; Manders, W. M.; Campbell, G. C., *Abstracts of Papers of the American Chemical Society* **1990,** *200*, 39-PETR.
226. Goldman, M.; Shen, L., *Physical Review* **1966,** *144* (1), 321-326.
227. Clauss, J.; Schmidtrohr, K.; Adam, A.; Boeffel, C.; Spiess, H. W., *Macromolecules* **1992,** *25* (20), 5208-5214.
228. Schmidtrohr, K.; Clauss, J.; Blumich, B.; Spiess, H. W., *Magnetic Resonance in Chemistry* **1990,** *28*, S3-S9.
229. Schmidtrohr, K.; Clauss, J.; Blumich, B.; Spiess, H. W., *Abstracts of Papers of the American Chemical Society* **1990,** *199*, 284-POLY.
230. Meurer, B.; Weill, G., *Macromolecular Chemistry and Physics* **2008,** *209* (2), 212-219.
231. Wang, L. Y.; Fang, P. F.; Ye, C. H.; Feng, J. W., *Journal of Polymer Science Part B-Polymer Physics* **2006,** *44* (19), 2864-2879.
232. deAzevedo, E. R.; Bonagamba, T. J., *Brazilian Journal of Physics* **2006,** *36* (1A), 61-74.
233. Buda, A. A.; Demco, D. E.; Bertmer, M.; Blumich, B., *Comptes Rendus Chimie* **2006,** *9* (3-4), 346-356.
234. Bertmer, M.; Demco, D. E.; Wang, M.; Melian, C.; Marcean-Chelcea, R. I.; Fechete, R.; Baias, M.; Blumich, B., *Chemical Physics Letters* **2006,** *431* (4-6), 404-409.
235. Jia, X.; Wang, X. W.; Tonelli, A. E.; White, J. L., *Macromolecules* **2005,** *38* (7), 2775-2780.
236. Hucher, C.; Eustache, R. P.; Beaume, F.; Tekely, P., *Macromolecules* **2005,** *38* (22), 9200-9209.
237. Cherry, B. R.; Fujimoto, C. H.; Cornelius, C. J.; Alam, T. M., *Macromolecules* **2005,** *38* (4), 1201-1206.
238. Thurecht, K. J.; Hill, D. J. T.; Preston, C. M. L.; Rintoul, L.; White, J. W.; Whittaker, A. K., *Macromolecules* **2004,** *37* (16), 6019-6026.
239. Kurosu, H.; Chen, Q., Structural studies of polymer blends by solid-state NMR. In *Advances in Solid State Nmr Studies of Materials and Polymers: A Special Volume Dedicated to Isao Ando*, 2004; Vol. 52, pp 167-200.
240. Werkhoven, T. M.; Mulder, F. M.; Zune, C.; Jerome, R.; de Groot, H. J. M., *Macromolecular Chemistry and Physics* **2003,** *204* (1), 46-51.
241. Cojocariu, G.; Natansohn, A., *Macromolecules* **2003,** *36* (7), 2404-2411.
242. Buda, A.; Demco, D. E.; Bertmer, M.; Blumich, B.; Reining, B.; Keul, H.; Hocker, H., *Solid State Nuclear Magnetic Resonance* **2003,** *24* (1), 39-67.
243. Buda, A.; Demco, D. E.; Bertmer, M.; Blumich, B.; Litvinov, V. M.; Penning, J. P., *Journal of Physical Chemistry B* **2003,** *107* (22), 5357-5370.
244. Shim, S. E.; Parr, J. C.; von Meerwall, E.; Isayev, A. I., *Journal of Physical Chemistry B* **2002,** *106* (46), 12072-12078.
245. Mirau, P. A.; Yang, S., *Chemistry of Materials* **2002,** *14* (1), 249-255.
246. Kretschmer, A.; Drake, R.; Neidhoefer, M.; Wilhelm, M., *Solid State Nuclear Magnetic Resonance* **2002,** *22* (2-3), 204-217.

247. Brus, J.; Dybal, J.; Sysel, P.; Hobzova, R., *Macromolecules* **2002,** *35* (4), 1253-1261.
248. Yu, H. S.; Natansohn, A.; Singh, M. A.; Torriani, I., *Macromolecules* **2001,** *34* (5), 1258-1266.
249. Ando, S.; Harris, R. K.; Hirschinger, J.; Reinsberg, S. A.; Scheler, U., *Macromolecules* **2001,** *34* (1), 66-75.
250. VanderHart, D. L.; Feng, Y.; Han, C. C.; Weiss, R. A., *Macromolecules* **2000,** *33* (6), 2206-2227.
251. Su, T. W.; Tzou, D. L. M., *Polymer* **2000,** *41* (19), 7289-7293.
252. Cheung, M. K.; Wang, J.; Zheng, S.; Mi, Y., *Polymer* **2000,** *41* (4), 1469-1474.
253. Brendler, E.; Jager, C.; Scheller, D.; Roewer, G., *Macromolecules* **2000,** *33* (22), 8371-8374.
254. Yu, H. S.; Natansohn, A.; Singh, M. A.; Plivelic, T., *Macromolecules* **1999,** *32* (22), 7562-7571.
255. Ishida, M.; Oshima, J.; Yoshinaga, K.; Horii, F., *Polymer* **1999,** *40* (12), 3323-3329.
256. Hu, W. G.; Zimmermann, H.; Schmidt-Rohr, K., *Applied Magnetic Resonance* **1999,** *17* (2-3), 197-209.
257. Holstein, P.; Monti, G. A.; Harris, R. K., *Physical Chemistry Chemical Physics* **1999,** *1* (15), 3549-3555.
258. Blumich, B.; Blumler, P.; Gasper, L.; Guthausen, A.; Gobbels, V.; Laukemper-Ostendorf, S.; Unseld, K.; Zimmer, G., *Macromolecular Symposia* **1999,** *141*, 83-93.
259. Mulder, F. M.; Heinen, W.; van Duin, M.; Lugtenburg, J.; de Groot, H. J. M., *Journal of the American Chemical Society* **1998,** *120* (49), 12891-12894.
260. Marjanski, M.; Srinivasarao, M.; Mirau, P. A., *Solid State Nuclear Magnetic Resonance* **1998,** *12* (2-3), 113-118.
261. Li, M.; Li, C. G.; Zhang, B. H.; Huang, W. Q.; Men, A. J.; He, B. L., *European Polymer Journal* **1998,** *34* (3-4), 515-521.
262. Kaji, H.; Horii, F., *Journal of Chemical Physics* **1998,** *109* (11), 4651-4658.
263. Wang, J. H.; Jack, K. S.; Natansohn, A. L., *Journal of Chemical Physics* **1997,** *107* (3), 1016-1020.
264. Schantz, S., *Macromolecules* **1997,** *30* (5), 1419-1425.
265. Geppi, M.; Ciardelli, F.; Veracini, C. A.; Forte, C.; Cecchin, G.; Ferrari, P., *Polymer* **1997,** *38* (23), 5713-5723.
266. Comotti, A.; Simonutti, R.; Sozzani, P., *Journal of Materials Science* **1997,** *32* (16), 4237-4245.
267. Clayden, N. J.; Nijs, C. L.; Eeckhaut, G. J., *Polymer* **1997,** *38* (5), 1011-1016.
268. Wong, S.; Vaia, R. A.; Giannelis, E. P.; Zax, D. B., *Solid State Ionics* **1996,** *86-8*, 547-557.
269. Weigand, F.; Demco, D. E.; Blumich, B.; Spiess, H. W., *Journal of Magnetic Resonance Series A* **1996,** *120* (2), 190-200.
270. Miyoshi, T.; Takegoshi, K.; Hikichi, K., *Polymer* **1996,** *37* (1), 11-18.
271. Guo, M. M., *Trends in Polymer Science* **1996,** *4* (7), 238-244.
272. Egawa, Y.; Imanishi, S.; Matsumoto, A.; Horii, F., *Polymer* **1996,** *37* (25), 5569-5575.

273. DuPrez, F. E.; Goethals, E. J.; Adriaensens, P. J.; Gelan, J. M.; Vanderzande, D. J. M., *Macromolecules* **1996,** *29* (11), 4000-4005.
274. Cosgrove, T.; Turner, M. J.; Griffiths, P. C.; Hollingshurst, J.; Shenton, M. J.; Semlyen, J. A., *Polymer* **1996,** *37* (9), 1535-1540.
275. Meille, S. V.; Farina, A.; Gallazzi, M. C.; Sozzani, P.; Simonutti, R.; Comotti, A., *Macromolecules* **1995,** *28* (6), 1893-1902.
276. Demco, D. E.; Johansson, A.; Tegenfeldt, J., *Solid State Nuclear Magnetic Resonance* **1995,** *4* (1), 13-38.
277. Chen, A.; Wu, D. H.; Johnson, C. S., *Journal of the American Chemical Society* **1995,** *117* (30), 7965-7970.
278. Wilhelm, M.; Lehmann, S.; Jager, C.; Spiess, H. W.; Jerome, R., *Magnetic Resonance in Chemistry* **1994,** *32*, S3-S7.
279. Takegoshi, K.; Hikichi, K., *Polymer Journal* **1994,** *26* (12), 1377-1380.
280. Chin, Y. H.; Kaplan, S., *Magnetic Resonance in Chemistry* **1994,** *32*, S53-S60.
281. Asano, A.; Takegoshi, K.; Hikichi, K., *Polymer* **1994,** *35* (26), 5630-5636.
282. Kelts, L. W.; Landry, C. J. T.; Teegarden, D. M., *Macromolecules* **1993,** *26* (11), 2941-2949.
283. Clauss, J.; Schmidtrohr, K.; Spiess, H. W., *Acta Polymerica* **1993,** *44* (1), 1-17.
284. Cai, W. Z.; Schmidtrohr, K.; Egger, N.; Gerharz, B.; Spiess, H. W., *Polymer* **1993,** *34* (2), 267-276.
285. Zhang, X. Q.; Takegoshi, K.; Hikichi, K., *Polymer Journal* **1992,** *24* (12), 1403-1407.
286. Hecht, A. M.; Guillermo, A.; Horkay, F.; Mallam, S.; Legrand, J. F.; Geissler, E., *Macromolecules* **1992,** *25* (14), 3677-3684.
287. Yu, J.; Zhang, Z. H.; Ni, Y.; Lu, Y. B.; Xiong, Y. Q.; Xu, W. J., *Acta Polymerica Sinica* **2007,** (1), 81-84.
288. Tatsuno, H.; Aimi, K.; Ando, S., *Magnetic Resonance in Chemistry* **2007,** *45* (5), 401-409.
289. Voda, M. A.; Demco, D. E.; Voda, A.; Schauber, T.; Adler, M.; Dabisch, T.; Adams, A.; Baias, M.; Blumich, B., *Macromolecules* **2006,** *39* (14), 4802-4810.
290. Pallathadka, P. K.; Tay, S. S.; Liu, T. X.; Sprenger, P., *Polymer Engineering and Science* **2006,** *46* (12), 1684-1690.
291. Lili, Z.; Chen, Q.; Hansen, E. W., *Macromolecular Chemistry and Physics* **2005,** *206* (2), 246-257.
292. Ando, S.; Harris, R. K.; Hazendonk, P.; Wormald, P., *Macromolecular Rapid Communications* **2005,** *26* (5), 345-356.
293. McElheny, D.; Grinshtein, J.; Frydman, V.; Frydman, L., *Macromolecules* **2002,** *35* (9), 3544-3552.
294. Matsuo, M.; Bin, Y.; Nakano, M., *Polymer* **2001,** *42* (10), 4687-4707.
295. McGrath, K. J.; Roland, C. M.; Antonietti, M., *Macromolecules* **2000,** *33* (22), 8354-8360.
296. Miller, J. B., *Journal of Thermal Analysis* **1997,** *49* (1), 521-524.
297. Thakur, K. A. M.; Kean, R. T.; Zupfer, J. M.; Buehler, N. U.; Doscotch, M. A.; Munson, E. J., *Macromolecules* **1996,** *29* (27), 8844-8851.
298. Feng, H. Q.; Ye, C. H.; Zhang, P.; Sun, Z. H.; Feng, Z. L., *Macromolecular Chemistry and Physics* **1995,** *196* (8), 2587-2600.

299. Roland, C. M.; Walton, J. H.; Miller, J. B., *Magnetic Resonance in Chemistry* **1994,** *32*, S36-S39.
300. Parker, A. A.; Marcinko, J. J.; Shieh, Y. T.; Shields, C.; Hedrick, D. P.; Ritchey, W. M., *Polymer Bulletin* **1989,** *21* (2), 229-234.
301. Packer, K. J.; Pope, J. M.; Yeung, R. R.; Cudby, M. E. A., *Journal of Polymer Science Part B-Polymer Physics* **1984,** *22* (4), 589-616.
302. Pratt, R. G.; Ackerman, J. L., *Abstracts of Papers of the American Chemical Society* **1983,** *186* (AUG), 61-PMSE.
303. Tanaka, H.; Gomez, M. A.; Tonelli, A. E.; Chichesterhicks, S. V.; Haddon, R. C., *Macromolecules* **1988,** *21* (7), 2301-2304.
304. Young, S. G.; Magill, J. H., *Macromolecules* **1989,** *22* (5), 2549-2551.
305. Young, S. G.; Kojima, M.; Magill, J. H.; Lin, F. T., *Polymer* **1992,** *33* (15), 3215-3225.
306. Allcock, H. R.; Cameron, C. G.; Skloss, T. W.; TaylorMeyers, S.; Haw, J. F., *Macromolecules* **1996,** *29* (1), 233-238.
307. Stewart, F. F.; Peterson, E. S.; Busse, S. C.; Orme, C. J., *Chemistry of Materials* **1997,** *9* (1), 155-163.
308. Hazendonk, P.; deDenus, C.; Iuga, A.; Cahoon, P.; Nilsson, B.; Iuga, D., *Journal of Inorganic and Organometallic Polymers and Materials* **2006,** *16* (4), 343-357.
309. Koch, B.; Vogel, M., *Macromolecules* **2009,** *42* (2), 531-536.
310. Beckmann, P. A.; Dybowski, C., *Journal of Magnetic Resonance* **2000,** *146* (2), 379-380.
311. Hua, Y.; Sarkar, T. K., *IEEE Trans. Signal Process.* **1991,** *39* (4), 892-900.
312. Grunwald, P. D., *The Minimum Description Length Principle*. MIT Press: 2007.
313. van Beek, J. D., *Journal of Magnetic Resonance* **2007,** *187*, 19-26.